Design and Fabrication of Polymer-based Lab-on-a-Chip Devices Towards Applications in Food and Environmental Analysis

Senkbeil, Silja

Publication date:
2012

Document Version
Publisher's PDF, also known as Version of record

Design and Fabrication of Polymer-based Lab-on-a-Chip Devices Towards Applications in Food and Environmental Analysis

Silja Senkbeil

Department of Micro- and Nanotechnology
Technical University of Denmark
Building 345 B
DK–2800 Kongens Lyngby
Denmark

Ph.D. Thesis
December 2012

Supervisor: Professor Jörg Peter Kutter, DTU Nanotech
Co-supervisor: Head of Division Jørn Smedsgaard, DTU Food

In der Mitte von Schwierigkeiten,
liegen die Möglichkeiten.

In the middle of difficulty
lies opportunity.

ALBERT EINSTEIN

To my parents Beatrix and Horst

Preface

This thesis is presented as a partial requirement for obtaining a Ph.D. degree from the Technical University of Denmark (DTU). The research was carried out at the Department of Micro- and Nanotechnology (DTU Nanotech), DTU, from October 2009 to December 2012 in the ChemLabChip group. The project was financially supported by DTU Nanotech, DTU Food, and the Copenhagen Graduate School for Nanoscience and Nanotechnology (C:O:N:T). The supervisors were:

Professor Jörg Peter Kutter, DTU Nanotech
Main supervisor

Head of Division Jørn Smedsgaard, DTU Food
Co-supervisor

Kgs. Lyngby, 31st December 2012

Silja Senkbeil

Abstract

Pesticides play a key factor in the high productivity achieved in modern agricultural food production. While increasing productivity and lowering production costs, they are potentially toxic and can have a serious impact on humans and the environment. In general, monitoring of pesticides and other environmental contaminants is performed in analytical laboratories, utilizing a multiplicity of time-consuming and cost-intensive chemical analysis methods like chromatography and mass spectrometry. To ensure food security and to monitor maximum residue levels in a highly globalized market, miniaturized analysis systems could provide inexpensive, portable devices for fast and reliable on-site monitoring of – not only – pesticides. Introduced already more than 20 years ago, lab-on-a-chip (LOC) devices found their way into biological and clinical research. Their fast analysis times, low sample volume and low reagent consumption are attractive for many applications in the life sciences, e.g., for DNA sequencing platforms and screening applications in drug development. It was only recently that the use of LOC systems gained considerable interest in the broad field of environmental analysis. In this work, several polymeric LOC systems for the analysis of dithiocarbamate (DTC) pesticides were designed and their performance was tested. Cyclic olefin polymer (COP) was studied as a potential material for non-aqueous analysis of DTC pesticides. While COP has some outstanding material properties compared to commonly used substrate materials, such as poly(methyl)methacrylate (PMMA) or polycarbonate (PC), it was shown that bonding of COP chips is challenging. Gold microband electrodes were integrated into microfluidic channels for electrochemical detection of the DTCs ziram and nabam. It was found that sulfur-containing DTC pesticides adsorb onto the gold surface of the electrode and thereby passivate it to a high extent. While sulfur-gold interactions of DTC pesticides were a major drawback for electrochemical detections, their high affinity for gold could

be exploited in a second microfluidic sensor. Here, the sensor consisted of a polydimethylsiloxane (PDMS) chip for on-chip mixing of DTCs with gold nanoparticle (AuNP), which were functionalized with rhodamine 6G (R6G). While AuNPs act as a fluorescence quencher for the adsorbed R6G, they interact with the sulfur-containing pesticides upon mixing and thus release R6G into the solution. The R6G fluorescence intensity was measured and could be related to ziram concentrations with a limit of detection as low as $16\,\mu g \cdot L^{-1}$. Due to its indirect sensing mechanism, the AuNP-based DTC sensor was not specific for ziram and a similar fluorescence response was measured for ferbam, demonstrating that the mechanism can be employed as an indirect detection scheme for several DTC pesticides. Therefore, the nonspecific detection mechanism needs to be combined with a separation step prior to AuNP-mediated detection, to allow quantitative and qualitative analysis of different DTC pesticides. To this end, a capillary electrophoresis (CE) unit was implemented on a third chip, which was fabricated of thiol:ene, a photopolymerizable material. The CE microchip consisted of a separation channel for DTC separation, and side channels for subsequent AuNP probe lamination of the separation bands. Even though a separation of pesticides was not performed, the electrokinetically driven lamination of AuNP, and the feasibility of indirect fluorescence detection of ziram in microfluidic channels with a small detection volume was proven. Furthermore, three different fluorophores could be separated on these chips, demonstrating that chips fabricated from thiol:ene offer a great potential within polymer based CE.

Resumé (in Danish)

Brugen af pesticider er en vigtig faktor i den høje produktivitet moderne landbrug har opnået i fødevareproduktionen. Skønt pesticider øger produktiviteten og sænker produktionsomkostningerne, så er de potentielt giftige og kan have en alvorlig indvirkning på mennesker og miljø. Generelt bliver overvågningen af pesticider og andre miljøforurenende stoffer udført i analyselaboratorier, ved anvendelse af talrige tidskrævende og omkostningstunge kemiske analysemetoder som kromatografi og massespektrometri. For at sikre fødevaresikkerheden og overvåge grænseværdier i et stærkt globaliseret marked, kan miniaturiserede analyse systemer give billige, bærbare enheder til hurtig og pålidelig on-site overvågning af – ikke kun – pesticider. Siden, deres introduktion for mere end 20 år siden, har lab-on-a-chip (LOC) systemer fundet vej ind i biologisk og klinisk forskning. Deres korte analysetider, lave prøvevolumener og lave reagensforbrug er attraktive for mange applikationer inden for naturvidenskab, f.eks. til DNA-sekventeringsplatforme og screeningsapplikationer i lægemiddelindustrien. Det var først for nylig, at brugen af LOC systemer opnåede en betydelig interesse indenfor miljøanalyser. I dette arbejde blev flere polymere LOC systemer, til analyse af dithiocarbamater (DTC) pesticider, designet og deres præstationer blev testet. Cyklisk olefin polymer (COP) blev undersøgt som potentielt materiale til ikke-vandig analyse af DTC pesticider. Mens COP har nogle enestående materialeegenskaber i forhold til almindeligt anvendte substratmaterialer, såsom poly(methyl)methacrylate (PMMA) eller polykarbonat (PC), blev det påvist, at bonding af COP chips er udfordrende. Guld mikrobåndelektroder blev integreret i mikrofluide kanaler til elektrokemisk detektion af DTC pesticiderne ziram og nabam. Det blev konstateret, at svovlholdige DTC pesticider adsorberes på guldoverfladen af elektroden og derved i stort omfang passiverer den. Mens svovl-guld interaktioner af DTC pesticider var en stor ulempe for elektrokemiske detektion, kunne den høje affinitet

for guld udnyttes i en anden mikrofluid sensor. Her bestod sensoren af en polydimethylsiloxane (PDMS) chip til on-chip blanding af DTC pesticider med guld nanopartikler (AuNP), som er funktionaliseret med rhodamine 6G (R6G). Mens AuNP partiklerne virker som en fluorescens dæmper for det adsorberede R6G, så interagerer de, efter blanding, med de svovlholdige pesticider og frigiver således R6G i opløsningen. Fluorescensintensitet af R6G blev målt og kunne relateres til ziram koncentrationer med en detektionsgrænse så lav som $16\,\mu g{\cdot}L^{-1}$. På grund af sin indirekte målemekanisme, var den AuNP-baserede DTC sensor ikke specifik for ziram og en tilsvarende fluorescens respons blev målt for ferbam, hvilket viser, at mekanismen kan anvendes som en indirekte detektionmetode til påvisning af flere DTC pesticider. For at tillade kvantitativ og kvalitativ analyse af forskellige DTC pesticider, skal den ikke-specifikke detektions mekanisme derfor kombineres med et separationstrin før den AuNP basede detektion sker. Til dette formål blev en kapillarelektroforese (CE) enhed implementeret på en tredje chip, som blev fremstillet af thiol:ene, et fotopolymeriserbart materiale. CE mikrochippen bestod af en separation kanal til DTC separation, og side kanaler for den efterfølgende laminering af separationsbåndene med AuNP. Selv om en adskillelse af pesticider ikke blev udført, blev elektrokinetisk drevet laminering af AuNP, og muligheden for indirekte fluorescensdetektion af ziram i mikrofluide kanaler med et lille detektionsvolumen bevist. Desuden kunne tre forskellige fluoroforer adskilles på disse chips, hvilket viser, at chips fremstillet af thiol-ene har et stort potentiale inden for polymer baseret CE.

Acknowledgments

First and foremost, this thesis would not have been possible without the help and support of many people and here I would like to take the opportunity to express my sincere gratitude to each of them.

I would like to thank my supervisor Professor Jörg P. Kutter for giving me the opportunity to undertake this Ph.D. project in his research group. His patience and encouraging support in times of difficulties, and his enthusiasm towards new ideas have been a constant motivation throughout my work. I also want to thank my co-supervisor Jørn Smedsgaard for many fruitful discussions regarding conventional pesticide analysis.

A special acknowledgment goes to my colleges in the ChemLabChip group at DTU Nanotech for providing such an inspiring and harmonic work environment that made me feel comfortable right from the beginning. Our endless discussions during lunch breaks often reached far beyond research topics and added a great lot of fun. I am especially grateful to Josiane P. Lafleur for her unconditional support throughout the last stages of my Ph.D. work and for her invaluable advice for all questions in life, but in particular, for being a true and caring friend. Thomas G. Jensen was a great help with his quick and often unconventional ideas for experimental setups, his programming and Danish translation skills. Klaus B. Mogensen was always there with his friendly guidance and expert advice in microchip capillary electrophoresis and electronics. I would like to thank my office companions Arnaud E. Musa and Andreas H. Kunding for their steadfast interest in my research work and good cheer. Coming from a mechanical engineering background, I was lucky to have Olga Ordeig and Detlef Snakenborg who were a great resource of help and advice with every question about chemistry and electrochemistry.

A special thanks goes to the technical stuff at DTU Nanotech and Danchip, Birgit Nygaard, Per Jonassen, Conny Hougaard and Helle V. Jensen for their guidance through technical issues during chip

fabrication. Last, but not least, I would like to thank my family and friends who took part in every moment, and Volker for being by my side with his enormous patience and support during the last months of my Ph.D. studies. You are my rock in breaking waves.

Contents

1. Introduction

When Manz et al. first described the concept of a miniaturized total chemical analysis system, they proposed a downscaling of well-established chemical analysis systems, such as chromatography and electrophoresis onto a single (portable) platform [1]. Following the general trend of miniaturization, the now-called micro total analysis system (μTAS) were developed on the basis of already available microfabrication techniques from the semiconductor industries. Research in the early years expanded from design and fabrication of these μTAS devices to applications in separation and detection of chemical compounds [2]. Over the time, the concept of μTAS was developed into lab-on-a-chip (LOC) devices to incorporate not only miniaturized chemical analysis, but also other laboratory processes – towards a fully automated miniaturized laboratory system [3]. LOCs gained much popularity in clinical diagnostics, nucleic acid, protein and cell studies, e.g., for high-throughput screening in pharmaceutical research and development, where often only small amounts of samples are available [4–7]. Moreover, miniaturization of laboratory processes on LOC systems benefits from short analysis times, less chemical reagent consumption and less heat generation. While glass and silicon were used as (relatively costly) substrate materials in early devices, new potential polymeric materials were soon investigated and polydimethylsiloxane (PDMS) became the major material choice for many researchers in the field. The shift from expensive cleanroom processes to more easily accessible fabrication methods did not only expand the user group for LOC research, but also paved the way for the development of cheap disposable analytical devices. These may one day be used as inexpensive, but smart devices in many areas, such as point of care devices for medical applications in private households or developing countries that do not have adequate laboratory resources. Beside the enormous potential of LOC systems as fully integrated and disposable sensors, there are some drawbacks

that need to be overcome. While the miniaturization of fluidic parts is often straightforward and especially electrophoretic on-chip separation methods are among the most successful implementations, the miniaturization and integration of peripheral devices, e.g., for detection and data processing, are more complex. A second trend in LOC platforms is therefore the development of disposable microfluidic cartridges that can be inserted into a small and portable device for analysis, as it is already used in some LOC solutions for, e.g., blood and DNA analysis [8]. Although LOCs are already now well represented in life science and related research areas, it was only recently that their potential was discovered for environmental monitoring. With an ever-growing world population and progressing industrialization, we are facing ongoing challenges in environmental monitoring of air, soil and water as well as foodstuff analysis. Frequent screening of many different samples is therefore indispensable to preserve otherwise endangered ecosystems, ensure water quality and secure foodstuff that is free of pesticide residues, toxins and other harmful additives.

Traditionally, environmental samples are taken at the place of interest and get transported to a laboratory for further analysis. Common state-of-the-art techniques, such as gas and liquid chromatography coupled to mass spectrometry, require large and expensive instrumentation and are usually reserved for few specialized analytical laboratories. Logistic challenges can therefore be a limiting factor for efficient and systematic inspections, especially in rural areas. However, if some screening functionalities could be implemented in portable LOC systems, analysis could be carried out on-site and allow easier access to, e.g., data about pesticide usage and residues in food production, or pollution of surface waters. Along with rapid screening for contaminants, this could offer the advantage of lower analysis costs and avoid analyte decomposition or contamination during sample transportation. Even though LOCs cannot offer the same sensitivity as conventional analysis instruments, they can definitely be useful tools for on-site prescreening, so that only critical samples need to be sent to laboratories. On-chip environmental analysis is in an early state and the focus is mainly on the development of measurement methods with a dominant trend towards electrokinetic separation techniques and optical or electrochemical detection pathways [9, 10]. In gen-

eral, the implementation of optical detection methods into LOCs is challenging, due to small sample volumes and limited optical path lengths in miniaturized system. Not many environmental analytes exhibit native fluorescence, so that derivatisation and preconcentration is often necessary. Some examples of optical detection systems have been reported, such as laser induced fluorescence detection of polycyclic aromatic hydrocarbons (PAHs) and UV absorbance detection of phenolic water pollutants and explosives [9, 10]. However, electrochemical detection pathways are generally preferred in miniaturized platforms for environmental analysis, due to their high sensitivity and compatibility [11]. Successful electrochemical detection of phenolic compounds, nitroaromatic explosives and trace metals in microfluidic devices with sensitivities in the low $\mu g \cdot L^{-1}$ range have been described [9, 11, 12].

In contrast, the on-chip analysis of pesticides is underrepresented in the field, with only a few applications. One prominent approach is the incorporation of enzymatic biosensors for organophosporous and carbamate pesticide detection into microfluidic systems. The sensor makes use of the pesticides' ability to inhibit (acetyl)cholinesterase and very low detection limits in the $ng \cdot L^{-1}$ range can be reached [13, 14]. A major drawback with these sensors is their non- selective qualitative response that can give rise to synergistic effects, i.e., a higher response for a mix of pesticides than for the sum of the individual pesticides, or false positive results due to matrix compounds that inhibit the enzyme activity with no pesticide present [14, 15]. These effects can be circumvented by the use of adequate microfluidic separation techniques. A major challenge is hereby the single-use concept of enzymatic sensors: enzymatic activity gets (irreversibly) lost in a reaction with the respective pesticide and fresh assay reagents are needed for every new detection step.

However, detection methods of this type have been successfully implemented into microfluidic channels by, e.g., using enzyme-coated magnetic beads that can be trapped and consequently released inside the microchannel. Like this, fresh enzyme is provided for every measurement [16]. Although, biosensors are quite successful for organophosporous and carbamate pesticide detection, bioanalytical assays for dithiocarbamate pesticide detection are rare due to the

complex mode of action and versatile enzymatic reactivity of these pesticides [14, 17]. The work presented in this thesis addresses alternative, enzyme-free, electrochemical and optical detection routes and focuses on the fabrication of polymeric LOCs for detection and separation of dithiocarbamate pesticides, a pesticide group that is so far neglected in LOC-based environmental analysis.

1.1. Thesis outline

The thesis is divided into seven chapters that guide the reader through the development process of different microfluidic chips for potential dithiocarbamate analysis.

Chapter 2

This chapter gives a brief introduction to different theoretical aspects that are important to understand the background behind fluid dynamics in miniaturized systems, electrochemical and fluorescent measurements. While a small section introduces the reader to some polymer-related fabrication methods, more in-depth details to chip fabrication are also given in the chapters pertaining to specific chip designs, since fabrication was a considerable part of this thesis.

Chapter 3

Polymeric materials have a broad range of different properties and a suitable material needs to be chosen with regard to the intended application. Cyclic olefin polymer (COP) is an interesting material, which fits many needs. Structuring and especially bonding qualities of two different COPs were investigated and are summarized in this chapter.

Chapter 4

A microfluidic chip with integrated gold electrodes for electrochemical measurements is presented and the performance is characterized. The chips were further tested as electrochemical detection of dithiocarbamate pesticides, nabam and ziram, was tested.

Chapter 5

Gold nanoparticles offer new strategies for sensing pathways in many research fields. In this chapter, a microfluidic chip for on-chip mixing of dithiocarbamate pesticide standards with rhodamine-functionalized gold nanoparticles is presented. Dithiocarbamate pesticides were detected with high sensitivity in a novel microfluidic sensor, utilizing the fluorescence quenching properties of gold nanoparticles (AuNPs).

Chapter 6

Thiol-ene chips were fabricated for microchip capillary electrophoresis. Thiol-ene is a new material for microfluidic chips and their performance as capillary electrophoresis microchips is demonstrated, for the first time, by a separation of three different fluorophores. The AuNP-mediated fluorescence principle is transferred from the pressure driven device with a large detection cell (in Chapter 5) to an electrokinetically driven chip with a smaller detection volume.

Chapter 7

A concluding chapter that summarizes the achieved results and discusses future perspectives.

2. Theoretical Background

2.1. Dithiocarbamate pesticides

Pesticides are chemically and/or biological active compounds that can be classified into fungicides, insecticides, herbicides and plant growth regulators. They are used to repel or control pests on crops and hereby enhance the productivity in food production. A specific group of fungicides are the dithiocarbamate (DTC) pesticides that are widely used in agricultural production. DTCs are a group of organosulfur compounds that can be further divided into three subgroups, dimethylithiocarbamates (DMDCs), ethylenbisdithiocarbamates (EBDCs) and propylenbisdithiocarbamate [18]. Table 2.1 summarizes the nine different DTCs. All DTCs have in common that they are complexes between carbamate groups and a transition metal (except for thiram), and are highly insoluble in aqueous solution. The chemical structure of the pesticides ziram, ferbam and nabam,which were investigated in this thesis, are depicted in Figure 2.1, and their solubility and different solvents is summarized in Table 2.2. Beside their positive effect on food production, they can be potentially toxic to non-target organisms and the environment as their residues are highly mobile in soil, which might bear risk for ground water contamination [19] [17]. More recently they were related to the development of Parkinson's disease in agricultural workers [20]. Fungicides of the dithiocarbamate group are some of the most detected pesticides in the European Union and it was only recently that new Maximum Residue Levels (MRLs) were published by the European Commission (EC) [21, 22]. The MRLs vary for different dithiocarbamate species but right now there are no specific methods that can differentiate each single dithiocarbamate. Generally, dithiocarbamate are decomposed by acid hydrolysis with hot mineral acids before analysis. The decomposition causes the generation of carbon disulfide (CS_2), which can then be detected by spectrophotometric and (gas)chromatographic

methods. The unspecific detection of evolved CS_2 is prone to false positive results due to interference from matrix volatiles or acid digestion, beside being very time consuming [17, 21].

Table 2.1.: Dithocarbamate classification

Dimethyl-dithiocarbamates	Ethylenbis-dithiocarbamates	Propylenbis-dithiocarbamates
Ferbam	Maneb	Propineb
Thiram	Mancozeb	
Ziram	Nabam	
	Zineb	
	Metiram	

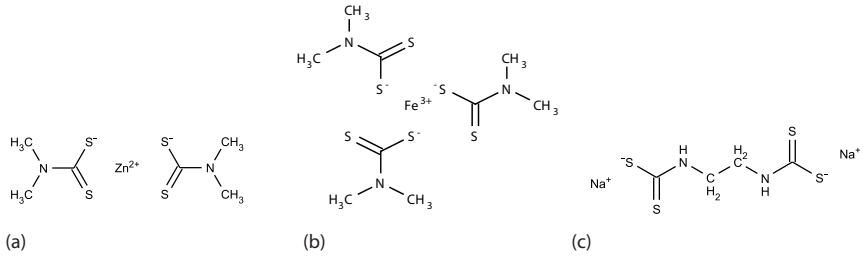

Figure 2.1.: Chemical structure of dithiocarbamate pesticides, (a) ziram, (b) ferbam and (c) nabam

2.1.1. Pesticide residues and legislation

Pesticide residue levels and their toxicology are evaluated in the Joint Meeting on Pesticide Residues (JMPR), which is administered by the FAO[1] and the WHO[2]. They give recommendations and risk assessments to their member countries on, e.g., MRLs and Acceptable Daily Intakes (ADIs). For foodstuff that is produced inside or imported into the European Union, the EC evaluates and approves every active substance for plant protection in food and feed production, and

[1] Food and Agriculture Organization of the United Nations
[2] World Health Organisation

Table 2.2.: Solubility [23]

Ziram	Ferbam	Nabam
Water: 18.3 $mg \cdot L^{-1}$	Water: 130 $mg \cdot L^{-1}$	Water: 200 $g \cdot L^{-1}$
Acetone: 2.88 $g \cdot L^{-1}$	Acetone (soluble)	insoluble in organic
Methanol: 0.22 $g \cdot L^{-1}$	Acetonitrile (soluble)	solvents
Toluene: 2.33 $g \cdot L^{-1}$	Chloroform (soluble)	

assesses their impact on human health and the environment based on the JMPR recommendations. Foodstuff and feed produced for the European market is currently subjected to the EC regulation from 2005 [22]. The regulation defines pesticide MRLs for a broad range of different fresh and processed food products. In general, a residue is the trace that a pesticide leaves in or on food after the application. Consequently, MRLs are the maximum traces that are legally allowed in or on food and feed and are expressed in $mg \cdot kg^{-1}$. The MRLs for the different DTCs on foodstuff cover a range from $\mu g \cdot kg^{-1}$ to $mg \cdot kg^{-1}$ and vary for diverse food. They can be found in the European pesticide database. The maximum residue level varies from, e.g., 0.1 $mg \cdot kg^{-1}$ for citrus fruits to 5 $mg \cdot kg^{-1}$ for cherries [24].

2.2. Microfluidics

The growth of the semiconductor industry and with it the fast-paced development of microfabrication techniques led to a new world of microscale structuring methods. With the development of the first on-chip gas chromatograph [25] and the highly promoted research on ink-jet printers by IBM [26], fluidic devices on the microscale caught the interest of more and more researchers, leading to the development of countless applications in chemistry, biology and medicine. The following section explains the principle physics of microfluidics, responsible for the outstanding performance of these devices.

2.2.1. Laminar flow

Fluids in a microfluidic system behave quite differently than in the macro systems that we encounter in our everyday life. When we compare the surface area-to-volume ratio (SA:V) of a cylinder with the diameter $d = 4\,\text{cm}$, a length $l = 8\,\text{cm}$ and a volume $V = 100.5\,\text{mL}$, the SA:V is $1.25\,\text{cm}^{-1}$. The SA:V increases to $1000.25\,\text{cm}^{-1}$, if we reduce the volume to $V = 100.5\,\text{nL}$ and shrink the cylinder to a capillary ($d = 40\,\mu\text{m}$). Reducing the SA:V can have positive effects, as capillary forces dominate and heat dissipates easily by convective transfer, but can also impact surface adsorption of molecules.

Fluid flow in the macroscale regime is dominated by inertial effects that introduce instabilities and turbulence to our macro system, making it chaotic and unpredictable. On the other hand, in microfluidic systems, such as the above mentioned capillary, viscous forces dominate and instead a laminar flow regime is developed, resulting in sliding layers of fluids rather than chaotic turbulence [27]. The ratio of inertial to viscous forces is expressed by the dimensionless Reynolds number:

$$Re \equiv \frac{\rho d \upsilon}{\eta} \tag{2.1}$$

where ρ is the density, d is the length scale, e.g. the capillary diameter, υ is the linear flow velocity and η is the viscosity. Reynold numbers $Re \leq 2000$ indicate a laminar flow regime, in the transitional regime $2000 \leq Re \leq 2300$ turbulent flow is not fully developed and finally for $Re \geq 2300$ the turbulent flow regime occurs [3]. In microfluidic devices small dimensional parameters as low as a few µm are common and hence a low Reynolds number indicates flow in the laminar regime. The absence of turbulence may have many positive effects, but as we shall see, it makes mixing of fluids more challenging.

In Figure 2.2 two differently sized solutes are dissolved in a liquid stream that is flowing next to an adjacent stream of the same solvent. The smaller molecules (dark blue) might have a diffusion coefficient of $D \approx 5 \times 10^{-10}\,\text{m}^2\cdot\text{s}^{-1}$ like, e.g., sugar molecules in water, the bigger cyan colored solutes might be of the size of DNA molecules with a diffusion coefficient of $D \approx 1 \times 10^{-12}\,\text{m}^2\cdot\text{s}^{-1}$. As we can see, the smaller molecules diffuse completely through the entire width of the

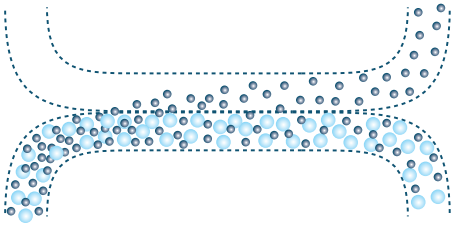

Figure 2.2.: Schematic mechanism of diffusion in two adjacent laminar fluid streams in a microchannel.

channel, whereas the bigger molecules do not mix with the upper stream within the time the two streams are in contact.

In a microchannel, mixing of two solutes flowing in two laminating streams of the exact same solvent is only dependent on diffusion. The kinetics behind this phenomenon were described by Einstein and von Smoluchowski in their studies on Brownian motion [28, 29]. The movement of a single molecule in one dimension, according to Einstein and von Smoluchowski described by:

$$\bar{x}^2 = 2Dt \tag{2.2}$$

or

$$t = \frac{\bar{x}^2}{2D} \tag{2.3}$$

where x is the distance traveled in time t and D is the solute's specific diffusion coefficient. From this equation it is obvious that mixing in micro dimensional devices is highly dependent on the length scale x. For the large molecule in Figure 2.2 the time to diffuse half the width of the channel (e.g. 50 µm) would approximate to 42 min and for the smaller molecule to 5 s. Mixing of both molecules will only occur, if the time that the two adjacent fluid streams are in contact for diffusion is long enough.

In addition, the molecules are also transported in axial direction by the fluid stream with constant velocity v from the inlet to the outlet. A dimensional analysis will give the following choices for the

time scale: the time to move the distance w by radial diffusion is:

$$\tau^{rad}_{diffusion} = \frac{w^2}{D} \tag{2.4}$$

and the time to move the same distance w in axial direction by convection is:

$$\tau^{a}_{convection} = \frac{w}{\upsilon} \tag{2.5}$$

If $\tau^{rad}_{diffusion} << \tau^{a}_{convection}$ diffusion is much faster than convection and diffusive mixing is dominant. The relation between convective and diffusive transport is described by another dimensionless number, the Péclet number [27]:

$$Pe = \frac{\tau^{rad}_{diffusion}}{\tau^{a}_{diffusion}} \equiv \frac{\upsilon w}{D} \tag{2.6}$$

From this number the approximate length l_m required for complete diffusive mixing in a channel with the width w can be estimated as:

$$l_m \approx wPe \tag{2.7}$$

Reynolds and Péclet numbers are not the only dimensionless numbers describing important fluidic phenomena, but they are some of the most important guides for first dimensional design considerations in microfluidic chip design. For a comprehensive overview on the physics behind microfluidics, the interested reader is referred to the reviews by Gravesen and Squires [30, 31] and for an in-depth discussion to Bruus [27].

2.3. Flow in microchannels

Moving liquids in microchannel structures can be achieved in many ways. Capillary forces can be used to drag aqueous liquids along hydrophilic surfaces, liquids can be pumped through a channel by high precision syringe pumps or electro-charging effects can be utilized to transport electrolyte solutions within an electric field. During this work two different fluid pumping mechanism were used, which are explained in further detail in the sections below.

2.3.1. Pressure driven flow

Fluid that is moved through a straight microchannel, e.g., by a syringe pump, is driven by a pressure drop between the inlet and the outlet of the channel. The Hagen-Poiseuille flow or pressure driven flow is characterized by infinitesimally small liquid layers that slide against their adjacent layers, building a parabolic flow profile inside the channel, illustrated in Figure 2.3. The liquid's velocity at the channel wall can be assumed as equal to the velocity of the wall (i.e., zero), also known as *no-slip* boundary condition.

For the straight microchannel with a circular cross section the volume flow Q is:

$$Q = \frac{\pi r^4}{8\eta l}\Delta p \tag{2.8}$$

with channel radius r, channel length l, the liquid's viscosity η and the pressure drop along the channel Δp. The reciprocal of the equations first term is also known as the fluidic resistance of the channel. Once again, this emphasizes the influence of the dimensional parameter on the microfluidic behavior, as a decreased channel radius will rise the fluidic resistance with the power of 4 [3].

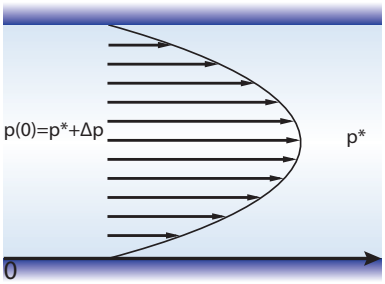

Figure 2.3.: Hagen-Poiseuille flow profile in a capillary where Δp is the pressure difference.

Another fluid-driving force particularly useful in microscale separations is electroosmosis which is discussed in the next section.

2.3.2. Electrical double layer

When a surface is immersed into a solution, a interfacial region is formed whose properties differ significantly from the bulk properties. The formation of an electrical double layer (EDL) was first described by Helmholtz who suggested that a monolayer of negativley (or positively) charged ions is adsorbed at the surface and an adjacent layer of positively charged counterions from the solution is immobilized by electrostatic forces [32]. This capacitor-like, fixed surface layer is therefore known as Helmholtz layer. In Section 2.4.1, we will see that the Helmholtz layer can further be divided into two planes.

After Helmholtz denoted this simple model of an EDL, Gouy and Chapman described another model of the EDL. In their model, an interfacial potential between immobilized negative charge carriers and positively charged counterions in a diffuse double layer is built up. Today's model of the EDL was further modified by Stern, who combined the two models to a system with a fixed (Helmholtz) layer and a diffuse Gouy-Chapman layer, illustrated in Figure 2.4. Due to the charge distribution across the layers, a potential is built up that decays linearly over the Helmholtz layer (also called Stern layer) and exponentially over the Gouy-Chapman layer [33]. The potential between the two layers at the shear plane is the ζ-potential. Even though a potential is built up, the entire system maintains electroneutrality at any time with the positive charge carriers canceling the negatively charged surface.

2.3.3. Electroosmotic flow

If we take a closer look at the surface of a glass capillary in contact with a buffer solution at high pH, the terminal silanol (-Si-OH) groups at the surface are deprotonized to -Si-O-, leaving a negatively charged wall. With the positively charged counterions next to it, a rigid Helmholtz layer is built up and charge carriers from the bulk solution forming the more diffuse Gouy-Chapman layer.

The thickness of this diffuse double layer can be calculated with the Debye length λ_D

$$\lambda_D = \sqrt{\frac{\varepsilon RT}{2F^2 I}} \tag{2.9}$$

where ε is the dielectric constant, R is the universal gas constant, T the absolute temperature, F is Faraday's constant. The ionic strength of the buffer solution:

$$I = \frac{1}{2}\sum_i c_1 {z_i}^2 \tag{2.10}$$

depends on the charge number z and the concentration c of each buffer component [3]. The Debye length for common buffer systems is in the order of a few nm and thus much smaller than commonly used micochannels with dimensions ranging from 1 µm to a few 100 µm.

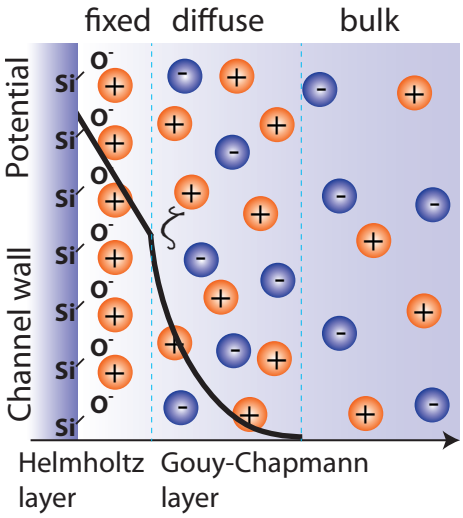

Figure 2.4.: Schematic of the electrical double layer defined by Stern. The EDL can be divided into a fixed and a diffuse double layer, keeping electroneutrality by balancing out charges between the layers. The decay of the potential from surface to bulk solution (0 potential) and the ζ-potential at the shear plane are drawn across the layers.

If an electric field E is applied between inlet and outlet of a microfluidic channel that is filled with buffer solution, hydrated protons within the diffuse layer move towards the cathode and pull adjacent fluid layers with them. A constant electroosmotic flow (EOF) with a flat flow profile across the bulk solution is established with the electroosmotic velocity:

$$\nu_{eo} = \mu_{eo} E \tag{2.11}$$

with

$$\mu_{eo} = \frac{\varepsilon \zeta}{\eta} \tag{2.12}$$

From Equation (2.11) we can conclude that the EOF is strongly dependent on the ζ-potential, which in return is influenced by both the surface chemistry of the wall and any chemical changes in the liquid due to changes in pH, temperature, ionic strength etc.

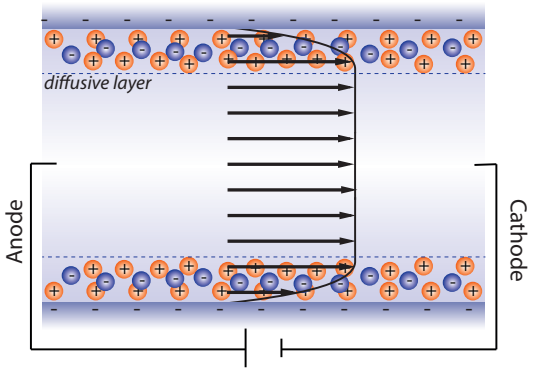

Figure 2.5.: Electroosmotic flow in a glass capillary with the typical flat flow profile outside the diffuse layer, while the flow velocity drops to 0 across the EDL.

2.3.4. Microchip capillary electrophoresis

When an electric field is applied across a microfluidic channel we have already seen in Section 2.3.3 that a net flow towards the cathode is

established. Furthermore, ionic species, which might be present in the buffer solution, will migrate towards the anode or cathode of the system. The electrophoretic mobility of such a charged species is given by:

$$\mu_{ep} = \frac{q}{6\pi\eta r_h} \tag{2.13}$$

with charge q and the hydrodynamic radius r_h. The total velocity for a charged species is therefore a combination of electrophoretic and electroosmotic velocity and with Equation (2.11) and Equation (2.13) can be written as:

$$\nu_{tot} = (\mu_{eo} + \mu_{ep})E \tag{2.14}$$

Figure 2.6 illustrates that highly (positively) charged cations will travel fast through a capillary, followed by neutral molecules and the much slower, (negatively) charged anions. This separation technique has been transferred from capillaries (capillary electrophoresis) to microchips with very short analysis times in the millisecond range [2]. The implementation of capillary electrophoresis on microfludic platforms allows for valveless electrokinetic sample injection of very small sample volumes in the pico- and nanoliter range. The cross-channel design from Figure 2.7 illustrates gated sample injection into a separation channel.

In a microchannel with negatively charged walls the electroosmotic flow will have the same direction than the current flow in the system and Ohm's law and Kirchhoff's circuit law can be used as an analogy to calculate electroosmotic flow in the system [34]. The cross-channel system consists of four connected channels with liquid reservoirs that are connected to a high voltage supply. During a gated injection, the separation channel is first conditioned with a buffer stream that is flowing from the buffer reservoir (B) through the separation channel towards the waste reservoir (W). During this pre-injection step, no sample is allowed into the separation channel and it is therefore driven from the sample reservoir (S) towards the sample waste reservoir (SW). A small fraction of the buffer stream is still led into the SW to prevent the sample from "bleeding" into the separation channel. At the next step the voltage settings are changed and the sample

is allowed to flow into the separation channel while the flow from the sidearms is stopped. After a short time period the voltages are switched back to their previous settings and the sample plug that was built in the intersection is now "pushed" into the separation channel. Other configurations for sample injection are, e.g., the pinched injection scheme and the double T injector and are discussed in further detail in Jacobson et al. [35] and Shultz-Lockyear et al. [36].

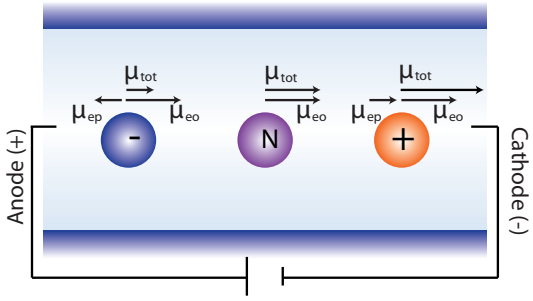

Figure 2.6.: Separation principle in microchip capillary electrophoresis. Differently charged analytes and neutral compounds can be separated due to their different migration mobilities.

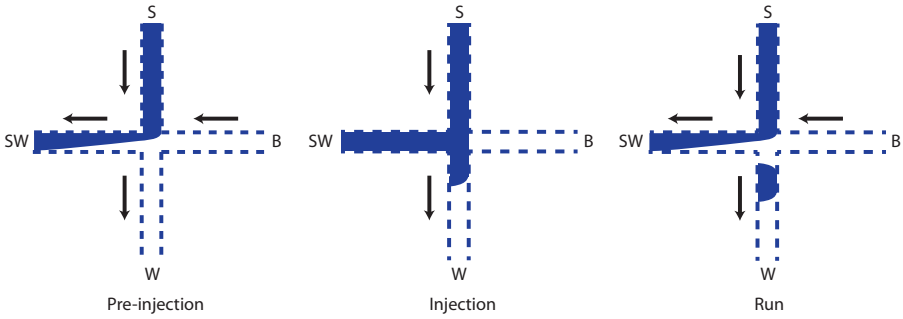

Figure 2.7.: Gated injection scheme for microchip capillary electrophoresis. Figure adapted from [3]

2.3.5. Optical detection in microfluidics

Optical detection schemes are often used in microfluidic systems and have a long history in conventional analytical chemistry. Besides absorption and photo luminescence, fluorescence spectroscopy is one of the major detection methods.

Fluorescence

In fluorescence spectroscopy an electron is excited to a higher electronic state by the absorption of a photon. The excited species can only remain in its high electronic state for a very short time frame, usually in the order of 10^{-15}s and eventually relaxes to its ground state. During this relaxation, fluorescence occurs due to the emission of a photon. The wavelength of the emitted light is larger than the wavelength of the absorbed light, as a consequence of, e.g., thermal energy losses during relaxation [37]. The excitation of and emission by a species is a repetitive cycle that in theory can be repeated over and over but the fluorescence signal can be lost permanently by photochemical destruction of the molecule known as photobleaching. A non-permanent loss of fluorescence may occur by temporary interactions with its environment (quenching) or with itself (self-quenching). Although fluorescence detection offers very high sensitivities, the implementation of a detection setup onto a microfluidic platform can be challenging, as emitted light needs to be separated from excitation light. Therefore, a typical setup often consists of several filters and lenses, to focus the excitation light (e.g., a laser beam) onto the mirochannel and a detector (e.g., a photo multiplier tube) that is often placed in an angle (e.g., 45°) to the excitation source to avoid the direct collection of excitation light. Another drawback in fluorescence analysis is that not all analytes exhibit native fluorescence and thus need to be labeled prior to analysis.

2.4. Electrochemistry

An alternative to optical detection is the integration of electrodes into the microfluidic system and the electrochemical characterization and

analysis. The following section will give a short introduction to the theory behind electrochemical measurements in microfluidic systems.

2.4.1. The electrode-electrolyte interphase

In Section 2.3.2 we have already described the electrical double layer (EDL) and the charge distribution at the interface giving rise to electrokinetic phenomena such as electroosmotic flow. Figure 2.8 illustrates the interaction of a (positively) charged metal electrode with the ionic zones of the aqueous electrolyte. The EDL that is formed at the interface is described with the Bockris-Devanathan-Muller model, a further development of the Stern model. This model uses the fixed and diffuses layers, but also the predominance of polar solvent molecules and adsorption of species at the electrode surface [38].

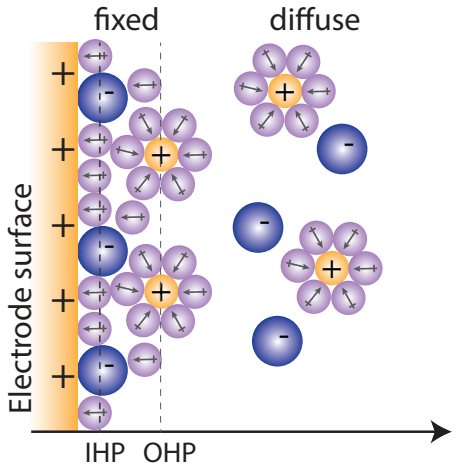

Figure 2.8.: EDL with inner Helmholtz plane (IHP) and outer Helmholtz plane (OHP) at the electrode-electrolyte interface, with contact adsorption of large anions and solvated smaller cations, which are not able to interact with the electrode surface. The arrow in the solvent molecules is pointing towards the negative dipole moment of the solvent.

Polar water molecules will orientate themselves at the electrode, penetrated only by large anions that are not solvated and hence

able to intact directly with the electrode surface. The plane through the locus of these contact adsorbed species is called inner Helmholtz plane (IHP). Solvated smaller cations are not able to interact with the surface and are non-specifically adsorbed, restricted by the first layer of water molecules. The plane through their locus is called the outer Helmholtz plane (OHP). Both Helmholtz planes are located within the Helmholtz layer and the potential from the electrode surface across this layer drops linearly (see Section 2.3.2) [39]. Note that the whole system is at equilibrium and electrically neutral. The EDL can be seen as a parallel-plate capacitor with two capacities in series:

$$\frac{1}{C} = \frac{1}{C_f} + \frac{1}{C_d} \tag{2.15}$$

where C_f is the capacitance of the fixed layer and C_d the capacitance of the diffuse layer. Varying electrolyte concentration, desorption and adsorption processes can cause charge accumulation at the electrode-electrolyte interface, responsible for double layer charging and an increased capacitance. Even though no charge is transferred, an external, nonfaradaic current can be measured. In contrast, a faradaic current flows as the result of a charge transfer due to oxidation or reduction reactions at the interface [33]. In electrochemical experiments these oxidation and reduction (redox) reactions at the interface are of interest and, hence the faradaic current.

The equilibrium potential for a redox system in solution is given by the Nernst equation:

$$E = E^{\circ} + \frac{RT}{nF} ln \frac{C_O}{C_R} \tag{2.16}$$

with E° being the standard potential, R the universal gas constant, T the absolute temperature, C_O and C_R the concentrations of the oxidized and reduced form, respectively. If we consider an inert (metal) electrode surface in contact with a redox system

$$Red \rightleftharpoons Ox + ne^{-} \tag{2.17}$$

the reduced component Red will be oxidized if a current passes through the electrode and the potential at the electrode is set above E. The potential difference between the electrode potential and the

equilibrium potential is the overpotential η. Table 2.4.1 shows the convention for the redox reaction directions used throughout this thesis.

Table 2.3.: Convention for redox reactions

direction	overvoltage	current	reaction
anodic	$\eta > 0$	$i > 0$	$Red \rightarrow Ox + ne^-$
cathodic	$\eta < 0$	$i < 0$	$Ox + ne^- \rightarrow Red$

2.4.2. Three-electrode setup

Electrochemical measurements usually use a potentiostat with a three-electrode setup that consists of a working electrode (WE), i.e., the electrode-electrolyte interface, a reference electrode (RE) and a counter electrode (CE) in a cell filled with liquid. The RE is maintained at a stable potential and used as a reference for the potential control and measurement at the WE. To prevent any current flow between WE and RE, the potentiostat has a high input impedance so that the current in the system is drawn through the CE. A current flowing through the RE would change its potential. WE and RE are usually brought in close contact to minimize the Ohmic drop across the electrolyte [33].

2.4.3. Cyclic voltammetry

Conventional macro electrode

Cyclic voltammetry (CV) is a powerful technique to determine the dynamics of redox systems, characterize electrode behavior and study chemical and adsorption processes. The potential is swept in a triangular wave form and the resulting current at the WE is monitored. The scan starts at a potential that is below the characteristic E of the analyte and the current measured corresponds to non-faradaic charging processes. During the forward scan, when the potential approaches E, the oxidation of the analyte begins. While the reduced form is consumed at the electrode surface, more species are brought

to the surface by diffusive transport mechanisms and the anodic current further increases until a maximum is reached. The concentration gradient in the diffusive layer at the electrode surface increases further into the bulk solution and a depletion of the surface area takes place as can be seen from the drop in current leading to a peak-shaped voltammogram. When the potential scan is reversed, oxidized species that were generated during the forward scan are reduced and a negative cathodic current is measured until the electrode surface is again depleted of oxidized species.

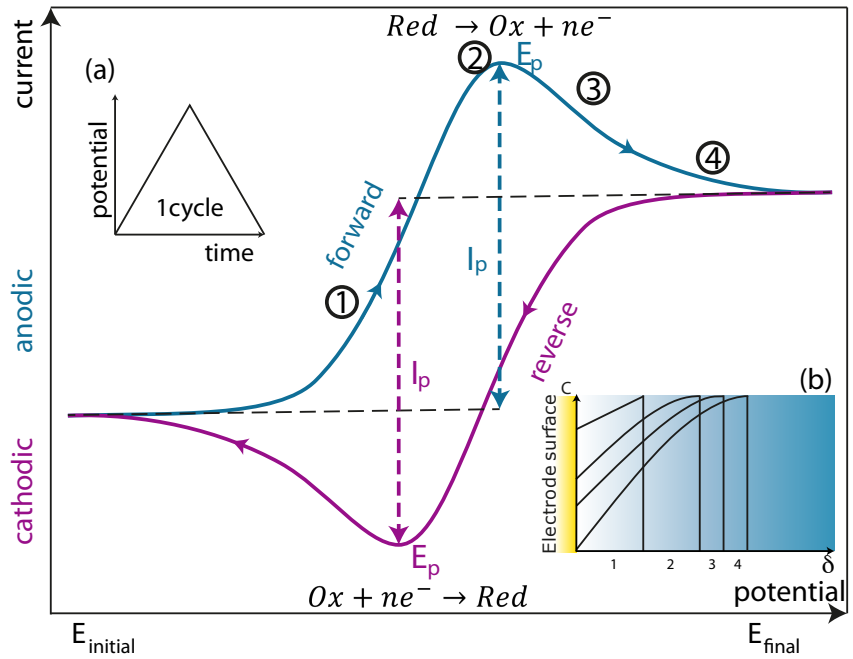

Figure 2.9.: Schematic illustration of a cyclic voltammogram with anodic and cathodic peaks for a typical reversible redox system. E_p and I_p are the peak potential and limiting current for the anodic and cathodic sweep. Inset (a) depicts the triangular potential waveform for one cycle. The concentration gradients and their corresponding diffusion layer thickness δ is illustrated in inset (b) for different steps during the forward scan.

The simulated voltammogram in Figure 2.9 shows some characteristics for a chemically reversible system (Nernstian kinetics), i.e., the rate of the electron transfer is higher than the mass transport. In such a system the difference in peak potentials ΔE_p for a n-electron process equals $^{0.059}/_{\mathrm{n}}$ V and the peak current ratio $\frac{I_p^a}{I_p^c}$ is unity. The peak current is given by the Randles-Sevčik equation at 25 °C,

$$I_p = 2.69 \times 10^5 n^{3/2} C_\infty D^{1/2} \nu^{1/2} A \tag{2.18}$$

where n is the number of electrons, C_∞ is the bulk concentration (in mol·cm^{-3}), D is the diffusion coefficient (in cm^2·s^{-1}), ν is the scan rate (in V·s^{-1}) and A is the electrode area in (cm^2). As will be discussed in the next section the shape of a cyclic voltammogram will have a sigmoidal form for microelectrods and measurements under hydrodynamic conditions.

Miniaturization and hydrodynamic behavior

The ongoing trend towards miniaturization has also brought some advantages to the electrochemical world. Microelectrodes (i.e., one electrode dimension $< 25\,\mu$m [39]) display outstanding characteristics. The reduction in size reduces the double layer capacitance, increases the current density and their overall lower measurement currents make investigations of low conducting systems possible (lower Ohmic drop compared to macro system)[40]. Furthermore, due to radial (and planar) diffusion at the electrode the diffusion layer thickness exceeds the dimensions of the electrode and steady state limiting currents are rapidly obtained during cyclic voltammetric experiments. If we consider a microelectrode in a microchannel, fresh solution is brought to the electrode surface by a constant laminar flow. Hence, the thickness of the diffusion layer is dependent on the convective transport of the fluid and decreases as the flow rate increases. This can be seen in an increase in limiting current, which is illustrated in Figure 2.10.

Microfluidic systems satisfy usually, the following assumptions:

1. diffusive transport takes place in the direction perpendicular to the electrode surface,

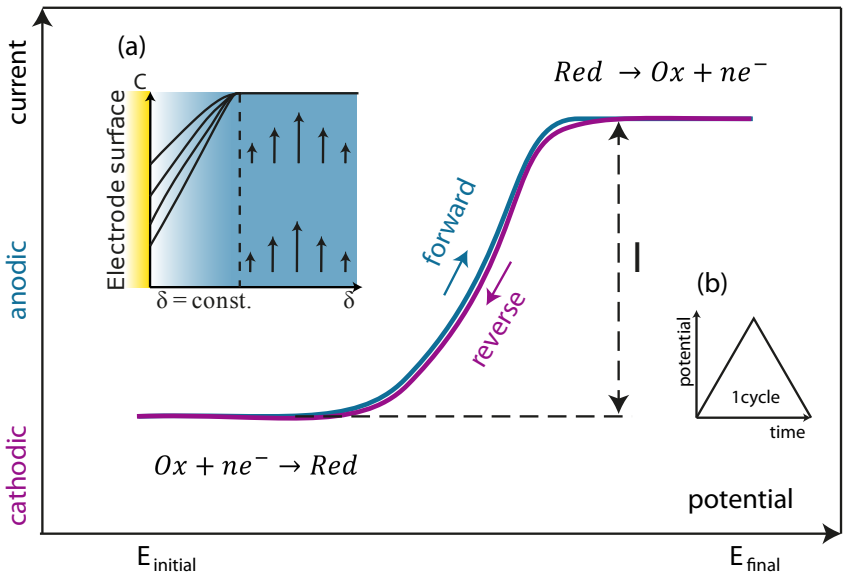

Figure 2.10.: Simulated cyclic voltammogram for a reversible redox reaction with a sigmoidal shape for a microelectrode setup under hydrodyamic laminar flow conditions. The concentration gradients and their corresponding diffusion layer thickness δ is illustrated in inset (a). Inset (b) depicts the triangular potential waveform for one cycle.

2. diffusive transport is small compared to convective,
3. the parabolic flow profile can be approximated as linear in the close vicinity of the electrode.

under theses circumstances, the limiting current of a band electrode in a microchannel is described by the Levich equation [41]:

$$I_{lim} = 0.925 n F C_\infty D^{2/3} \left(\frac{Q}{h^2 d} \right)^{1/3} w x_l^{1/3} \tag{2.19}$$

with the number of electrons n, Faraday's constant F, the bulk concentration C_∞ (in mol·cm^{-3}), the diffusion coefficient D (in cm^2·s^{-1}), the volume flow Q (in cm^3·s^{-1}), the half-channel height h, the channel width d, and the band-electrode width w and length x_l.

2.4.4. Gold electrodes in aqueous solutions

In this work, inert gold (Au) electrodes were used for electrochemical measurements. The applicable potential range for inert electrodes in (non-)aqueos systems that can be used for electrochemical measurements is defined by the electrolytic breakdown of the solvent. Figure 2.11 shows a hypothetical linear sweep[3] voltammogram for an Au electrode in aqueous solution with water and oxygen as the only active species. As can be seen, the current increases almost exponentially for the decomposition of water and the resulting oxygen and hydrogen evolution, respectively. The potential range in between is called the potential window and varies for different electrode materials and solvent/electrolyte compositions. Measurements outside this window would suffer from high background currents. The use of non-aqueous solutions can widen the potential window. If the solution is saturated with oxygen, which is usually the case for nondegassed aqueous solutions, the dissolved oxygen is reduced at lower potentials, thus limiting the useful potential range. Usually, degassing the solution and purging it with nitrogen can remove the dissolved oxygen [39].

[3] That is, a linear scan over a certain potential range or the forward scan in cyclic voltammetry.

2.4.5. Electrochemical detection

Although cyclic voltammetry is a very useful technique to electrochemically characterize a specific analyte, it cannot be used as a detection method after analyte separation in, e.g., capillary electrophoresis. Here, DC amperometry can be used as a detection method, where a predefined potential is applied between the working and reference electrode. When the analyte passes the working electrode it is either reduced or oxidized and the recorded current is a measure for the concentration of the analyte. The specific detection potential can be identified from cyclic voltammograms and the purple line in Figure 2.11 shows the response for a hypothetical analyte during the forward scan. A detection potential close to the onset of the oxidation (1) obviously would not give a high signal; a detection at the half-wave potential (2) would give a better resolution, but would be very prone to minimal potential changes. The optimal detection potential would therefore be the minimal potential where the process is already current limited (3), but not to close to the beginning oxygen evolution (4), to minimize the signal-to-noise ratio [42].

2.5. Microfabrication techniques

All those miniaturized methods require microfabrication techniques to produce microfluidic devices with small channel dimensions. The rapid development in microelectronics and MEMS[4] applications provides a wide range of photolithographic and other microfabrication techniques that can be used for microfluidic devices. Most of these techniques are based on silicon and glass substrates and the first microfluidic devices were made of these materials. On the other hand, silicon and glass substrates are rather expensive materials that can only be processed in cleanroom facilities, which increase the production costs of disposable devices. With the demand for cheap, single-use and often biocompatible devices the development was shifted to polymeric materials. Although cleanroom processes are still used for certain applications, several alternatives for polymer fabrication are presented in the sections below.

[4] MicroElectroMechanical System

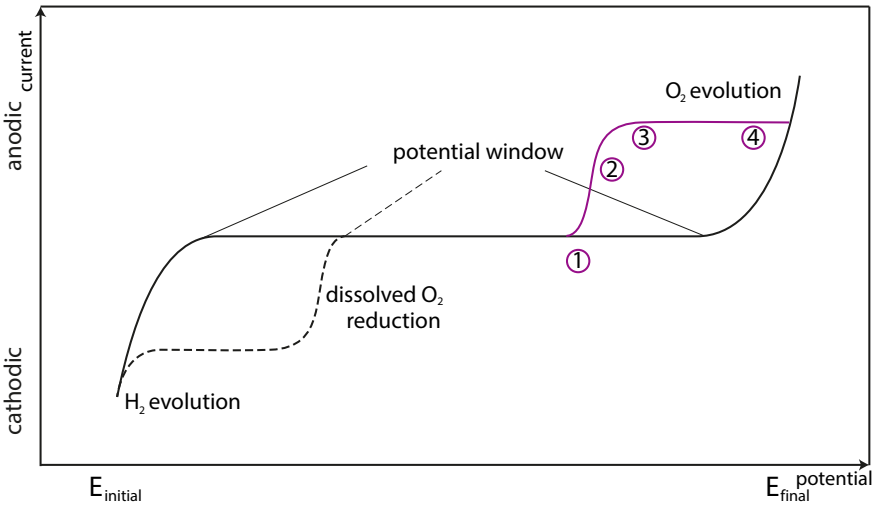

Figure 2.11.: Simulated behavior for a forward scan from a negative potential to a positive potential in aqueous solution where only water and oxygen (dashed line) are present. The straight black line shows the potential window for a degassed solution, where the onset of hydrogen and oxygen evolution limits the applicable potential window. The dashed line shows the reduced potential window, due to dissolved oxygen reduction, when the solution is saturated with oxygen. The purple line shows the corresponding response for a present analyte under hydrodynamic conditions. Finding the right detection potential: (1) A potentail close to the onset of oxidation will give a low signal. (2) A detection close to the half-wave potential will be prone to potential changes. (3) Optimal detection potential where the process is current limited. (4) A higher potential will not result in a better detection signal but the onset of oxygen evolution might interfere with the measurement. Figure adapted from LaCourse [42].

2.5.1. Laser ablation

Laser ablation is a very fast technique to structure a wide spectrum of polymeric materials that covers polystyrene, polycarbonate (PC), polyethyleneterephthalate, poly(methyl)methacrylate (PMMA), polydimethylsiloxane (PDMS) and many more [43]. Two different radiation wavelengths, infrared (IR) and ultraviolet (UV) radiation, are used to remove polymeric material. The substrate is placed on a holder and the laser beam is moved in x-y direction across it, following a path that is predefined through a computer aided design (CAD) drawing. Depending on the radiation, the material is either removed by thermal degradation of locally heated areas (IR) or by a combination of UV-activated chemical bond breaking and thermal degradation. Feature sizes are highly dependent on radiation wavelength, laser power, number of passes and optical properties of the system. Typical minimum feature sizes for an IR system are a few 100 µm, but smaller dimensions can be reached with UV systems or masking techniques that use a photomask to define the ablated structure rather than a direct laser writing along a path. Even though small feature sizes are easily realizable within seconds, the surface roughness, channel shape and bulge formation is highly dependent on the polymer composition, but also on various processing parameters and interactions of them [44].

2.5.2. Soft lithography

In softlithography a negative mold is made by micrstructuring techniques such as micromilling or more advanced cleanroom techniques. The mold is then used to build a positive polymer copy. The molding process allows for cheap replication of many copies with small three-dimensional structures down to the nm range [45].

Casting

Casting is a fast and reproducible structuring method for elastomeric polymers and microfluidic chips are often cast in PDMS. The silicone base is mixed with a curing agent prior to use and poured over the mold. The chemical crosslinking of the two components starts imme-

diately after mixing, but can be enhanced by placing the filled mold into an oven. For a curing temperature of 80 °C, the solidification takes approximately 2 h. The cured PDMS can than be peeled off from the mold. Figure 2.12 depicts the molding process.

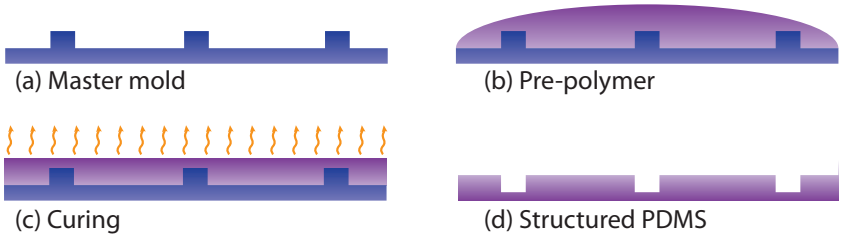

Figure 2.12.: Casting of PDMS structures. (a) Negative master mold fabricated by micromilling or cleanroam fabrication methods. (b) Pre-polymer is poured over the mold and (c) cured. (d) Final positive structure.

3. COP/COC – a new emerging material?

3.1. First generation microfluidic chip for DTC detection

The Ph.D. project started with the intention to develop a microfluidic device that can perform a chemical analysis of several dithiocarbamate (DTC) pesticides. The design of a first generation microfluidic chip involved on-chip electrochemical detection combined with a second optional optical detection method in non-aqueous media. Figure 3.1 shows the schematic drawing of a microfluidic device with integrated gold electrodes for electrochemical detection and fiber couplers for UV absorbance or fluorescence measurements. The fabrication process of the microfluidic part is discussed in detail in the following sections, whereas the integration of microelectrodes and the electrochemical measurements are discussed in Chapter 4 on page 59.

3.2. Substrate materials

When developing a new microfluidic system several aspects are important. Apart from the channel geometry, the choice of an adequate substrate material is fundamental. The microchips that were developed during this thesis were designed for in-field monitoring of DTC pesticides. Chips for this purpose have to be cheap and disposable and electrically insulating for the implementation of electrochemical detection schemes and electrokinetically driven separations. In addition, low autofluorescence and high light transmission are crucial for optical detection and resistance to organic solvents is explicitly needed for DTC analysis in non-aqueous solutions.

Silicon and glass chips would offer a high chemical stability, but fail in terms of optical transparency, insulating properties (silicon)

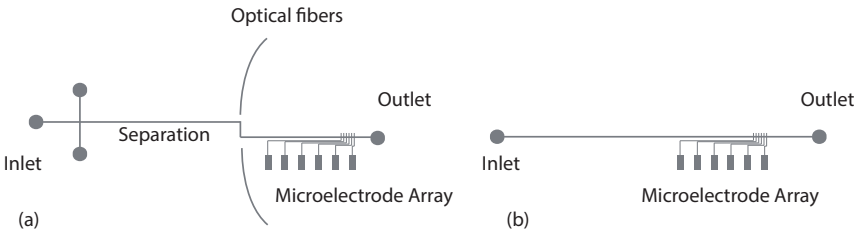

Figure 3.1.: (a) Schematic drawing of a COP microchip for electrochemical and additional optical detection. The design consists of an injection cross for electrokinetic sample injection, a separation channel, a detection cell for UV absorbance measurements and an electrode array for electrochemical detection. (b) A first generation chip for electrochemical detection with a 68 mm × 50 µm × 50 µm channel and an integrated microelectrode array for pressure driven flow.

and low production costs. Although quartz glass is optically transparent down to the UV range and silicon surfaces can be modified, so that they are transparent and electrically insulating, the fabrication of such devices would involve several photolithographic steps, which would be reflected in an overall rise of production time and costs. Polymer substrates, on the other hand, are cheap substrate materials that can be structured in fast thermo-forming processes.

During the last 30 years of microfluidic research, several polymeric materials have been investigated. Among those, the most prominent ones are poly(methyl)methacrylate (PMMA), polycarbonate (PC) and polydimethylsiloxane (PDMS). All of them are well studied with standard procedures for structuring and bonding. Especially PDMS is very popular and often the first choice, when it comes to rapid prototyping. Apart from their good processability in fast reproduction methods like injection molding, hot embossing and casting, they offer good optical transparency reasonable for many applications. The chemical resistance of PMMA and PC is rather poor, crack propagation at stress points will cause failure of the microfluidic chip when they come in contact with common polar solvents like ethanol or methanol. This major drawback makes them unsuitable for operations in non-aqueous solutions. PDMS, in contrast, will not de-

compose upon contact with organic solvents, but adsorption into the polymer matrix can cause swelling of the polymer [46]. Its high compliance is very advantageous for on-chip valves, where a high grade of deformation is needed but channel deformation might also influence the flow stability [47]. Note that PDMS is optically transparent from the UV range to near infrared range and offers some advantages in other areas like high gas permeability that are crucial in biomedical applications.

In the late 1980s a new polymer, cyclic olefin polymer (COP), became commercially available and soon raised interest as a new thermoplastic "supermaterial" with promising properties. COP's main advantage over commonly used polymers is its excellent chemical resistance against organic solvents, paired with good optical transparency even in the near UV range, which makes it superior to PMMA, PC and PDMS.

COP is produced by a wide variety of manufacturers and is therefore available under various brand names, with Topas[1], Zeonor[2] and Zeonex[2] being the most prominent ones in microfluidic applications. During this work, Topas and Zeonor foils were used. Both polymers are available in different grades with slightly different characteristics due to their different polymerisation mechanisms. Topas is polymerized in a chain polymerization with ethene, Zeonor and Zeonex, on the other hand, are produced in a ring-opening metathesis polymerization of cyclic monomers and a subsequent hydrogenation [48, 49]. For this reason, Topas, which is synthesized from more than one monomer, is referred to as a cyclic olefin copolymer (COC) and Zeonor/Zeonex as COPs. In this thesis, COP will be used as a synonym for both polymers, as suggested by Nunes et al. [50].

Not much information is available on the exact chemical composition and its influence on the physical and chemical properties of both, Topas and Zeonor. The different synthesis schemes are illustrated in Figure 3.2 A. The increase in glass transition temperature (T_g) and stiffness for Topas is related to an increase in norbornene content and its position in the main chain [51], whereas the T_g for Zeonor and Zeonex grades is related to a change in substitute group and subse-

[1]Topas Advanced Polymers Inc., Florence, KY, USA
[2]Zeon Corporation, Tokyo, Japan,

quent ring formation [48, 49] (Figure 3.2 B). The different properties of these COPs are summarized in Table 3.1 and their chemical resistance is compared with other common polymers in Table 3.2.

Table 3.1.: Properties of common microchip polymers

	Topas	Zeonor	PMMA	PC
Glass transition temperature T_g [°C]	78-178	102-164	106	150
Optical transmission [%][3]	91	92	88	92
Water absorption [%]	0<0.01	<0.01	0.1	0.04

Table 3.2.: Chemical resistance of different thermoplastic polymers

Topas	Zeonor	PMMA	PC
Methanol	Methanol	diluted mineral acid	limited resistance: alcohols, diluted mineral acids
Ethanol	Ethanol		
Isopropanol	Isopropanol		
Acetone	Acetone		
Acetonitrile	Acetonitrile		
Sulfuric acid (40%)	Sulfuric acid (10%)		
Hydrochloric acid	Hydrochloric acid (36%)		
Nitric Acid	Nitric Acid (65%)		
Sodium hydroxide (50%)	Sodium hydroxide (50%)		

3.3. Microstructuring

A major advantage of thermoplastics over conventional silicon and glass substrates is their suitability for automatized high throughput fabrication methods, which will reduce the cost of a single device. Injection molding is probably the fasted mass fabrication method but it is arguably not the preferred one for single prototyping. Hot embossing is an alternative thermal replication methods that can be automated, especially for lab-on-a-foil applications [52], and was used as the preferred structuring method of COP film during this

[3] Percentage of optical transmission given by the supplier according to ISO 13468-1,-2: Optical transmission in the visible region of the spectrum, 390 to 750 nm.

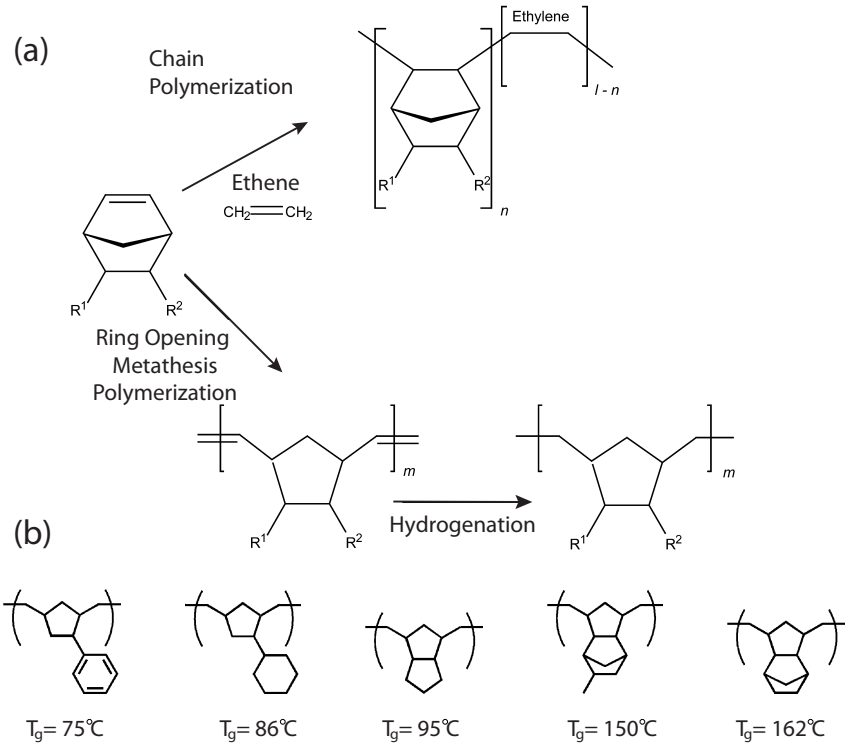

Figure 3.2.: (a) Synthesis of Topas and Zeonor/Zeonex through chain polymerization and ring opening methathesis [48], (b) T_g is dependent of the chemical structure of Zeonor/Zeonex [49]

work. Furthermore, foil substrates are more flexible than stiff plates substrates which facilitates demoulding after structuring.

3.3.1. Hot embossing

The functional principle of hot embossing and nanoimprint lithography is very similar, both methods are used to shape a thermoplastic by pressing a stamp into a heated substrate. Substrate and stamp are brought into conformal contact and placed in a press. Once the setup is heated to a temperature above the glass transition temperature of the thermoplastic, the stamp is pressed into the softened material. While keeping the pressure constant, the temperature is lowered below the glass transition temperature, the structured polymer solidifies and can be separated from the stamp. The replication quality depends highly on the rheological properties of the softened polymer and hence polymer specific process parameters for temperature and pressure are applied. When using a press that is equipped with a vacuum chamber, even small feature sizes in the nanometer range are possible [53]. Hot embossing and nanoimprint lithography differ from each other, in that the former is defined for structures that are embossed into a thick substrate and thus only the surface is structured. In nanoimprint lithography, a thin film only slightly thicker than the fabricated structures is used and hence a thin residual layer remains after the structuring that can be removed by etching.

Silicon stamp fabrication

The COP microchips that were used in parts of this thesis were fabricated by hot embossing using a manual hydraulic press. The silicon stamp that was used to replicate structures was fabricated on a 4 inch silicon (Si) wafer (525 µm thickness). The channel structures were transferred to the Si-wafer by standard positive UV-photolithography, followed by an anisotropic DRIE[4] step in an inductively coupled plasma etcher (Surface Technology System, Newport, UK). Deep anisotropic etch profiles were fabricated utilizing the Bosch process, which consists of two-step etching and passivation cycles. During

[4]Deep Reactive Ion Etching

the etching phase sulfur hexafluorid is used to etch silicon and it is followed by a passivation step, where octafluorocyclobutane is used to deposit a passivation layer onto the sidewalls that will protect already etched areas from further exposure to the reactive ions in the next cycle. The alternation of etch and passivation steps results in a scalloped surface that becomes smoother as the cycle time decreases. By alternating etching and passivation steps, deep anisotropic etch profiles with straight sidewalls were obtained. Figure 3.3 shows two SEM[5] micrographs of a Si-stamp for COP embossing. An etching/passivation ratio of 1.2 with a cycle length of 4.4 s was used, that resulted in slightly tapered sidewalls (3° undercut) and a very smooth surface (scallop size $\ll 1\,\mu m$). After etching, the photoresist was stripped by an oxygen plasma followed by an RCA[6] clean and a wet oxidation of a 200 nm thin silicon oxide layer. The oxide layer was almost etched away in a short hydrofluoric acid dip, leaving a smoother sidewall surface. To prevent sticking of the polymer to the stamp, a teflon like coating was applied with chemical vapor deposition (CVD). During CVD a monolayer of 1*H*,1*H*,2*H*,2*H*-perfluorodecyltrichlorosilane is covalently bound to the silanol groups of the Si-surface, which makes the surface of the stamp hydrophobic and prevents sticking of COP during the molding and demolding processes. Each wafer contained three Si-stamps that were diced with a Disco automatic dicing saw (DAD 321, Japan).

Figure 3.4 illustrates the entire fabrication process from master fabrication to final polymer channel structure.

Zeonor embossing

Zeonor foil was chosen as the preferred substrate material for microfluidic chips because of its superior foil quality. Where Topas foils (TOPAS Advanced Polymers Inc., Florence, KY, USA) have a lot of imperfections, e.g., small trapped air bubbles and striation marks from foil extrusion, Zeonor foil does not show any visible imperfec-

[5] Scanning Electron Microscopy

[6] Cleaning step invented by Radio Corporation of America, which involves cleaning of organic and inorganic contaminants and the removal of thin (native) oxide layers.

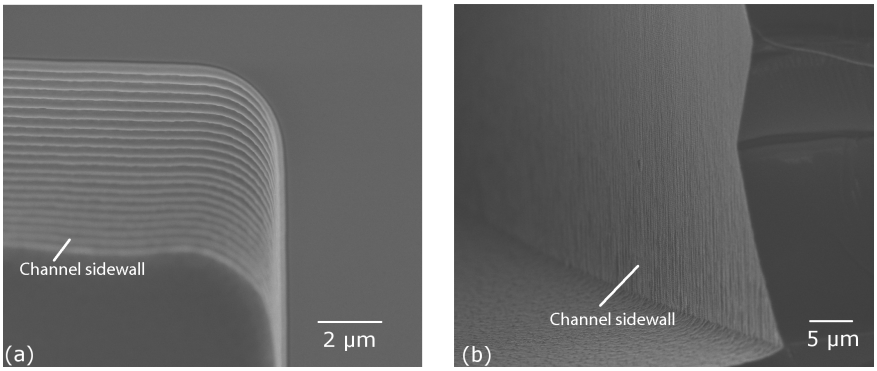

Figure 3.3.: (a) Si-stamp after DRIE, scallop size is much less than 1 µm. (b) Smooth sidewall of a Si-stamp after silicon oxide etch.

tions. It is available in two different grades, ZF-14 ($T_g = 136°C$) and ZF-16 ($T_g = 163°C$) and various foil thicknesses, varying from 40 µm to 188 µm. ZF-14-188 was used as the substrate material for all Zeonor chips during this work. It was partly obtained as a sample from Zeon (Zeon Europe GmbH, Düsseldorf, Germany) and later purchased from Ibidi (Ibidi GmbH, Planegg, Germany). The foil is covered with a protective film on one side and this protected side was always used as the active side for structuring and bonding. A manual hydraulic press (P/O WEBER Remshaldern, Germany) with two guiding columns and individually addressable hotplates was used to emboss a straight micro channel with the following dimensions 50 µm × 50 µm × 68 mm. The Si-stamp was cut from the wafer in a rectangular shape (10 mm × 75 mm) and a piece of Zeonor foil was cut, slightly bigger than the Si-stamp. To prevent sticking of COP foil to the metal platen of the press, the embossing stack was sandwiched between a bottom glass plate, a flat teflon coated Si-wafer, and a top glass plate, before it was loaded into the preheated press. The temperature was increased to the final embossing temperature and the press was left for temperature equilibration for 10 min before embossing. Embossing temperatures from 145 °C to 160 °C and forces from 7 kN to 15 kN were applied. A constant pressure over 10 min was manually maintained by adjusting the pressure with the hydraulic hand pump. After embossing, the press was left to cool

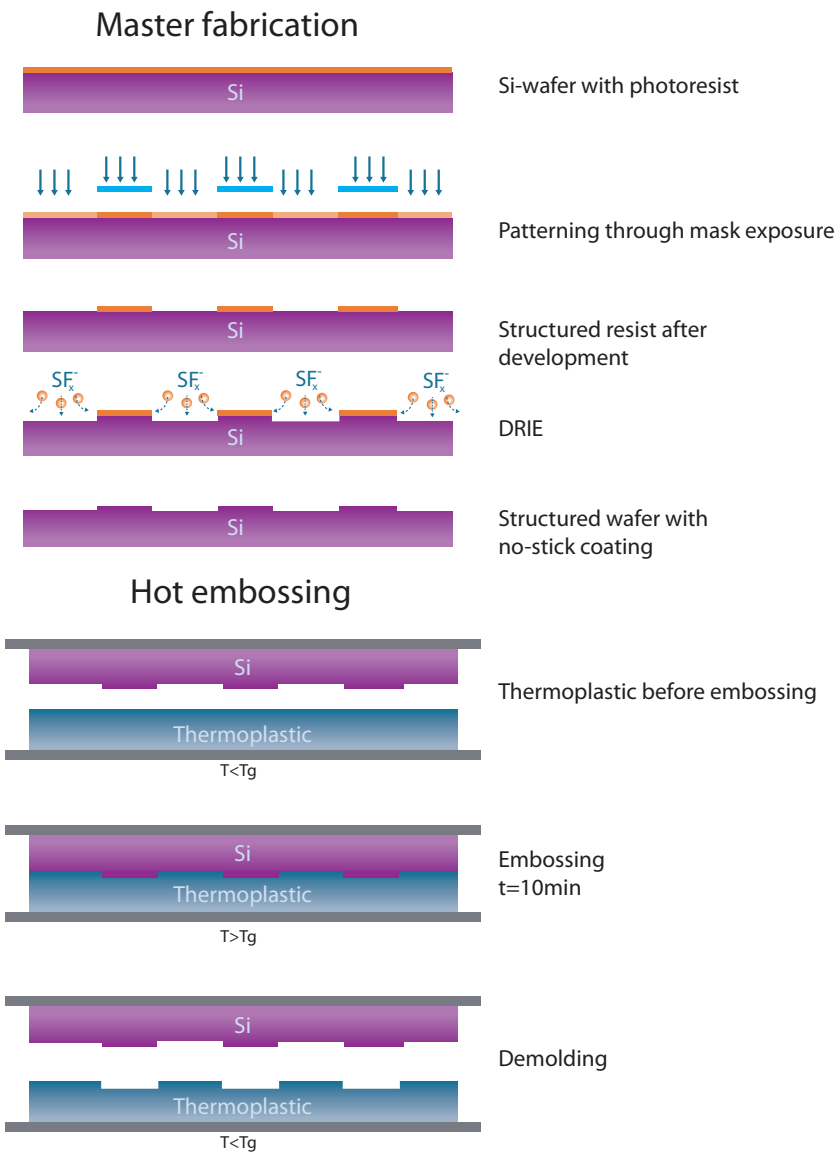

Figure 3.4.: Schematics of the Si-stamp fabrication and hot embossing process.

and the sandwich was taken out at 80 °C. The embossed foil can be demolded by carefully sliding a scalpel between the foil and the flat Si-wafer, thus carefully lifting foil and stamp off the wafer. After that, the foil can readily be peeled off the Si-stamp. Optimum embossing results were found for an embossing temperature of 155 °C and 10 kN embossing force. Figure 3.5 shows the crosssection of an embossed channel.

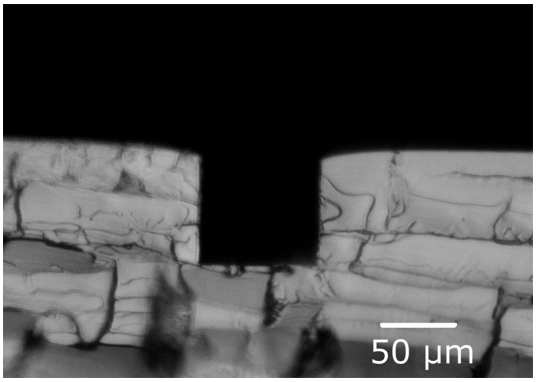

Figure 3.5.: Cross section of an embossed microchannel in COP. Dimensions: 80 µm × 80 µm

Hot embossing of Topas foil (Topas 5013L, $T_g = 134$ °C, foil thickness $t = 254$µm) can be performed with the same embossing parameters, as previously described for Zeonor embosssing. Topas foil is stiffer than Zeonor foil and hence manual demolding can cause crazing of the material in areas with high local tension. The white lines typical for crazing can be seen in Figure 3.6. Re-heating of the stamp/foil stack in an oven at 100 °C, after the separation from the flat Si-wafer and prior to demolding, can facilitate the demolding and prevents crazing.

Once the foil is structured, holes are drilled through the reservoir area for a later microfluidic interconnection. The yet open channel is laminated with a COP foil to seal the structures.

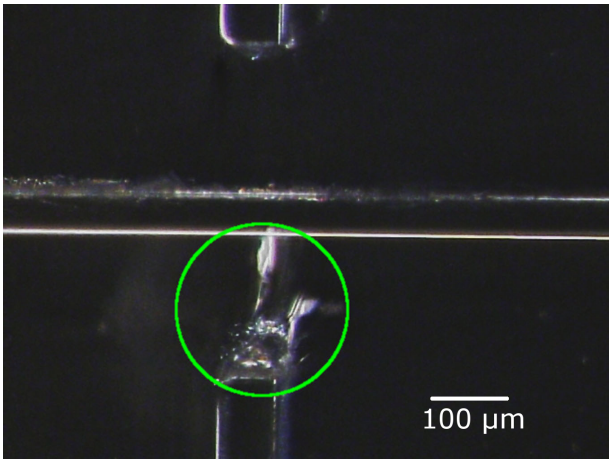

Figure 3.6.: Distorted structure in Topas foil after demolding due to stress-induced crazing of the brittle material. The micrograph shows a microchannel (horizontal structure) and two fibercouplers (top and bottom structures) at a distance ca. 200 µm away from the channel. White lines that are typical for crazing can be seen in the bottom structure (green circle) and along the channel wall.

3.4. Bonding

Bonding and the (ir)reversible sealing of open channel structures is a crucial step in the fabrication of microfluidic devices. Bonding of glass [54], PDMS, PDMS-to-glass [55] and PMMA [56, 57] is usually straight forward and existing protocols can easily be adapted. In contrast to this, COP bonding is more challenging as we will see in the following sections.

3.4.1. Thermal bonding

Sealing of an open polymeric structure can be obtained by thermally activated diffusion bonding. During this process, the structured part is sealed with the same material by bringing them into conformal contact and placing them in a press. While pressing them together at a temperature below T_g the two surfaces in contact are bonded by thermally activated crosslinking of the polymers. Several research articles have been published describing the thermal bonding of either Topas or Zeonor, mostly low T_g grades. Successful thermal bonding of thick slides ($> 1\,mm$) [58–62], thin layers of spincoated Topas [63–65], and fast lamination using an office roll laminator [66] have been reported. Thermal bonding of COP is often not sufficient and a variety of strategies were developed by several research groups to improve the bond strength of this particular polymer [67–73]. Some are suggesting direct bonding with rather complicated application of adhesives: here, a thin layer of UV glue is applied to the bond surface and the mating parts are carefully aligned before UV exposure. Obviously, channel clogging due to excess UV glue is frequently encountered and the authors try to overcome this by extrapolating the glue spread rate, using sacrificial channels and nitrogen to blow out excess glue [74].

3.4.2. Surface activation

Furthermore, different surface treatment methods have been suggested to improve COP bonding. In general, surface treatment aims to modify the surface characteristics, while the bulk material is unchanged thus providing a stronger bond between two mating surfaces.

The following sections give an overview over such treatments and explain qualitatively the results for Zeonor and Topas foil bonding. See also Table 3.3.

UV and UV/ozone treatment

Surface exposure to UV radiation is expected to photolytically degrade surface polymers and thus lower the T_g of the surface, while the bulk remains unchanged [57]. While Truckenmüller et al. [57] were the first to successfully bond PMMA applying UV radiation, Bhattacharyya et al. [67], Tsao et al. [68] and Shinohara et al. [69] investigated UV-irradiation, combined UV/ozone (UV/O_3) and oxygen plasma surface treatment and their impact on improving the bond strength of COP. They found that the exposure to reactive ozone and oxygen plasma produced low molecular weight polymers through chain scission, thus lowering the surface T_g. Furthermore, the surface became more hydrophilic due to the oxidative reaction and the formation of terminal oxygen containing groups. Both the lower surface T_g and hydrophilic surface were suspected to have a positive effect on bonding strength [69].

Oxygen plasma treatment

Native COP surfaces are generally very hydrophobic and their terminal hydrocarbon groups make covalent functionalization or bonding challenging [75]. Mizuno, Shinohara and co-workers [69, 76], and later Roy et al. described a positive effect of oxygen plasma treatment on COP bond strength [70]. By exposing Zeonex 480 plates ($T_g = 138\,°C$) to oxygen plasma Mizuno and Shinohara found an increase of surface energy from $0.6\,J{\cdot}cm^{-2}$ to $8\,J{\cdot}cm^{-2}$ and an increase in burst pressure to 1.31 MPa for samples that were treated with a 30 s oxygen plasma and bonded at room temperature (though no burst pressure was given for untreated samples). Roy et al. report an increase of burst pressure from 1.61 MPa (untreated) to 2.03 MPa for oxygenated argon plasma treatments of a sandwiched Topas 5013 and Topas 6015 chip ($T_g = 134\,°C$ and $T_g = 158\,°C$, respectively), with bonding temperature=138 °C [70]. As already described by Hwang et al., they confirmed a change in surface wettability by a change in

contact angle from 90° to below 20° and related the improved bonding strength to implementation of oxygen groups into the surface of the respective COPs [77]. The presented surface activation methods are summarized in Table 3.3.

Solvent-assisted bonding

Solvation of a polymer surface by a suitable solvent enables the entanglement of its polymer chains, which then become more mobile and promote the diffusion across the interface of two mating surfaces during bonding [78]. The ability of a solvent to dissolve a specific material is given by the compound's solubility parameter, e.g. the Hildebrand parameter δ. The specific Hildebrand parameter for Zeonor foil is not published by the manufacturer, but Tsao et al. reported a value of 17.7 $MPa^{1/2}$ for COC [78]. Polymers and solvents with the same or close Hildebrand parameter are likely to be soluble in each other. Wallow et al. bonded Zeonor 1060R slides successfully by immersing them in a 80:20 wt% ethanol:decalin mixture (10 min for the unstructured lid and 30 s for structured parts) before thermal bonding [71]. They could improve the bonding strength by more than 2-fold, compared to to untreated samples. Miserere et al. used a PDMS slab that was soaked in hexadecane for 1 h as an ink-pad to plastify the unstructured Topas 8007 lid before bonding [79]. A third, vapor based method was first described by Ro et al. where they used a short exposure to methylcyclohexane vapor to plastify Zeonor 1020R [80, 81]. Mair, Ogilvie and co-workers further investigated this vapor method and Mair et al. reported very high burst pressure values (36 MPa for a single chip) for Topas 8007 chips that were bonded by a cyclohexane vapor plastification and subsequent 15 min UV exposure after pressure-assisted room temperature bonding [72, 73]. The reported solvent bonding methods and achieved bond strengths are summarized in Table 3.4.

3.5. Experimental

Surface activation tests of Zeonor and Topas foils were performed using a UV-flood lamp (Dymax 5000-EC, Dymax Europe GmbH,

Table 3.3.: Comparison of reported surface activation methods and obtained bond strength for different Zeonor/Zeonex and Topas grades.

Treatment	Grade	T_g [°C]	Bonding temp. [°C]	Bonding pressure [MPa]	Strength	Test method	Ref.
VUV 1 min	Zeonex 480	138	22	2.5	1.77±0.25 MPa	tensile test, glued to metal bands	[69]
VUV/O_3 10 min	Zeonex 480	138	22	2.5	1.33±0.21 MPa		
O_2 plasma 30 s	Zeonex 480	138	22	2.5	1.31±0.63 MPa		
UV/O_3	Zeonor 1020R	105	90	4.8	0.806 mJ·cm^{-2}	razor blade test	[68]
native	Zeonor 1020R	105	90	4.8	<0.003 mJ·cm^{-2}		
UV/O_3 1–30 min	Zeonor 750R	70	70	3.45	≈ 8 MPa	three point bend test	[67]
O_2 plasma 1–10 min	Zeonor 750R	70	70	3.45	≈ 6 MPa		
native	Zeonor 750R	70		3.45	≈ 5.54 MPa		
O_2 plasma 30–120 s	Zeonex 480	138	70 (annealing)	none	≈ 8 J/m^{-2}	razor blade test	[76]
O_2 plasma	Topas 5013/6015	134/158	125	2	1.61 MPa	burst pressure	[70]
native	Topas 5013/6015	134/158	125	2	2.03 MPa		

Table 3.4.: Comparison of reported solvent assisted bonding methods and obtained bond strength (if available) for different Zeonor/Zeonex and Topas grades.

Treatment	Grade	T_g [°C]	Bonding temp. [°C]	Bonding pressure [MPa]	Strength [MPa]	Ref.
ethanol/decalin	Zeonor 1060R	100	60	≈ 1.38	≤ 16.13	[71]
native	Zeonor 1060R	100	88	≈ 1.38	≤ 6.89	
150 s Cyclohexane vapor + 15 min UV irradiation	Topas 8007	78	22	0.178	≈ 17	[72]
150 s Cyclohexane vapor	Topas 8007	78	22	0.178	≈ 12	
60 s Cyclohexane vapor + 15 min UV irradiation	Topas 8007	78	22	0.178	≈ 12	
60 s Cyclohexane vapor + 15 min UV irradiation	Topas 8007	78	22	0.178	≈ 6	
Cyclohexane vapor 36 s	Topas 6015	158	65	1.4	N.A.	[73]
Cyclohexane vapor 5.5 min	Topas 8007	78	65	1.4	N.A.	
Methylcyclohexane vapor 3 min	Zeonor 1020R	105	70	0.69	N.A.	[80]
Methylcyclohexane vapor 1 min	Zeonor 1020R	105	40	1.38	N.A.	[81]
Hexadecane 4 min	Topas 8007	78	80	roll laminator	N.A.	[79]

Wiesbaden, Germany, intensity: 40 mW·cm^{-2} at 365 nm), a UV/O_3-photoreactor (UVP PR-100, UVP LLC. Upland, CA, USA, nominal irradiation peak intensity 15 mW·cm^{-2} at $\lambda = 254$ nm) and an oxygen plasma chamber (atto plasma chamber with 13.56 MHz generator, Diener Electronic, Ebhausen, Germany). All chips were cleaned with isopropanol in an ultrasonic bath for 10 min prior to bonding to remove particles, flushed again with isopropanol and blown dry with nitrogen. For Zeonor substrates, the protected side of the foil was used as the active bonding side.

Reagents

Xylene, hexadecane, methylcyclohexane and isopropanol were obtained from Sigma Aldrich (Saint Louis, MO, USA) and were of analytical grade.

3.5.1. Thermal bonding of Zeonor-ZF-14

Zeonor foil was thermally bonded based on parameters that were described previously by our research group [82]. Bonding of the Zeonor foil was achieved by placing the structured foil with the drilled holes and an unstructured bottom foil between two quartz glass plates, which were then loaded into the hydraulic press. The upper hot plate was lowered until it was in contact with the upper quartz glass plate but no pressure was applied. After increasing the temperature to 125 °C, a bonding force of 10 kN was applied and kept constant over 10 min. The bonded chip was released after a short cooling period at 100 °C. Bonding with this method often led to insufficient bonding with delaminated areas around the channel; furthermore, the bonding was not very strong and the two foils could readily be peeled apart. To further improve the bonding and level out any unevenness in the press, the bonding stack was sandwiched between either 0.5 mm thick graphite sheets or 1 mm thick rubber slabs, wrapped in aluminum foil. To prevent imprinting of the graphite sheet or aluminum surface into the COP surface, a teflon-coated Si-wafer or polished nickel shims were placed between the aluminum foil and the COP bond stack. The compressible support layers helped to prevent un-bonded areas due to an uneven pressure distribution across

the bonding area, but did not improve the bonding strength. Variation in temperature from 115 °C up to 129 °C in combination with low (7 kN), medium (10 kN), and high (15 kN) bonding forces did not lead to any improvements. It either promoted channel blocking by collapsed sidewalls (high temperature, high pressure) or did not bond at all (low temperature). Thermally bonded Zeonor chips only resisted flow rates of 10 µL·min^{-1} and frequently leaked after a few hours (see Chapter 4 on page 59). Therefore, several surface treatments were applied to improve the bonding strength.

UV/ozone treatment

As reported by Shinohara et al. [69] and Tsao et al. [68], UV/O_3 treatment of Zeonex 480 plates and Zeonor 1020R (T_g = 138 °C) could improve the bond strength and similar experiments were performed with Zeonor foil. Bottom and top foil were placed into a UV/O_3-photoreactor, approximately 2 cm below the UV-grid.

Exposure times were 1 min, 5 min, 10 min and 15 min. After irradiation, the foils were brought into conformal contact and placed between two flat nickel shims. This stack was sandwiched between two 1 mm thick rubber slabs and placed into a pre-heated lab press (T = 125 °C). A constant force of 10 kN was applied for 10 min thereafter the bonded chip was released. UV/O_3 treatment of Zeonor foil caused a moderate change in surface wettability to a contact angle of 40°. Furthermore, Zeonor foil turned yellowish after 5 min exposure and therefore, the optical transmission after UV/O_3 exposure was measured with an UV/VIS spectrometer (UV/VIS 1800, Shimadzu, Kyoto, Japan). The result is shown in Figure 3.7. Upon UV/O_3 treatment the optical transmission changed drastically, falling below 50% in the range from 248 to 320 nm. This makes UV/O_3 treated chips unsuitable for optical detection methods in the UV range. Bonded chips showed stronger bond strength.

When separating the foils, “marks” were left on the surface, indicating a stronger interlocking of the material. Even though the UV/O_3 treatment had a positive effect on the bond strength, the laminated foils could still be separated with little resistance. After further separation of the laminated foils, the non-uniformity of the

bond was revealed (see Figure 3.8). Large transparent areas could indicate a "resistance" to the treatment resulting in a locally lower bond strength.

A 30 s UV treatment with a UV-flood lamp caused already a loss of light transmisssion below 50% in the range from 248 to 330 nm but with no improvement in bond strength. No significant change in contact angle was observed and this method was not further investigated.

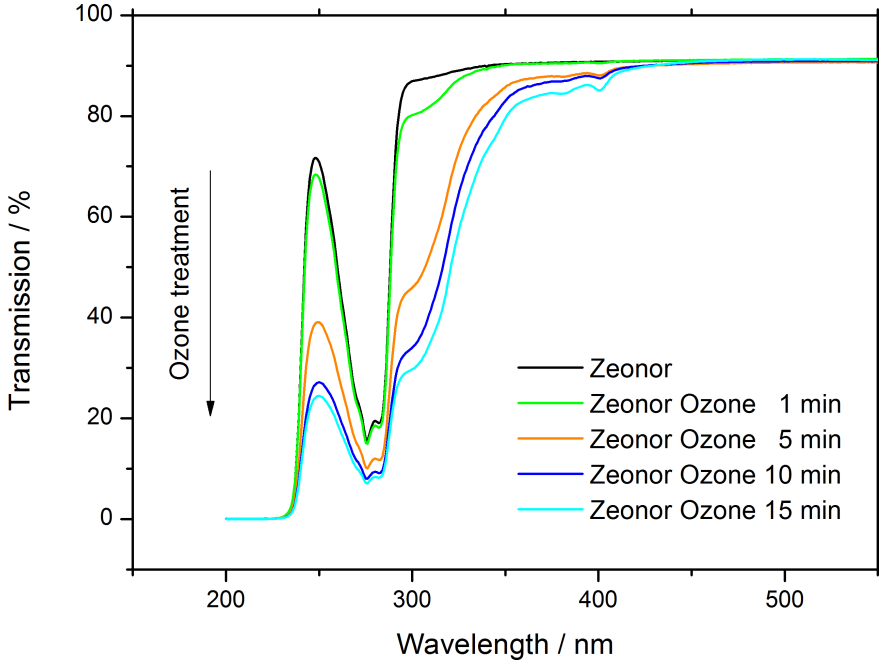

Figure 3.7.: Transmission spectrum of native Zeonor foil, and after UV or UV/O_3 treatment (foil thickness 188 µm). Transmission drops to below 50% in the range from 248 to 330 nm after longtime UV/O_3 treatment. A small decrease was also observed for 1 min UV/O_3 treatment.

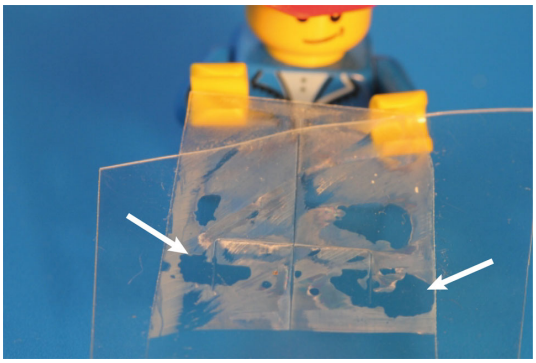

Figure 3.8.: Delaminated chip. Transparent areas show surface regions that were not affected by UV/O_3 treatment.

Oxygen plasma treatment

Plasma treatment of Zeonor foil was performed in an oxygen rich plasma at 50 W with a process pressure of 0.5 mbar. Samples were treated for 100 s and 300 s. The contact angle after plasma treatment was not measurable (<20°), because of the high hydrophilic surface after the treatment. Repeated measurements showed that the plasma treated surface would stay hydrophilic and no contact angle could be measured over 7 days. Bonding of plasma-treated Zeonor samples was performed using the same thermal bonding parameters as already described above ($T = 125\,°C$, $F = 10\,kN$, $t = 10\,min$). No qualitative change in bonding strength was observed for neither of the chosen treatment times, the two mating foils could be separated by peeling with no effort. The plasma treatment did not had an effect on the light transmission.

Solvent-assisted bonding

Xylene ($\delta = 18$ MPa$^{1/2}$)[7] , hexadecane ($\delta = 18$ MPa$^{1/2}$)[7], methylcyclohexane ($\delta = 16$ MPa$^{1/2}$)[7], and isopropanol ($\delta = 23.4$ MPa$^{1/2}$)[7] were chosen for solvent-assisted bonding. Surface activation was performed in two different ways. First an ink-pad like setup was tested:

[7]Hildebrand parameter from: Handbook of Solubility Parameters and Other Cohesion Parameters [83]

a few drops of xylene were dripped on a laboratory tissue and Zeonor foil was pressed against the tissue. Pressing the foil caused immediate cracking and crumbling. Also, diluted xylene with isopropanol (4% v/v) caused cracking after stamping. A second approach was to use a mixture of hexadecane and isopropanol. In this case, the solvent solution was pipetted onto the surface of the unstructured foil and wiped off with a laboratory tissue [84]. Already a solvent mixture of 3.75 % caused crack formation in the material and it was not further investigated. Due to the material failure at direct solvent application, exposure to solvent vapor was tried next. The simple exposure setup consisted of a petri dish filled with solvent and an aluminum holder on top. Unstructured lamination foil was placed on top of the holder and the gap between the polymer surface and the solution was ca. 1 cm. Samples were exposed to methylcyclohexane vapor for 1 min, 10 min, 15 min and 20 min. After exposure, they were pressed together, transferred to a press and bonded for 10 min with two different temperature settings (110 °C and 120 °C). Low exposure times and low bonding temperatures did not show an improvement. Foils could be separated with low resistance. Longer exposure times seemed to promote surface plastification of the Zeonor surface and enhance bonding at the interface. However, bonding results with methylcyclohexane vapor were not very reproducible. Channels often collapsed or the bonding was not uniform due to partial plastification of the surface, similar to the described results for UV/O_3 activation in Figure 3.8. Bonding of thick substrates to Zeonor foil was more successful. Here, 1 mm thick Zeonor slides[8] (Zeonor1420R, $T_g = 136\,°C$) structured with larger microchannels (200 µm × 300 µm) were dipped into methylcyclohexane solution. Excess solvent was wiped off and slides were bonded to Zeonor foil that was exposed to methylcyclohexane vapor using the above method. In contrast, Topas slides[8] (Topas 5013 $T_g = 134\,°C$) were more effected by the solvent vapor treatment than Zeonor slides. They melted after exposure to methylcyclohexane vapor and while bonding at a lower temperature (70 °C).

[8] Injection-molded in-house.

3.5.2. Topas 5013 bonding

In contrast to the weak thermally bonded Zeonor foil, bonding of Topas foil (Topas 5013) at 120 °C, 10 kN for 10 min, resulted in much better bonding strengths. Thermally bonded Topas foils cannot be separated without breaking one of the layers. A 30 s UV irradiation could even further improve the bonding. Sealed microfluidic chips, UV treated and native, could resist fluid flows of 100 µL·min^{-1} without failure due to delamination. The contact angle for Topas foil after UV treatment did not change significantly and the surface remained hydrophobic. As already observed for ultraviolet (UV) and UV/O_3 treatment of Zeonor, the UV treatment changed the UV transmittance of Topas, below 50% light transmittance in the range from 252 to 310 nm. UV/Vis spectra for different treated Topas foils are summarized in Figure 3.9.

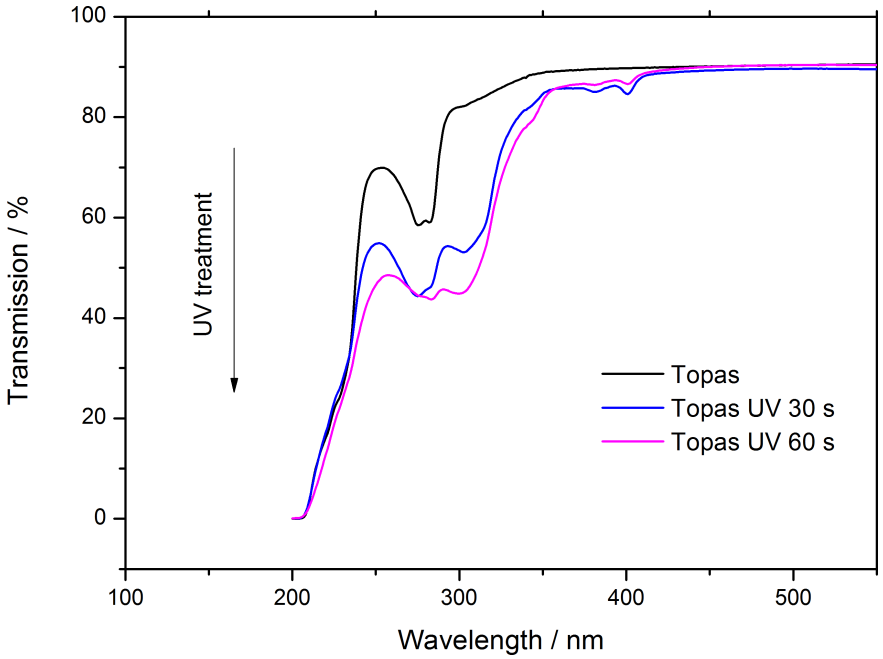

Figure 3.9.: Transmission spectra of native Topas foil and after 30 s and 60 s UV treatment (foil thickness 254 µm).

3.5.3. Razor blade test

The razor blade test is a method, which was first introduced by Gillis and Gilman [85] to evaluate the surface energy of a bonded interface by crack propagation. Maszara [86] further developed it to compare the bond strength of oxidized silicon wafers. In short, a razor blade of thickness t is inserted between two bonded surfaces and the crack length L from the razor blade tip to the first fringe of the crack is measured. With the material specific elastic modulus E, substrate and blade thickness t_s and t_b, the surface energy can be calculated according to:

$$\gamma = \frac{3Et_s{}^3t_b^2}{32L^4} \tag{3.1}$$

The razor blade test was performed immediately after bonding and the crack length was measured, in an inverted microscope (IX71, Olympus Corporation, Tokyo, Japan) equipped with a Canon EOS 550D (Tokyo, Japan).

The Young's modulus for Topas 5013 is 3200 MPa and 2200 MPa for Zeonor1420R[9]. The razor blade thickness was 100 µm and foil thickness was 254 µm for Topas and 188 µm for Zeonor, respectively. The crack length was measured on at least three bonded foils and at different positions. Images for native, oxygen plasma and UV/O_3 treated samples are shown in Figure 3.10. No difference can be seen for native and oxygen plasma treated samples. The foils separate readily, leaving no marks on the surface. UV/O_3 treated samples show a significant difference, as the crack length is shorter compared to native Zeonor, but more importantly, the separation of laminated foils leaves marks on the surface, indicating a stronger interface interaction and hence a stronger bond. The calculated surface energies based on the crack length are summarized in Table 3.5. Here, an increase in surface energy from 12 $J{\cdot}m^{-2}$ to 47 $J{\cdot}m^{-2}$ is calculated.

The results for a razor blade test on bonded Topas foils are also summarized in Table 3.5 and micrographs of the crack after blade insertion are shown in Figure 3.11. The test shows a strong interlock

[9] Young's modulus for ZF-14 is not available. Zeonor1420R is the polymer substrate used for foil extrusion of ZF-14.

of the mating surfaces at the interface, as the crack formation leaves marks on the surface. Calculated surface energies are 243 $J \cdot m^{-2}$ for native Topas and are much higher (1061 $J \cdot m^{-2}$) for 30 s UV-treated foils. The variation in crack length is reflected in a very high error for the measurements, on native Topas and 30 s UV treated Topas foils. The large error might be due to crack propagation from the point of blade insertion to the measurement but it could also be an indicator for imperfections or differences in the surface quality of Topas foils. For qualitative and quantitative results on the effect of UV treatment, more quantitative surface measurements are needed. In addition, the contact angle was measured (Drop shape analysis system DSA10Mk2, KRÜSS GmbH, Hamburg, Germany) right after each treatment and is summarized in Table 3.5.

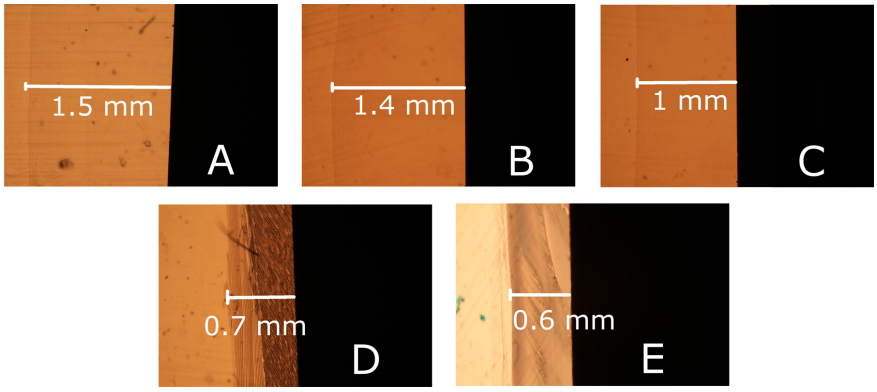

Figure 3.10.: Crack length for different surface treatments. The right black area in every micrograph is the razor blade tip. A) native Zeonor, B) 100 s oxygen plasma treatment, C) 5 min oxygen plasma treatment, D) 10 min UV/O_3 treatment, and E) 15 min UV/O_3 treatment.

3.6. Conclusions and outlook

Cyclic olefin polymer foils can readily be structured by hot embossing with a good reproducability. When it comes to microfluidic devices that require sealed microchannels, Zeonor ZF-14-188 and Topas

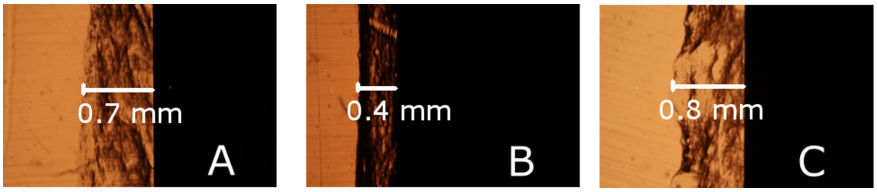

Figure 3.11.: Crack length for different surface treatments. The right black area in every micrograph is the razor blade tip. A) native Topas, B) 30 s UV treatment and C) 60 s UV treatment.

Table 3.5.: Bond strength in relation to surface energy of different bonding methods for Zeonor and Topas foils. Surface energy obtained by razor blade test. Errors as 95% confidence interval.

Surface activation	Surface energy [$J \cdot m^{-2}$]	Error [%]	Contact angle [°]
Zeonor native	12 ± 4	30	101.6 ± 1
Zeonor O_2 plasma 100 s	3 ± 1	33	< 20
Zeonor O_2 plasma 5 min	15 ± 4	27	< 20
Zeonor UV/O_3 10 min	49 ± 6	12	53 ± 5
Zeonor UV/O_3 15 min	38 ± 9	23	56 ± 4
Zeonor UV 30 s	6 ± 2	33	100 ± 1
Topas native	243 ± 129	53	102 ± 2
Topas UV 30 s	1061 ± 644	61	93 ± 6
Topas UV 60 s	198 ± 34	17	101 ± 1

5013L foil microchips differ significantly in their bonding strength. While Topas foil can be bonded using thermal diffusion bonding and can further be optimized by UV treatments, the picture is rather complex for Zeonor foil. Successful bonding strategies for other Topas and Zeonor/Zeonex grades could not be adapted for bonding of Zeonor foil. Even though a surface treatment with oxygen plasma changed the surface wettability remarkably, which might be beneficial for surface modifications in biological microfluidic applications, the bonding quality was not affected. A UV/O_3 and UV treatment of Zeonor and Topas foil could improve the bonding of Zeonor foil and (probably) of Topas, but for the price of UV transmission loss, a key property that makes COP superior to PMMA and PC. While, no non-uniformity was observed in Topas bonded foils, UV/O_3 and solvent vapor bonded Zeonor foils showed areas that seemed not affected by the treatment and thus showed a weaker bond. This effect might be related to the addition of lubricants or an anti-sticking coating, which is commonly applied by the manufactor as a wax-spray coating of polymer pellets before foil extrusion [87] or between protective film and foil. Topas and Zeonor are often said to be similar and the definitions COC and COP are used synonymously for both of them. From the findings during this work they are strikingly different. This hypothesis is also supported by Johansson et al. who found remarkable differences in the XPS-spectra of oxygen treated Topas (Topas 5513X2) and Zeonex (Zeonex 480R) substrates [88]. Furthermore, bonding strategies that are successful for lower T_g COP substrates might not be sufficent for higherer T_g COPs. Where Mair et al. [89] and Olgilvie et al. [73] report very high bond strengths and burst pressures for cyclohexane vapor assisted bonding of Topas 8007 (T_g = 78 °C), their method failed for high T_g Topas grades [73].

COP/COC are extraordinary materials with exceptionally good properties in many areas that are relevant for microfluidic devices, but fabrication and especially reliable bonding methods are not available for all grades and need to be further investigated. A systematic study on different Topas and Zeonor grades is therefore needed to identify bonding strategies that are reliable and easy to reproduce for laboratory prototyping. The razor blade method used during this work is most likely not a reliable method to characterize the bond strength;

the high error in crack length measurements might be due to crack propagation in weakly bonded chips or to handling errors when inserting the razor blade between the bonded interface. Variable bond strength from chip to chip might also be a source but could probably better be investigated by using more reliable testing methods like shear test measurement setups or burst pressure measurements. In general, a standardized burst pressure method for microfluidic devices, like tensile stress measurements in material science could offer better comparison and would lead to a road map for not only COP substrate selection for microfluidic devices.

4. Gold microelectrodes on COP

4.1. Electrochemical detection of pesticides

Dithiocarbamate pesticides are usually analyzed by chromatographic methods, combined with spectrophotometric or mass spectrometric detection methods. While much progress has been made in specific dithiocarbamate (DTC) detection using mass spectrometry [21, 90], the method requires large analytic equipment and cannot be integrated into a lab-on-a-chip (LOC) device for in-field detection. Apart from optical detection, electrochemical detection offers a sensitive alternative that does not require any analyte labelling and can be implemented onto a microfluidic system.

Some approaches for electrochemical detection of DTCs utilize a dropping mercury electrode [91–94] or carbon based electrodes [95, 96] with detection limits for ziram, zineb and thiram in the lower $\mu g \cdot L^{-1}$ range. Dropping mercury electrodes are excellent electrodes, but they cannot be implemented into microchannel systems, beside the fact that mercury is potentially toxic and is therefore not the preferred electrode material. While carbon paste electrodes, especially screen printed electrodes, are gaining popularity, their binding agent will be dissolved in solutions with a high organic solvent content. Although Hernández-Olmos et al. reported difficulties with gold electrodes for DTC detection [96], Sevilla et al. used a rotating gold disk electrode for anodic stripping voltammetry with a detection limit of $0.3\,ng \cdot L^{-1}$[97] and Ngoviwatchai et al. successfully detected different organothiophosphates, a related class of pesticides, using gold electrodes and a two step amperometic detection with a limit of detection below $100\,\mu g \cdot L^{-1}$ [98]. This chapter discusses the fabrication of gold microband electrodes, their characterization in a microfluidic system, and the potential use for electrochemical detection of DTCs.

4.1.1. Microchip with integrated microelectrodes

A key factor for electroanalysis in LOC devices, not only for electrochemical detection but also for electrokinetic driven flow, is the integration of microelectrodes into a microfluidic channel system. While the integration of noble metal electrodes in glass and silicon devices can be adapted from standard cleanroom processes in the semiconductor industry, the integration of metal microelectrodes on polymeric materials is not straightforward. Martin et al. reported a microfluidic chip containing a polydimethylsiloxane (PDMS) micofluidic bottom part and a glass top part with gold microelectrodes [99], and García et al. fabricated a PDMS chip with a microgroove to place a gold microfiber electrode [100, 101]. Direct patterning of metal microstructures on most polymer, glass or Si surfaces requires deposition of a titanium or chromium layer that ensures the adhesion of noble metals, e.g., gold or platinum. Furthermore, polymers like poly(methyl)methacrylate (PMMA) and polycarbonate (PC) cannot be patterned by standard photolithographic processes due to their low chemical resistance or low glass transition temperature. In contrast, gold can directly be deposited on cyclic olefin polymers (COPs) without the need of an adhesion layer [82, 102–105]. COP's high chemical resistance makes it suitable for many chemical processes used in standard photolithography.

4.1.2. Fabrication

Gold microelectrodes were fabricated using photolithography and a lift-off process, which was described by Illa et al. [82]. Prior to photolithographic patterning, 4 inch sized wafers were cut from Zeonor[1] foil and Topas[2] foil, respectively. The film-protected side of Zeonor film was always used as the active side.

In contrast to Topas foil, which is delivered in sheets, Zeonor foil is rolled during delivery and the cut wafers are slightly bent. This curvature will lead to non-uniform photoresist coating and can cause wafer handling errors during automatic processing. To flatten the

[1] ZF-14-188, $t = 188\,\mu m$, $T_g = 136\,°C$, ibidi GmbH, Planegg, Germany
[2] 5013L, $t = 254\,\mu m$, $T_g = 134\,°C$, TOPAS Advanced Polymers Inc., Florence, KY, USA

precut wafers, a 5 min pressing step at 100 °C and 3 kN in a manual laboratory press (P/O Weber, Remshaldern, Germany) was found sufficient. Wafers were either cleaned in an ultrasonic soap bath (30 drops of TritonX-100 solution in 5 L deionized water) or in a three-step ultrasonic bath, starting with acetone, followed by isopropanol and deionized water (each 10 min), and dried in a spin dryer. A 1.5 µm layer of image reversal resist was spin coated directly onto the wafers (SÜSS RC8 spincoater, SÜSS MicroTech AG, Munich, Germany). After softbaking, the resist was exposed to UV light (MA6 mask aligner, SÜSS, MicroTech GmbH, Munich, Germany) through a photomask and the positively patterned resist was baked for 25 min at 120 °C. During this reversal bake, the exposed areas crosslinked and became insoluble in developer solution, while the unexposed areas were still photoactive. A second flood exposure without photomask made these areas soluble in developer and a negative resist pattern remained. Image reversal patterns have a slight undercut, which makes a lift-off process possible. When depositing a gold (Au) layer, here 200 nm, the negatively sloped sidewalls are not exposed to the directional Au deposition and thus the resist structure can be dissolved in an acetone bath. While the resist is dissolved, the Au layer on top of the resist is "lifted-off" the wafer and only areas that were not covered by resist remain. The schematic process is illustrated in Figure 4.1.

Microchip design and experimental setup

The microchip for electrochemical detection consists of a top part that contains the Au electrode structures and a bottom part with the microfluidic channel structure. The channel was either structured by hot embossing (68 mm × 50 µm × 50 µm) in a Zeonor foil, or by micro milling in a Topas slide (68 mm × 220 µm × 500 µm). The electrode top part contains an array of 14 microband electrodes that are 14 µm in width, with 16 µm gaps between the electrodes. Top electrode and bottom channel part were bonded by thermal bonding (Zeonor) or by UV-assisted thermal bonding (Topas), respectively. Before bonding, the electrode array was manually aligned at a distance of 10 mm away from the channel outlet. The electrodes

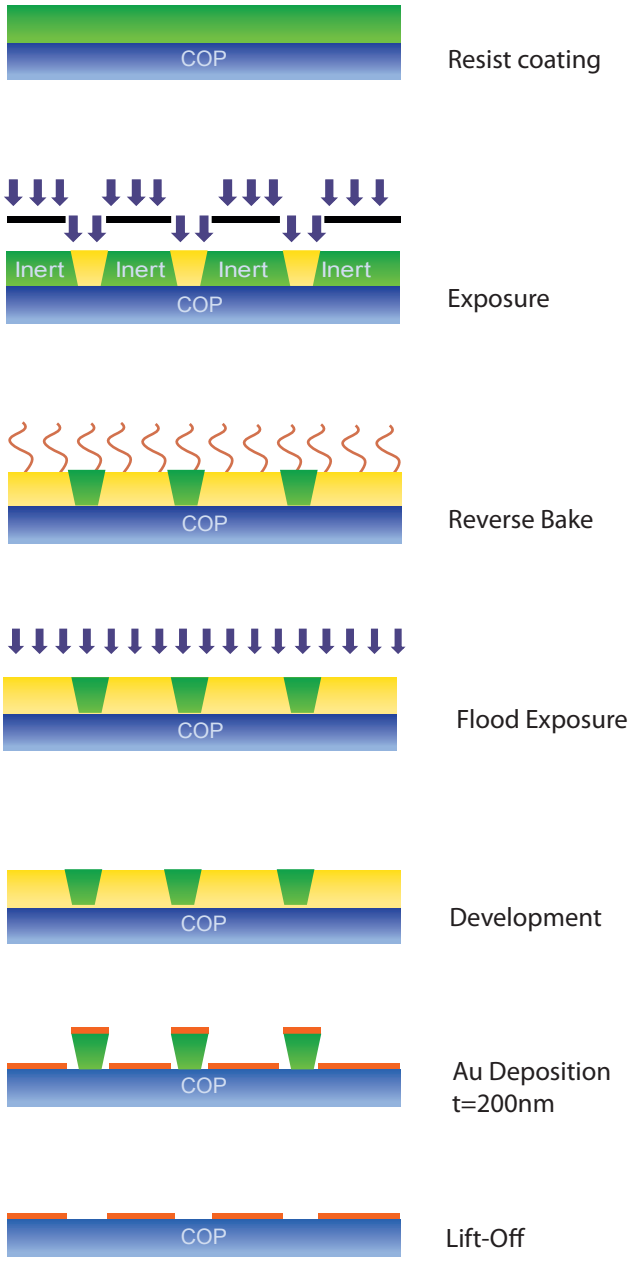

Figure 4.1.: Schematic illustration of the gold microelectrode fabrication. Negatively sloped sidewalls facilitate a lift-off and leave predefined gold structures at the COP surface.

run perpendicular to the channel, so that the active electrode area was determined by the channel width (see Figure 4.2). The chip was mounted in a PMMA/teflon holder that was fabricated by micromilling. Inlet and outlet were sealed with rubber o-rings and connected via microfittings (IDEX Health & Science, Oak Harbor, WA, USA) and silicone tubings (inner diameter = 0.8 mm) to a syringe pump (PHD 2000, Harvard Apparatus, Holliston, MA, USA) and a waste container.

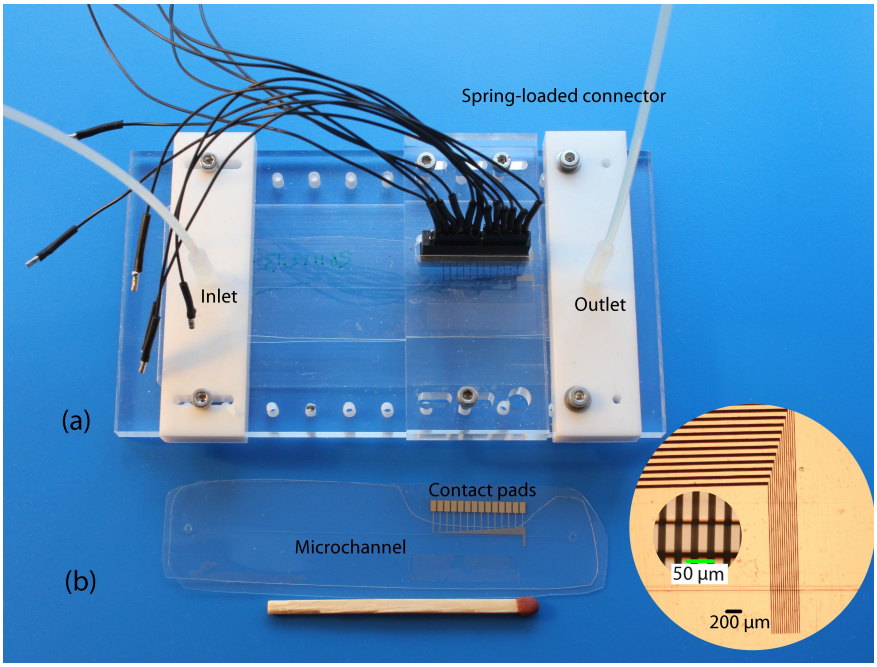

Figure 4.2.: (a) Microfluidic chip setup with tubings and spring loaded connector that connects the potentiostat with three electrodes of the micro electrode array. (b) Microchip, the inset shows a close up of the electrodes. The active electrode area is defined by the width of the microchannel.

A set of three microband electrodes was used as the working, counter, and quasi-reference electrode. The electrodes were connected via a spring-loaded connector (8PD series, Preci-Dip SA, Delémont, Switzerland) that was sightly pressed against the electrode

contact pads. Cyclic voltammetry was performed using a CHI 1010A Potentiostat (Chemical Instruments Inc., Austin, TX, USA). All potentials were measured versus the on-chip gold reference electrode.

Reagents

Potassium hexacyanoferrate(II)trihydrate ($K_4Fe(CN)_6$), potassium ferricyanide(III)($K_3Fe(CN)_6$), potassium nitrate (KNO_3), potassium hydroxide (KOH), sodium tetraborate decahydrate, zincbis(dimethyldithiocarbamate) (ziram), ethylenebis(dithiocarbamate) (nabam) were of analytical grade and received from Sigma Aldrich (Saint Louis, MO, USA). Pesticide standard solutions were prepared freshly by dissolving the appropriate amount of ziram and nabam in methanol (HPLC grade, Sigma Aldrich, Saint Louis, MO, USA) and 0.1 M sodium tetraborate (borate) buffer (with a measured $pH = 8.8$), respectively. 18 MΩ water (Millipore, Billerica, MA, USA) was used for all aqueous solutions.

4.1.3. Results and discussion

Electrode characterization

The Au electrodes were chemically activated by cycling the potential from −1.0 to 1.5 V versus Au in 0.5 M KNO_3 for every new set of electrodes. To characterize the electrode behavior, an equimolar solution of 5 mM $K_4Fe(CN)_6/K_3Fe(CN)_6$ in 0.5 M KNO_3 was pumped through the microfluidic channel with varying flow rates from 2 to 10 µL·min^{-1}. While pumping, the potential was cycled from −0.5 to 0.5 V with a scan rate of 50 mV·s^{-1}. Figure 4.3 shows typical voltammograms that were obtained during the characterization: Fe^{2+} is oxidized to Fe^{3+} and the product is reduced in the reverse scan. The sigmoidal shape of the voltammograms indicates the hydrodynamic nature of the measurement and is typical for the reversible redox system $K_4Fe(CN)_6/K_3Fe(CN)_6$. Furthermore, the limiting current for the system is dependent on the flow rate and increases with increasing flow rate. The system is independent from scan rate, another evidence that the redox process is solely mass-transport dependent.

An example is shown in Figure 4.4 for voltammograms recorded at $4\,\mu L{\cdot}min^{-1}$ and scan rates ranging from 5 to $100\,mV{\cdot}s^{-1}$.

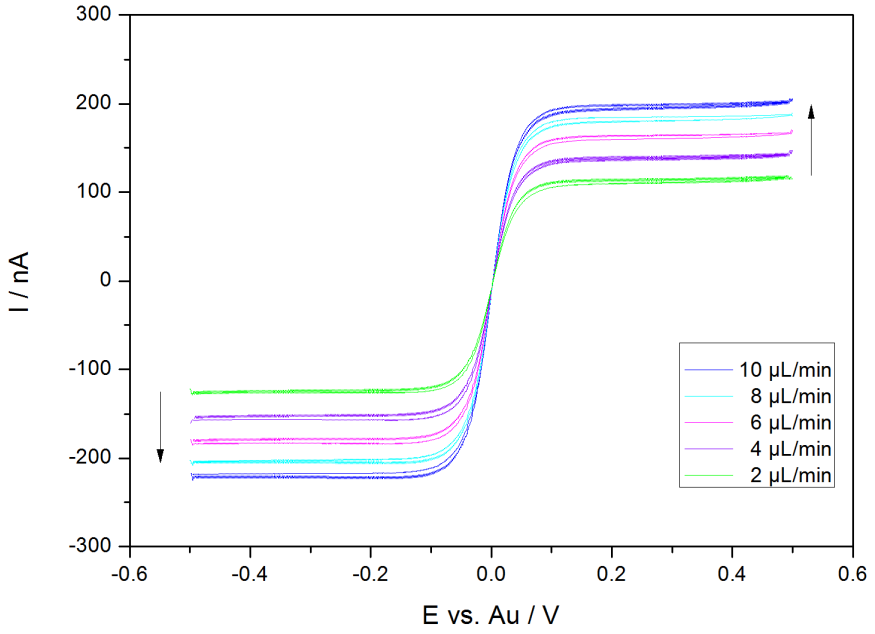

Figure 4.3.: Cyclic voltammograms of 5 mM $K_4Fe(CN)_6/K_3Fe(CN)_6$ in 0.5 M KNO_3. Scan rate: $50\,mV{\cdot}s^{-1}$ for different flow rates, ranging from $2 - 10\,\mu L{\cdot}min^{-1}$.

Further investigations on the limiting current and comparison of measured values to limiting currents, obtained by the Levich equation (Equation (2.19) on page 26) showed the predicted linear behavior (when plotted against the cubic root of the flow rate) but the absolute values were always higher than the calculated ones by Levich (see Figure 4.7). Levich limiting currents were calculated by using the nominal (cross-) channel dimensions of $50\,\mu m \times 50\,\mu m$. SEM[3] micrographs of the bonded channel show dimensions of approximately $45\,\mu m \times 47\,\mu m$ (Figure 4.5), but calculated limiting currents for these dimensions would be even smaller. If we take a closer look at the bonding interface, we notice that the channel corners are slightly

[3]Scanning Electron Microscopy

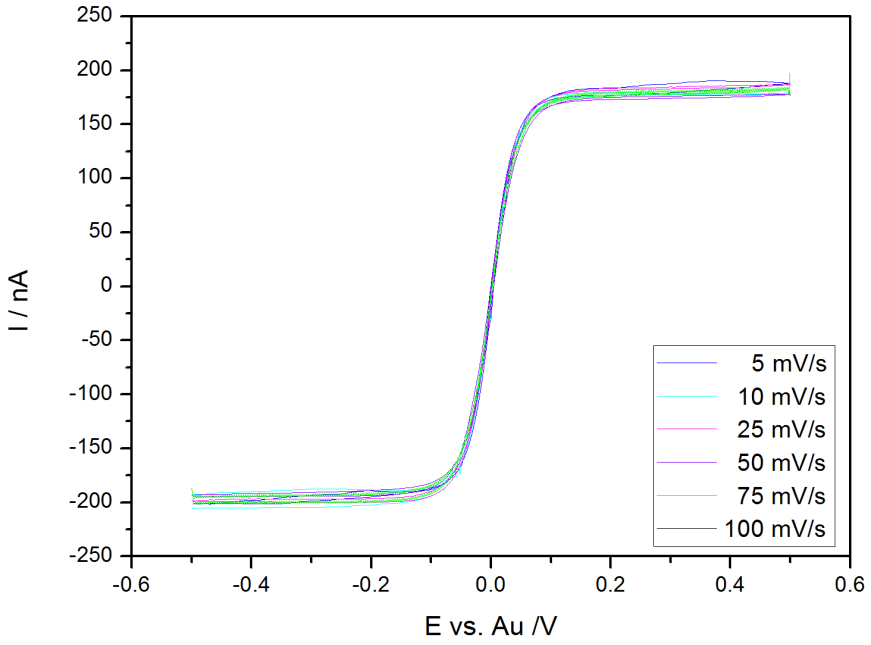

Figure 4.4.: Cyclic voltammogram of 5 mM $K_4Fe(CN)_6/K_3Fe(CN)_6$ in 0.5 M KNO_3. Flow rate: $4\,\mu L{\cdot}min^{-1}$ for different scan rates, ranging from $5 - 100\,mV{\cdot}s^{-1}$. The limiting current is not dependent on the scan rate, error $< 2\%$ of the standard deviation.

rounded and that a small gap between the top and bottom channel can be seen. As mentioned earlier, the electrode length is determined by the channel width or, in this case, the liquid contact area. The length of this gap is approximately 63 µm and limiting currents calculated with these dimensions would give a better fit for the measured currents.

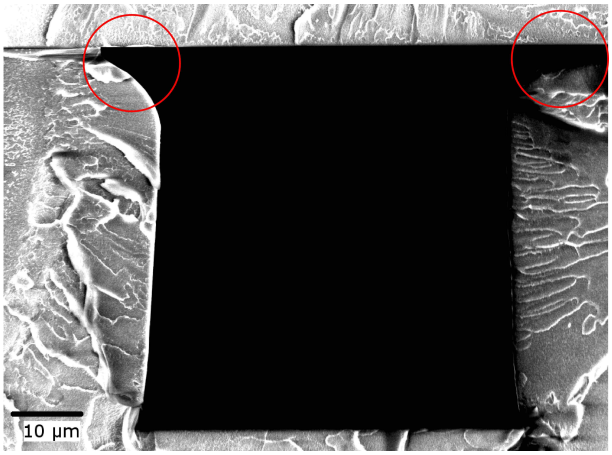

Figure 4.5.: Thermally bonded Zeonor microchip. The bonded interface shows a small gap (red circles), which might be responsible for the higher than expected currents in cyclic voltammetry of $K_4Fe(CN)_6/K_3Fe(CN)_6$.

However, the bond strength of thermally bonded Zeonor chips is very weak and the gap might be caused by delamination so that the active electrode area is not only defined by the channel dimensions. Despite these deviations, cyclic voltammograms with $K_4Fe(CN)_6$/ $K_3Fe(CN)_6$ offer a simple method to assess the functionality of the Au electrode and the active electrode area. They were performed before every measurement to verify the electrode quality.

Extensive measurements, e.g., pesticide studies on thermally bonded Zeonor microchips, were very challenging, as the chips often leaked after or during $K_4Fe(CN)_6$/ $K_3Fe(CN)_6$ characterization. Leakage mostly occurred in areas around the electrode connection, where a localized pressure from the spring- loaded connector might have induced delamination. A different connector, a so called zif connector

(Farnell, Herlev, Denmark) that is slid over the electrodes, similar to connectors know from memory cards in electronic devices, was tested, with the result that the contact pads were scratched off the polymer substrate. The observed difficulties in chip stability led to the bonding tests already described in Chapter 3 on page 31.

Later on, some electrode batches started to show "marks" and were "burned" during measurements, although no changes in experimental parameters were made. A Scotch tape test revealed that electrodes showing these marks had been lifted off whereas other electrodes still adhered to the polymer surface. Chemical residues on the COP surface either from lubricating agents or impurities from the TritonX-100 cleaning, were suspected to prevent optimal adhesion. The Zeonor wafer cleaning procedure was therefore changed from TritonX-100 cleaning to the three step acetone/isopropanol/deionozed water ultrasonic bath clean described before. At the same time, the reproducibilty of the Au electrode fabrication decreased due to a failure in Au lift-off and after extensive process investigation it was found that the e-beam deposition equipment (Wordentec) that was used for Au deposition varied in process temperatures. Sometimes, process temperatures were close to glass transition temperature (T_g), which apparently caused deformation of the thin COP wafer and prohibited proper lift-off. The Wordentec e-beam deposition system can be used in a batch mode and 6 wafers can be loaded at the same time. It was notices that the thermal deformation of the COP wafers increased from the first to the last processed wafer. Aluminum cooling blocks that were placed on top of the wafers could not prevent the deformation. A switch to another e-beam deposition equipment (Alcatel) solved the problem. The wafer – crucible distance in the Alcatel deposition system is larger than in the Wordentec system, in addition it uses a single wafer process, which might have a positive effect on the process temperature.

Electrochemical characterization of pesticides

Microfluidic chips for pesticide detection were made of Topas and had larger channel dimensions (68 mm × 220 µm × 500 µm), but used the same microband electrode design already described for Zeonor chips.

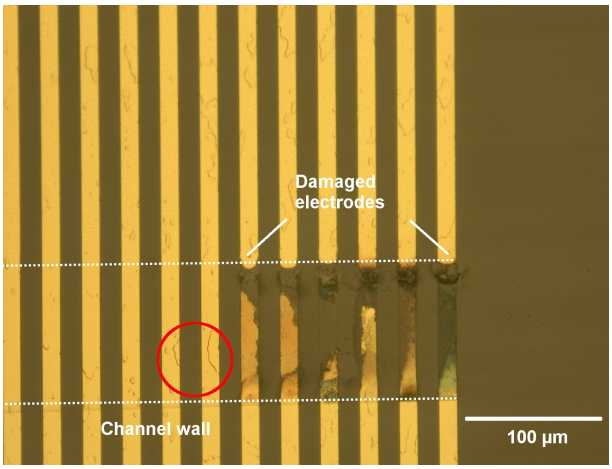

Figure 4.6.: Severely damaged electrodes after cyclic voltammetry. The image shows six damaged electrodes within the microchannel (white dotted line). Black "marks" (red circle) can be seen on the Au surface and might be caused by chemical residues on the polymer surface prior to Au deposition.

The electrode functionality was confirmed by cylic voltammograms of $K_4Fe(CN)_6/K_3Fe(CN)_6$. Residual cyclic voltammograms for 0.1 M borate buffer and a solution of 0.1 M borate buffer and methanol (50% v/v) were recorded. Figure 4.8 shows the typical response of an Au electrode in aqueous solution (black line). On the forward scan, formation of gold oxide occurred at $E \gtrsim 0.6\,\mathrm{V}$ and was followed by oxygen evolution at $E \gtrsim 1.0\,\mathrm{V}$. The reverse scan shows the subsequent reduction of gold oxide at $E \lesssim 0.5\,\mathrm{V}$ (peak at $E \approx 0.3\,\mathrm{V}$) and the reduction of dissolved oxygen at more negative potentials ($E < 0\,\mathrm{V}$). Addition of 50% methanol to the buffer solution seems to slightly suppress the oxide formation and shifts the onset of oxide formation and oxygen evolution to slightly more positive potentials.

A solution of $0.5\,\mathrm{mg{\cdot}L^{-1}}$ nabam in 0.1 M borate buffer was cycled between $E = 0\,\mathrm{V}$ and $E = 1.4\,\mathrm{V}$. The first five repetitive scans are shown in Figure 4.9. The observed response is a two-step anodic oxidation process for nabam that simultaneously with gold oxide formation, but no reduction on the reverse scan is evident. The reduction

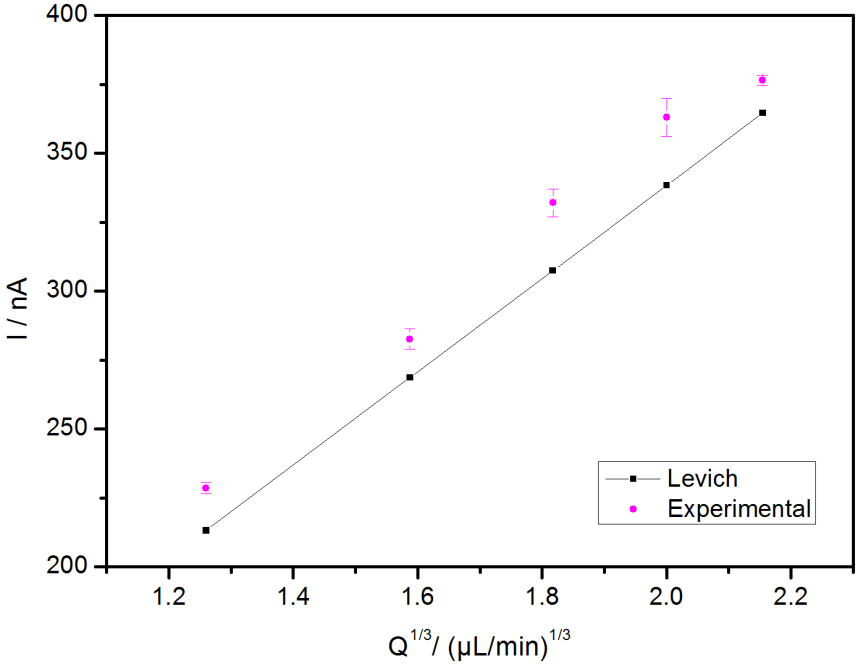

Figure 4.7.: Plot of measured and calculated limiting currents versus the cubic root of the flow rate, for flow rates from $2 - 10\,\mu L \cdot min^{-1}$. The measured limiting currents are higher than the ones predicted by Levich.

peak at $E \approx 0.4\,\mathrm{V}$ corresponds to the reduction of gold oxide. On the forward scan a plateau (1) is established at $E = 0.77\,\mathrm{V}$, and hence this process might correspond to a mass-transport dominated process, whereas the second signal peaks at $E \approx 1\,\mathrm{V}$ and is therefore not (completely) mass-transport dependent. While these first five scans show good reproducibility, following scans with increasing concentrations of nabam showed no linear increase in anodic current. Furthermore, the peak potentials were shifted to more positive potentials. Flushing the channel with buffer solution and repeated potential scans showed that nabam was adsorbed at the gold surface and did only slightly diminish from cycle to cycle (Figure 4.11).

A test with $75\,\mathrm{mg{\cdot}L^{-1}}$ ziram in 0.1 M borate buffer and 50% methanol showed the passivation of the electrode already after five cycles. Furthermore, fouled electrodes could not be reactivated to their initial state, and more reactive cleaning protocols involving flushing with 50 mM KOH and 25% H_2O_2 with a subsequent potential sweep from -0.2 to 1.1 V in 50 mM KOH [106] could not reestablish the electrode surface or caused delamination of gold.

The adsorbtion of organo sulfur compounds to gold surfaces is well known. However, LaCourse and co-workers have described several methods based on pulsed amperometric detection[4], which allows the use of noble gold electrodes for electrochemical detection [107–112]. In short, they suggest to make use of the formation of surface oxide and use it as an oxidative cleaning step. As seen in Figure 4.8, gold oxide is formed at positive potentials during the forward scan. Adsorbed sulfur species, and many other electrode fouling compounds like carbohydrates and amino acids, will be desorbed during this surface oxidation and while the gold oxide passivates the electrode, it is removed when reducing it at more negative potentials, leaving a clean electrode surface. While cycling the potential in cylic voltammetry, we pass through all these steps. First, during the positive scan the pesticide signal appears concomitantly with the oxide formation; this behavior was also reported by Ngoviwatchai et al. [107] and Vandeberg et al. [108] for the sulfur compounds dimethoate and thiourea, respectively. When proceeding further in the forward direc-

[4] A method that applies three potential steps instead of the constant applied potential in conventional amperometry

tion, oxygen evolution takes place, followed by the cathodic reduction of surface oxide that should leave a clean electrode surface. But, as shown in Figure 4.12, the electrode surface was not completely cleaned during the surface reduction and the current response was severely attenuated for repeated scans due to electrode fouling. Similar results could be seen in Figure 4.11, where preadsorbed nabam fouled the electrode and a higher anodic response in repetitive borate buffer scans is observed. On the other hand, the pesticide concentration was relatively high during these scans ($75\,\mathrm{mg{\cdot}L^{-1}}$), which might inhibit the formation of surface oxide and permanently foul the electrode. Tests with lower concentrations in the $\mu\mathrm{g{\cdot}L^{-1}}$ region could give more information about the fouling mechanism.

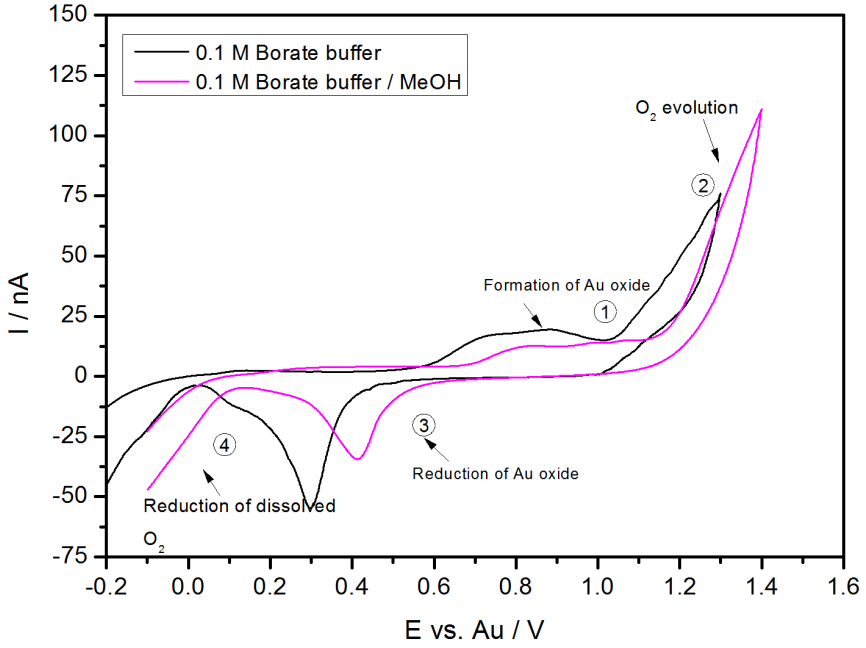

Figure 4.8.: Residual cyclic voltammogram in oxygen-saturated 0.1 M sodium tetraborate buffer and 50% methanol (MeOH). Formation of surface gold oxide and reduction on the reverse scan. Scan rate: $50\,\mathrm{mV{\cdot}s^{-1}}$, flow rate: $20\,\mu\mathrm{L{\cdot}min^{-1}}$.

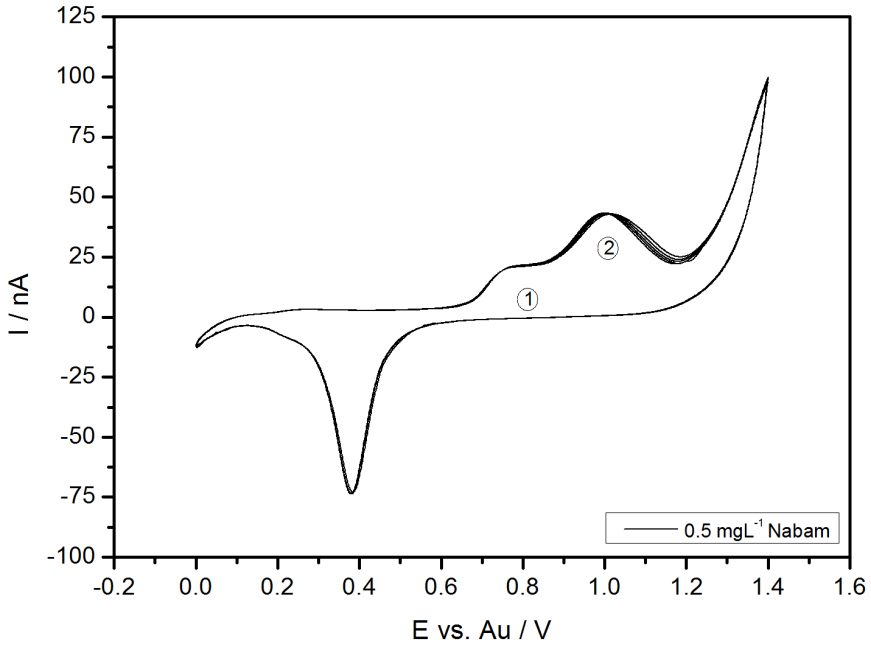

Figure 4.9.: Repeated scans show reproducible results for $0.5\,\mathrm{mg{\cdot}L^{-1}}$ nabam in 0.1 M sodium tetraborate buffer. Scan rate: $50\,\mathrm{mV{\cdot}s^{-1}}$, flow rate: $20\,\mu\mathrm{L{\cdot}min^{-1}}$.

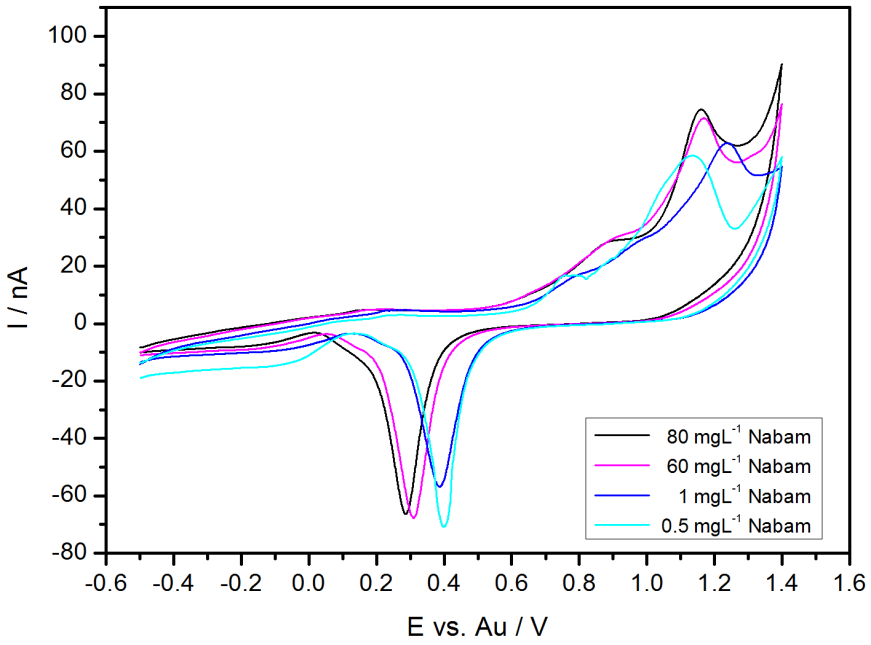

Figure 4.10.: Cyclic voltammetric response for different nabam concentrations. Scan rate: $50\,\mathrm{mV{\cdot}s^{-1}}$, flow rate: $20\,\mu\mathrm{L{\cdot}min^{-1}}$.

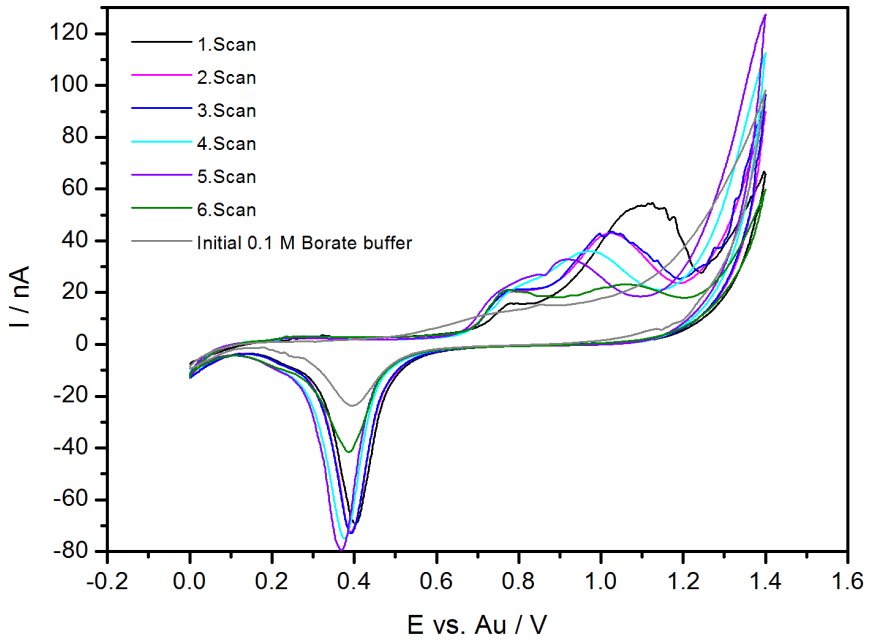

Figure 4.11.: Residual cyclic voltammetric response for repetitive scans of 0.1 M sodium tetraborate buffer after 0.5 mg·L^{-1} nabam detection. Scan rate: 50 mV·s^{-1}, flow rate: 20 µL·min^{-1}.

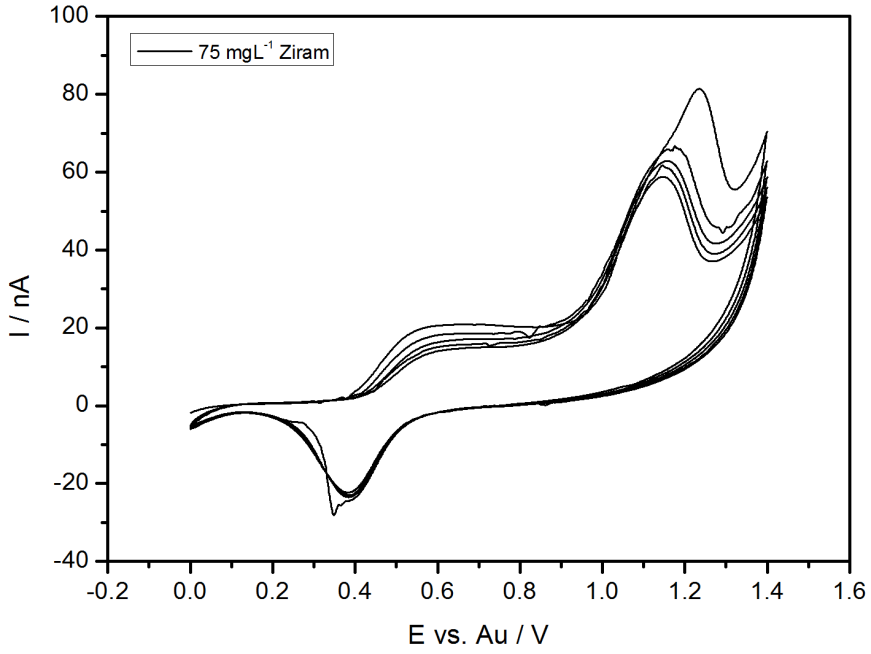

Figure 4.12.: Cyclic voltammetric response for ziram in 0.1 M sodium tetrtraborate buffer and 50% methanol. The graph shows five repetitions. Scan rate: $50\,\mathrm{mV{\cdot}s^{-1}}$, flow rate: $20\,\mu\mathrm{L{\cdot}min^{-1}}$.

4.2. RNA and pDNA extraction from E. coli cells

The COP microchips with integrated gold microband electrodes could further be used in a cooperation project with Tiago Matos, a Ph.D. student from Lund University (Department for Pure and applied Biochemistry, Prof. Leif Bülow). The main idea and the preliminary results are explained briefly in the following section.

E. coli cells are frequently used as host cells, for the extraction of RNA and DNA in biotechnology and pharmaceutical research. While RNA is an important carrier of genetic information and can have regulatory functions, plasmid DNA (pDNA) is especially interesting as a vector for new DNA vaccines, which are currently investigated in clinical trial studies, e.g., for influenza, malaria and HIV [113–115]. The purification and recovery of DNA and RNA is crucial in these research fields for the analysis, characterization and potential synthesis of genetic drugs. The standard protocols for RNA and DNA extraction involve complete lysis of cells in suitable detergents. Further purification involves several centrifugation and filtration steps to retrieve the final RNA and DNA molecules [116, 117]. This expensive and time-consuming procedure needs to be simplified for high throughput analysis and synthesis. Here, LOC devices offer a potential alternative to commonly applied large-scale methods. Lee et al. described a PDMS chip, consisting of a cathode and an anode chamber, separated by a polymeric ion exchange diaphragm, which allows electrolysis of chinese hamster ovary (CHO) cells [118]. Vulto et al. also employed an electrolysis device with an on-chip gel electrophoresis device to purify lysed RNA [119]. While all these approaches used on-chip cell lysis, electropermeabilization of cells is an alternative way to extracting plasmid DNA (pDNA) and RNA from cells without total cell lysis.

The principle is based on electroporation, a mechanisms that is widely used for the transfection of cells. When a cell is in close vicinity of an electric field a cross-membrane potential is developed and water entrance leads to the formation of random pores in the membrane. The cross-membrane potential is amongst others proportional to the applied electric field. When it is above a certain threshold, the electropermeabilization of the cell is irreversible and the cell dies. On

the other hand, if the cross-membrane potential is close to or below this threshold, the electropermeabilization is reversible and the pores will reseal (slowly) when no field is applied (see Figure 4.13) [120, 121]. Electroporation or electropermeabilization is mainly used to introduce molecules into cells, but it can be used as well to extract molecules such as RNA and pDNA from the cytosol into solution without lysis.

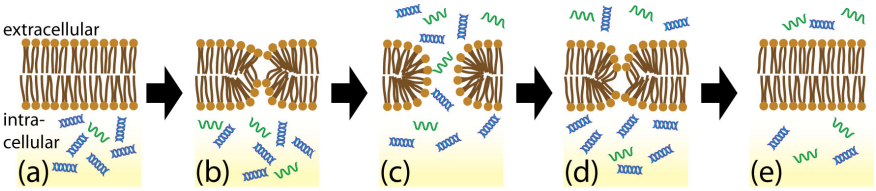

Figure 4.13.: Molecular rearrangement of lipids in the pore edges of the vesicle membrane. (a) Closed bilayer state, molecules are inside the cell. (b) Polarization of the cell membrane and formation of a cross-membrane potential in the electric field. Water entrance into the membrane causes pore formation. Phospholipids will rearrange to minimize the hydrophobic contact. (c) Molecule transition through the open pore. (d) The pore reseals, when no electric field is applied and (e) returns to the initial state.

4.2.1. Microfluidic chip with facing electrodes

The microfluidic chips for electropermeabilization of E. coli cells consisted of a simple three-layer chip design: the microfluidic channel (500 µm wide and 62 mm long) was cut into a 254 µm thick Topas 5013 foil by standard micro milling. Bottom and top layer, each with four arrays of interdigitated gold electrodes, sealed the middle channel layer. The electrode arrays consisted of 10 microband electrodes, which were 560 µm wide, with a pitch of 1120 µm and a length that was defined by the microchannel width, i.e., 500 µm. The electrodes were fabricated on Topas 5013 foil by photolithography, e-beam gold deposition (200 nm), and lift-off as already described in Section 4.1.2 on page 60. The three layers were exposed to UV light (30 s) and manually aligned, so that the interdigitated electrode arrays were

facing each other. They were then thermally bonded in a laboratory press at 120 °C at 10 kN for 10 min. The chip was connected via a homemade PMMA holder and teflon tubings to a HPLC pump (2150, LKB Bromma, Sweden) and a collection vessel, respectively. Bottom and top electrodes were connected to a DC power supply (HQ Power PS1502A, Gavere, Belgium) through spring-loaded connectors (8PD series, Preci-Dip SA, Delémont, Switzerland) in the bottom and top part of the holder. While the cells were pumped through the microchannel a potential was applied between top and bottom electrode so that the cells passed through an electric field. A perspective drawing of the setup is shown in Figure 4.14.

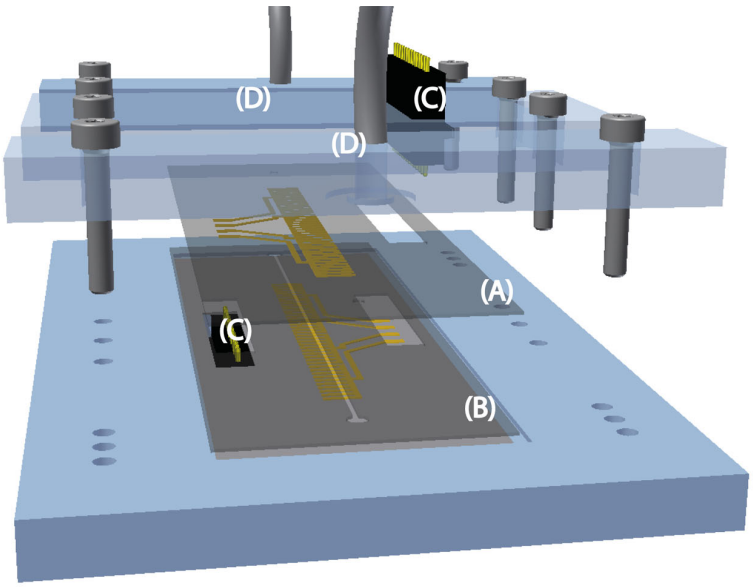

Figure 4.14.: Exploded view of the chip setup. The microfluidc chip consist of three layers,(a)the top layer with four electrode arrays (anode), (b) the middle layer with the cut microchannel and the bottom electrode layer (cathode). The electrode contact pads are connected to a power supply by spring loaded connectors (c). Inlet and outlet of the chip are sealed with o-rings and connected to teflon tubing. The fluidic and electric connection is ensured by tightening the screws.

4.2.2. Preliminary results

The microfluidic chip was used by our collaborators to extract pDNA and RNA from E. coli cells. They investigated the effect of different electric field strengths and found that RNA was already extracted at an applied potential of 0.5 V, and that extractionrates were further increased by raising the potential to 2 V. While no pDNA extraction was observed at 0.5 V, pDNA extraction could be increased with higher potentials (see Figure 4.15). To control the cell viability after electropermeabilization, vital cell colonies were counted and compared to a control sample that passed the channel with no applied electric field. Cells that were electropermeabilized at a low potential remained mostly intact, while mostly RNA could be extracted. Figure 4.16 demonstrates further that the cell viability decreased for potentials above 1 V, probably due to partial cell lysis at higher potentials. The pDNA extraction reached ca. 60% of the typical yield of a traditional Qiagen Plasmid MAXI KIT (Hilden, Germany).

The simple microfluidic chip could, in the long perspective, be used in two different ways: RNA can be extracted from living cells that will stay vital after extraction. The cells could be separated from the extraction product in an additional on-chip separation step and reused in a fermentation process for RNA synthesis. The simple on-chip electropermeabilization could also be an alternative for traditional cell lysis methods. A manuscript that discusses the obtained results in more detail is in preparation.

4.3. Conclusions and outlook

The integration of gold microelectrodes into microfluidic COP chips was shown. It was demonstrated, that the electrodes behave well when characterized with $K_4Fe(CN)_6$/ $K_3Fe(CN)_6$. As expected for a hydrodynamic system the oxidation and subsequent reduction was only dependent on mass transport to the electrode surface and the limiting current was hence dependent on flow rate. Chips that were made of Zeonor foil were prone to leakage due to the weak bonding strength of thermally bonded chips. Although, the electrodes were functioning well, longer experiments that were necessary for pesticde

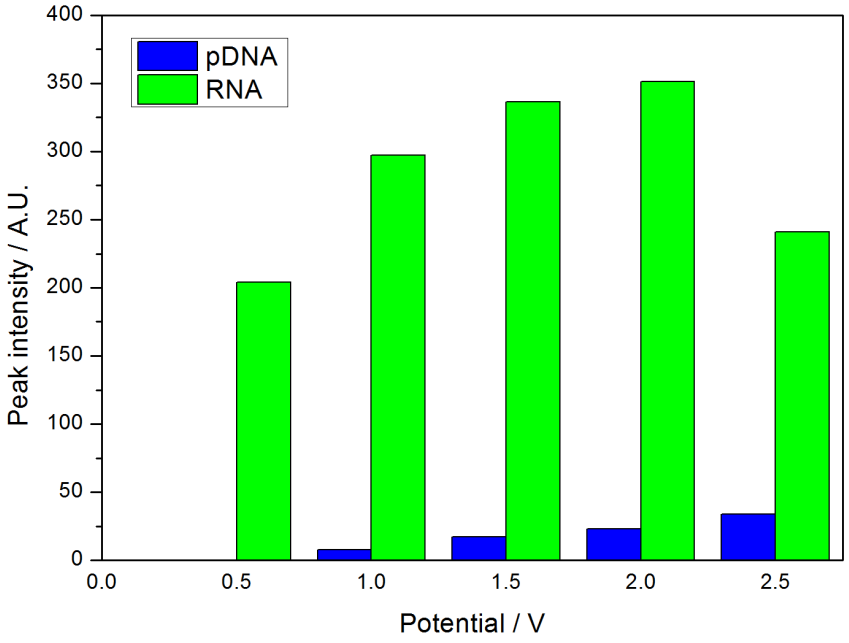

Figure 4.15.: Extracted pDNA and RNA. Extraction increases with rising voltage up to 2 V. The extraction is measured as peak intensity on an agarose gel after electropermeabilization. Buffer medium: 10 mM citrate buffer containing 10 mM sodium chloride, 30 mM glucose, pH 5.8. Flow rate was 200 µL·min^{-1}. Intensity values are corrected for peak intensities that were obtained when no electric field was applied. Figure courtesy of Tiago Matos, Lund University

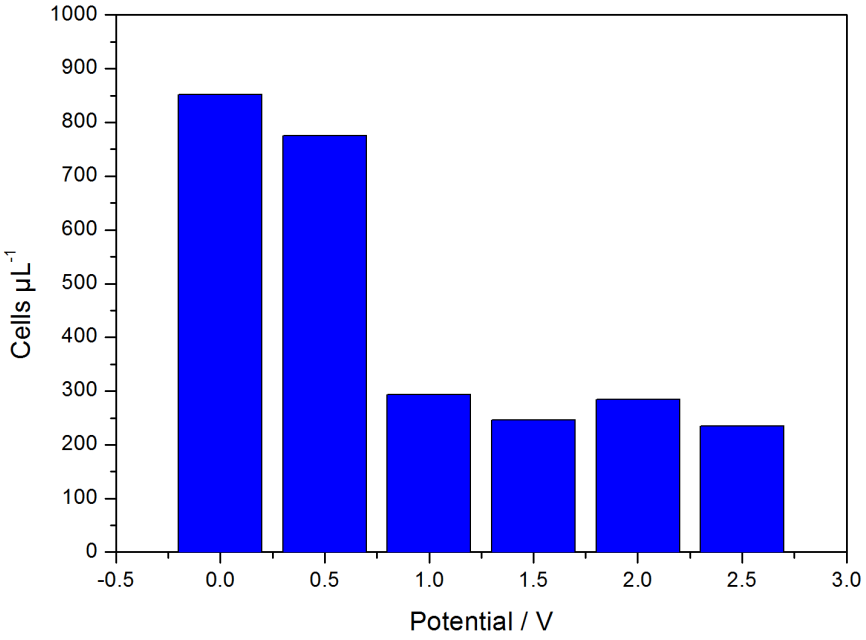

Figure 4.16.: Cell viability after electropermeabilization. A fraction of cells remains intact after permeabilization at 0.5 V applied potential. Above 1 V partial cell lysis is caused. Cell vitality was estimated by counting cell colonies. Figure courtesy of Tiago Matos, Lund University

characterization were not possible which such a short chip lifetime. On the other hand, Topas chips lasted longer and two DTC pesticides were further investigated with cyclic voltammetry. The characterization and subsequent detection of dithiocarbamate pesticides is rather complex: Tests with nabam and ziram showed that they are electrochemically active and could be detected at relatively high potentials $E \gtrsim 1\,\mathrm{V}$.
The oxidation of both nabam and ziram showed a two-step response, with the first step being plateau shaped, whereas the second was suspected to be controlled by surface adsorption and mass transport processes. To confirm the surface control of the process, several additional tests are required. The flow and scan dependency can reveal further evidence of the kinetics and surface processes. Repetitive scans showed that the electrode was readily fouled and reactive cleaning by cycling the potential in buffer solution would take many cycles. To use amperometric electrochemical detection schemes for dithiocarbamate detection, a detection potential needs to be found, e.g., by cyclic voltammetry. Fouling of the electrode would cause false current-concentration response and constant potential amperometry is not useful for detection. A pulsed amperometric detection scheme needs to be developed that consists of three different pulses for detection, oxidative and reductive cleaning. Possible strategies might also include more advanced techniques where a range of detection potentials is swept during the detection step to cover possible potential shifts [42]. Integrated pulsed amperometric detection offers a potential detection pathway, which might circumvent the high background current from simultaneous oxide formation during pesticide detection [42, 111]. To apply the technique, the adsorption and electrochemical response for dithiocarbamate pesticides needs to be studied in further detail, to better understand the fouling process and the potential shifts reported for different concentrations. Characterization will require several electrochemical studies, where different buffer configurations and scan ranges need to be investigated. The described microfluidic device with integrated microelectrodes is probably not suited for these studies in this particular case. Fouled electrodes cannot be replaced or reactivated and hence many microchips are needed which, at this development point, are too fragile to deliver

reliable results for these complex compounds. Here, macroelectrodes would be a better instrument for characterization since they can be mechanically reactivated after fouling. Once the process is better understood, it can be transferred back to the microsystem for actual pesticide detection. However, Topas chips with integrated gold electrodes could successfully be used in a cooperation project for the electropermeabilization of E.coli cells. While the strong affinity of (sulfur containing) dithiocarbamate pesticides for gold might be a challenge in electrochemical detection, it is an important feature for gold nanoparticle mediated detection of the same, which is explained in the next chapter.

5. Gold nanoparticle mediated fluorescence detection

As we have seen in the previous chapter, dithiocarbamate pesticides show high adsorption characteristics on gold electrodes, which caused electrode passivation and made electrochemical detection challenging. The electrode passivation was related to the high affinity of the sulfur containing pesticide to gold. This phenomenon is very well known and several studies have investigated the mechanisms and potential applications of chemisorption of organo sulfur compounds (mostly alkylthiols) on gold surfaces for self-assembled monolayers and further functionalization purposes [122–125]. More recently, surface modifications with dithiocarbamate ligands showed very robust assemblies and seem to stabilize the formation of gold nanoparticles [126–129]. While the strong sulfur-gold interaction of dithiocarbamates can be beneficial to functionalize gold surfaces, it can also be used for a surface mediated detection scheme, to detect dithiocarbamate pesticides. This approach is described in the following sections.

5.1. Gold nanoparticles for pesticide sensing applications

Gold nanoparticles (AuNPs) have been used intensively for a broad range of applications, from modified electrodes to enhanced optical detection pathways [130–132]. Their size-dependent optical properties have, amongst others, been used for the colorimetric and fluorescent sensing of heavy metal ions, such as mercury [133–135], with limits of detection as low as $0.1\,\mu g{\cdot}L^{-1}$ [135]. While the colorimetric sensing principle is based on particle aggregation in the presence of mercury ions, the fluorescent assay follows two different mechanisms. In a "turn-off" sensor, mercury quenches the fluorescence from highly fluorescent bovine serum albumin functionalized gold nanoclusters

[136]. A reverse principle is employed in the "turn-on" assay, where the fluorescence of rhodamine is quenched by the AuNP [1] as it adsorbs onto the gold surface. The strong interaction between mercury and gold leads to a release of rhodamine into the bulk solution and concomitant fluorescence recovery [133].

More recently, colorimetric AuNP based assays found applications in pesticide monitoring of organophosphorours and carbamate pesticides [140–144]. Most AuNP based sensors make use of the well known acethylcholine esterase (AChE) inhibition by these pesticides [145]. Lin, Virel, Liu and co-workers describe a colorimetric sensor, whose response is modulated by thiocholine (TCh), a product that is hydrolyzed by AChE, and acetylthiocholine. The presence of TCh will cause the aggregation of AuNP, which results in a color change of the AuNP probe. The TCh hydrolysis is suppressed if a pesticide is present that inactivates AChE. Sensors for paraoxon reached a limit of detection (LOD) of $13\,\mu g{\cdot}L^{-1}$ (45 nM) [143] and $1\,\mu g{\cdot}L^{-1}$ (4 nM) [141], respectivley. Liu et al. used the same approach, but combined it with a second fluorimetric "turn-off" sensing scheme: AuNP are functionalized with rhodamine B and will aggregate when thiocholine (no pesticide present) is adsorbed. Furthermore, rhodamine molecules are released, and their fluorescence is restored. This dual sensor offered LODs in the low $\mu g{\cdot}L^{-1}$ range for diazinon ($0.1\,\mu g{\cdot}L^{-1}$), malathion ($0.1\,\mu g{\cdot}L^{-1}$), phorate ($0.3\,\mu g{\cdot}L^{-1}$) and carbaryl ($1\,\mu g{\cdot}L^{-1}$) [144]. While all these sensors make use of the high affinity of the hydrolyzed sulfur containing thiocholine to gold a simpler detection scheme can be adapted for the sulfur containing dithiocarbamate (DTC) pesticides without the necessity for enzymatic catalysis.

The AuNP based sensor that was used in this thesis is adapted from Huang, Chen and co-workers [133, 146] and is based on the fluorescence quenching of rhodamine 6G (R6G) molecules adsorbed onto the surface of AuNPs. R6G was choosen over Rhodamine B for its higher fluorescence quantum yield and photostability in solution [146]. In basic tetraborate buffer, at a $pH = 9$ the positively charged

[1] Fluorophore quenching by AuNP's has been extensively studied and is related to electrostatic interactions and internal electron and energy transfer mechanisms [137–139].

R6G molecules adsorb via electrostatic interaction at the surface of negatively charged AuNPs. Upon the addition of DTC, the sulfur containing pesticides interact with the gold surface of the particles and displace the R6G molecules. The released R6G will restore its native fluorescence and the fluorescence intensity can be a measure for the pesticide concentration. Figure 5.1 illustrates the sensing schematic for this "turn-on" approach.

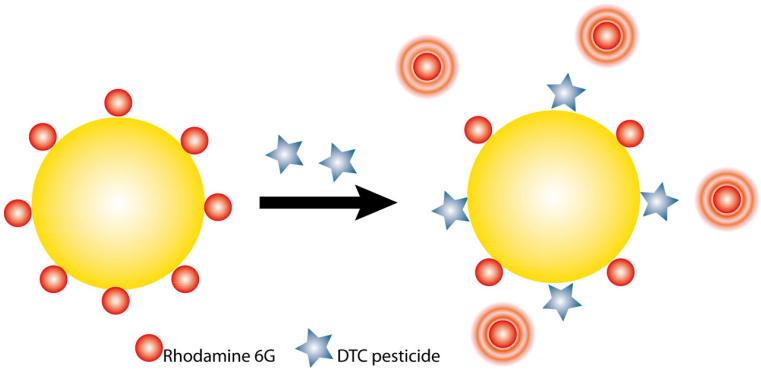

Figure 5.1.: Schematic illustration of the "turn-on" AuNP mediated detection scheme. The fluorescence of rhodamine 6G molecules (red circles) is quenched when adsorbed onto the gold surface and are released into the bulk solution after addition of dithiocarbamate molecules (blue star). Upon displacement, they restore their native fluorescence, which can be used as a measure for the pesticide concentration.

5.2. Chip design

The microfluidic chip is designed to mix different pesticide concentrations and the AuNP sensing probe on the chip (see Figure 5.2). The three inlets allow individual flow control of the analyte and sensing probe. Due to the small channel dimensions (300 µm wide $\times$100 µm deep, Gaussian profile), the flow is in the laminar regime ($Re \approx 2$) and mixing of the laminating fluids is dependent on diffusive transport. The overall length of the channel is 18 cm which allows for sufficient mixing before the detection cell is reached.

The microfluidic chip was fabricated out of three polydimethylsiloxane (PDMS) slabs (thickness = 1.5 mm). These slabs were cast in poly(methyl)methacrylate (PMMA) molds using the Sylgard-184 elastomer kit (Dow Corning, Midland, MI , USA). The middle layer was structured by laser ablation (50 W, Duo-Laser CO_2 laser, Synrad, Mukilteo, WA, USA) from both sides: first the waste channel (dashed line, figure 5.2) was structured, afterwards the slab was flipped to structure the flower-shaped channel. Top and bottom channel are connected through a 100 µm wide hole (red dot) that was drilled through the PDMS slab by pulsing the laser. Any debris from the laser ablation was removed by manually cleaning the structures with soap water, flushing with isopropanol and drying with nitrogen. The structured middle layer is bonded to the top and bottom slabs by exposing the respective sides for 90 s to an oxygen plasma (50 W, 13.56 MHz, atto Plasma, Diener Electronic, Ebhausen, Germany) and subsequent baking at 90 °C in a convective oven for 20 min.

5.3. Experimental setup

The PDMS chip was connected to a high precision syringe pump (neMESYS, Cetoni GmbH, Korbussen, Germany) by a homemade fluidic connector via teflon tubings (inner diameter = 0.8 mm) and microfittings (idex Health & Science, Oak Harbor, WA, USA)(figure 5.3). AuNP probe, pesticide solution and water were mixed on chip.

To mix different concentrations of pesticides on-chip, the flow rates of pesticide stock solution and water were altered between 0 and 4 µL·min^{-1}, while the AuNP probe's flowrate was kept constant at 6 µL·min^{-1}. The total flow rate was 10 µL·min^{-1}. Fluorescence micrographs were taken on an inverted microscope (IX71, Olympus Corporation, Tokyo, Japan) equipped with a fluorescence lamp (X-Cite 120, EXFO Photonic Solutions Inc., Mississauga, Ontario, Canada) and a digital camera (EOS 550D, Canon, Tokyo, Japan). The detection cell was excited at 20× magnification ($N.A. = 0.45$), using a filter block with $\lambda_{emission} > 590$nm and $\lambda_{exitation} \approx 510 - 550$ nm. Images were taken, 15 s apart, with an integration time of 3 s and a sensor sensitivity of ISO 400. Between the images, the shutter to the light source was manually shut to prevent photobleaching of the

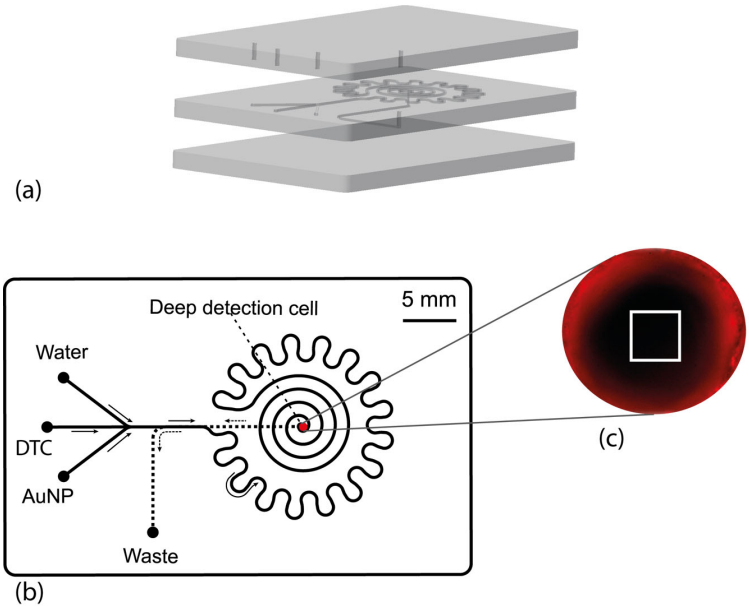

Figure 5.2.: (a) Bonding stack with structured middle layer and sealing top and bottom layer. The top layer contains holes for the fluidic connection.(b) Schematic drawing of the PDMS chip for AuNP-mediated fluorescence detection. While the flow rates of the pesticide (DTC) and water are varied to mix different pesticide concentrations on-chip, the AuNP flow rate is kept constant, as is the total flow rate in the system. Diffusive mixing takes place in the 18 cm long meandering and spiral channel. Fluorescent micrographs are taken from the detection cell (red dot) and the sample passes through the bottom waste channel. (c) A typical micrograph, that indicates the area for fluorescence measurement within the cell (white square). The dimensions of the square are 500×500 pixel $\approx 50 \times 50\,\mu$m.

probe while mixing in the channel. The resulting fluorescence intensity was measured by taking 14 bit RAW images of the detection cell and converting the RAW images into a Matlab compatible TIFF format with no compression. Afterwards, the average red intensity from a square inside the cell was determined using a Matlab script (MathWorks, Natick, MA, USA). A typical image is shown in figure 5.2 (c), where the white square marks the averaging area. Drilling the detection cell through the PDMS slab by laser ablation resulted in a rough surface around the cell edges, which is reflected in the high auto fluorescence at the rim of the cell.

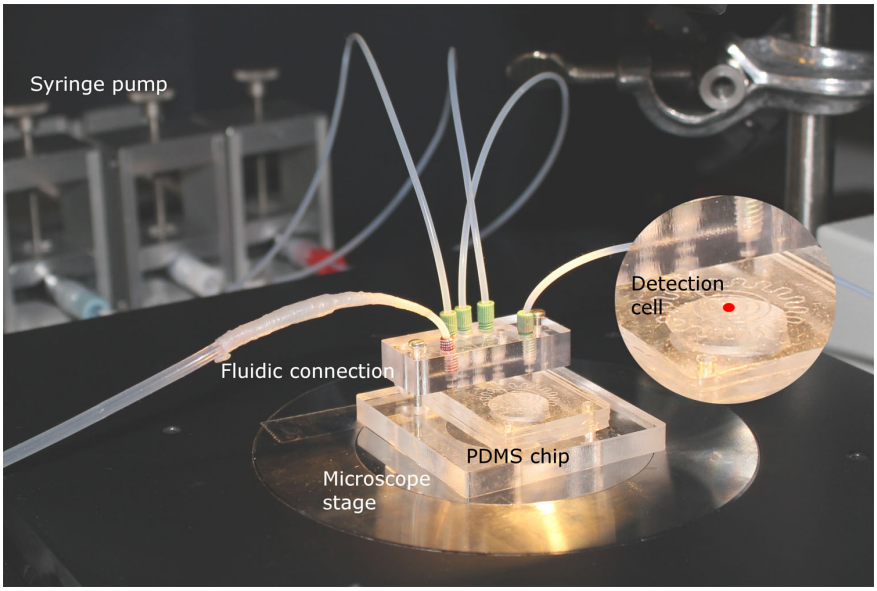

Figure 5.3.: The fluorescent measurement setup. Fluidic connection to a syringe pump allows individual fluidic control of the three different solutions. The content of the cell is excited with green light through the bottom of the stage of an inverted microscope.

Reagents

Chlorauric acid ($HAuCl_4$), rhodamine 6G (R6G), trisodium citrate dihydrate, sodium tetraborate decahydrate, methanol and acetoni-

trile were of analytical or HPLC grade and obtained from Sigma Aldrich (Saint Louis, Mo, USA). Pesticide stock solution ($50\,\mu g{\cdot}mL^{-1}$) of zinc bis(dimethyldithiocarbamate) (ziram) and iron(III) dimethyldithiocarbamate (ferbam) (Pestanal, Sigma Aldrich, Saint Louis, MO, USA) were prepared by dissolving 2.5 mg ziram in 50 mL methanol and 2.5 mg ferbam in 50 mL acetonitrile. Stock solutions were protected from light and stored at 5 °C. Appropriate working solutions were prepared freshly by diluting stock solutions with water. All aqueous solutions and dilutions were made with 18 MΩ water (Millipore, Billerica, MA, USA). The measured pH of 5 mM sodium tetraborate (borate) buffer was $pH = 9.14$.

Gold nanoparticle synthesis and size determination

AuNP were synthesized by the Frens-Turkevich method [147, 148] with modifications described by Grabar et al. [149]. 100 mL of 0.25 mM $HAuCl_4$ was brought to boil in a round bottom flask, equipped with a reflux condenser and submerged into a heated mineral oil bath (160 °C). 7.5 mL sodium citrate (38 mM) was rapidly added to the vortex of the solution and was stirred vigorously for 10 min. While stirring, a color change from pale yellow to burgundy was observed. After removing the flask from the heat, the AuNP solution was stirred for additional 15 min and left to cool to room temperature.

UV/Vis spectra of the AuNP solution can be used to estimate the average particle diameter and concentration by comparing the surface plasmon resonance peak to the absorbance peak at $\lambda = 450$ nm [150]. The average particle size of the synthesized AuNP was determined to be 23 nm with a concentration of 0.6 nM. AuNP solutions were stored in the dark and working solutions were prepared daily by diluting 2.5 mL AuNP solution to 5 mL with 5 mM borate buffer. 5 µL of 0.2 mM R6G solution was added to the working solution, which was then stored in the dark and left for 2 h to equilibrate. The R6G functionalization of AuNPs was optimized to prevent particle aggregation and a R6G/AuNP molar ratio of 600 to 700 was found best.

5.3.1. Fluorescence detection of ziram

Figure 5.4 depicts the fluorescence enhancement by the "turn-on" approach for ziram detection. Cell (a) is filled with R6G-AuNP probe and exhibits very weak fluorescence, whereas the content of cell (b) shows bright red fluorescence due to the addition of ziram to the R6G-AuNP probe and consequent release of R6G into solution. Again, the red rim around the cells is caused by the autofluorescence of the material.

Ziram calibration curves were obtained by mixing ziram working solution in different ratios with water, and a constant flow of R6G/AuNP probe. The laminated flow passed through the meandering channel with a total flow rate of $10\,\mu L \cdot min^{-1}$ while mixing by diffusion. The flow rate ratios for pesticide and water were changed in steps of $0.25\,\mu L \cdot min^{-1}$ and after each change of the flow rate, the flow was left for stabilization (10 min) before fluorescent micrographs were taken.

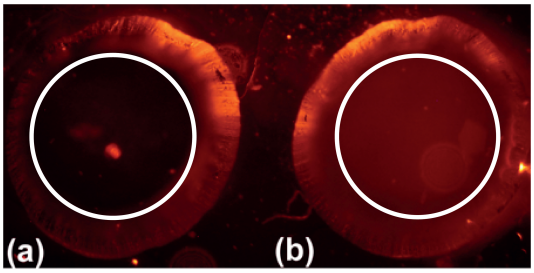

Figure 5.4.: Fluorescence micrographs of two PDMS cells, filled with (a) R6G-AuNP probe and (b) R6G-AuNP probe with a ziram solution, concentration $100\,\mu g \cdot L^{-1}$. The cells are marked with a white ring, the sample with the pesticide appears red due to the fluorescence signal of the released R6G.

The calibration curve for ziram in figure 5.5 was obtained by first diluting a $300\,\mu g \cdot L^{-1}$ ziram working solution by on-chip mixing of concentrations ranging from 0 to $120\,\mu g \cdot L^{-1}$. A second run with a ziram working solution concentration of $500\,\mu g \cdot L^{-1}$ covered the concentration range from 88 to $200\,\mu g \cdot L^{-1}$. The calibration curve represents the average fluorescence intensity from $n = 5$ measurements for each

ziram concentration. It is linear in the range from 16 to 150 µg·L^{-1} with a LOD of 16 µg·L^{-1} (determined as $3\sigma_{blank}$) and with the limit of linearity at 150 µg·L^{-1}. While the fluorescent sensing of ziram showed excellent results with a low detection limit and a wide linear range, a potential second colorimetric detection mechanism was investigated. Figure 5.6 shows samples of three different R6G-AuNP probes. The solutions are mixed by diluting 1 part of AuNP solution with 1 part water or ziram solution. A distinct color change from red (0 µg·L^{-1} ziram) to blue (500 µg·L^{-1} ziram) could be seen and could serve as an alternative detection mechanism.

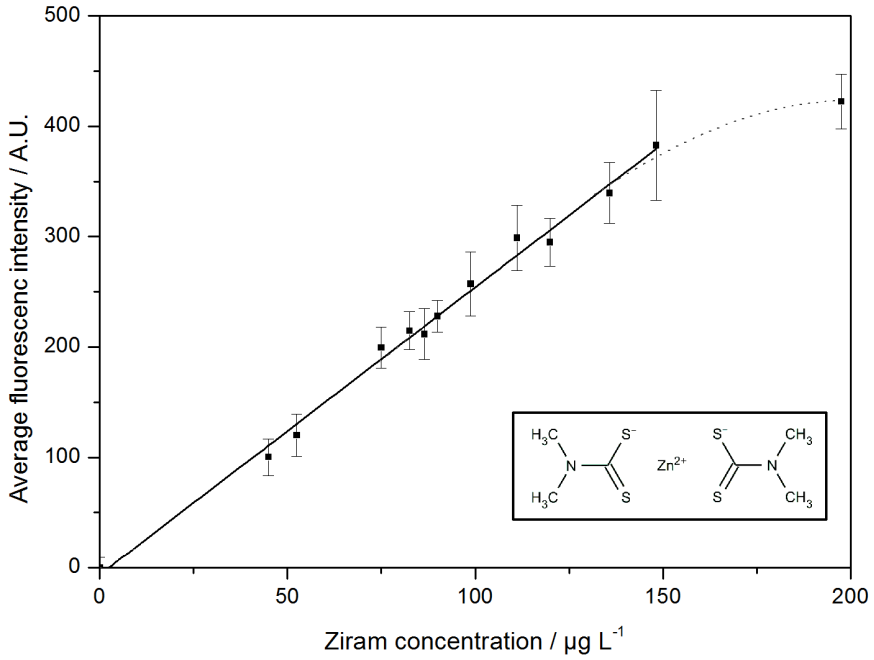

Figure 5.5.: Calibration curve for detection of ziram. Linear regression coefficient $R^2 = 0.99(3)$, with the limit of linearity at 150 µg·L^{-1}. The limit of detection is 16 µg·L^{-1} (calculated as $3 \cdot \sigma_{blank}$). Error bars are shown for the 95% confidence interval, error <2%. Inset: drawing of the chemical structure of ziram [151].

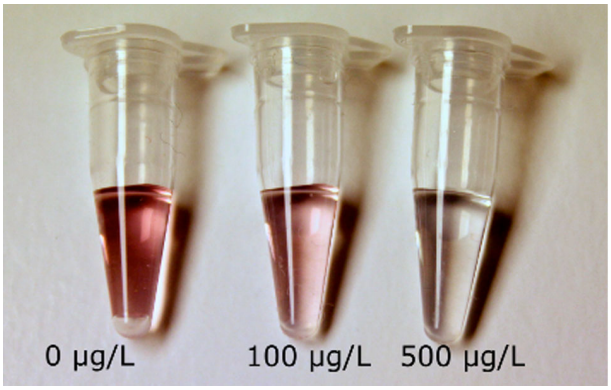

Figure 5.6.: Gold nanoparticles aggregate upon addition of ziram. Color change of the AuNP probe from red, no ziram added, to light red, 100 µg·L^{-1} ziram concentration, to blue/transparent, 500 µg·L^{-1} ziram concentration, could be seen.

5.3.2. Fluorescence detection of ferbam

After obtaining very promising results for the ziram detection, a second DTC pesticide, ferbam, was tested with the same method. A 300 µg·L^{-1} working solution was prepared by diluting a 50 mg·L^{-1} ferbam stock solution with 18 MΩ water. The same settings as already described for ziram detection were employed and the curve displayed in figure 5.7 illustrates the obtained result. The series is linear (correlation coefficient $R^2 = 0.99(9)$) in the measured range from 45 to 90 µg·L^{-1}. A linear fit reveals a significant offset at the y-intercept with ≈ 860 A.U. of the blank measurement. This offset might be induced by several factors:

The fluorescence micrographs were taken with a digital SLR[2] camera that is designed for photographic applications. With these cameras, the sensor data can be accessed from a RAW image format, where the raw unprocessed intensities of each red, blue and green pixel are saved. For a 14 bit RAW image, every sensor pixel can distinguish intensity values from 0 to $2^{14} = 16384$. Raw images that were taken with the Canon digital camera had a smaller range: mea-

[2]Single-Lens Reflex

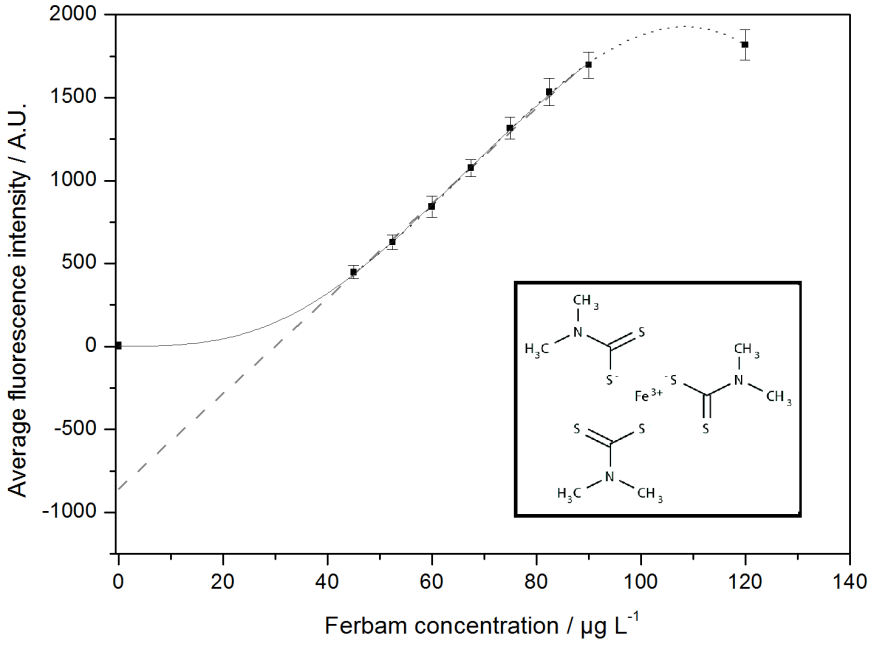

Figure 5.7.: Calibration curve for ferbam. The curve is linear in the range from 45 to 90 µg·L^{-1} with linear regression $R^2 = 0.99(9)$ and limit of linearity at 120 µg·L^{-1} (dotted line), but with a y-intercept at a value ≈ 800 units below the blank measurement (dashed line). Error bars shown for the 95% confidence interval, error $\leq 2\,\%$. Inset: drawing of the chemical structure of ferbam.

surements of black images, i.e. no light onto the sensor still reached red intensities of 2100 where 0 was expected. Red saturation was determined at 15 300 instead of 16 384. While the sensor saturation at bright values was never reached during fluorescence measurements, the cut-off at dark values was very close to the measured intensities of the blank signal. This might be a reason for the "too high" blank value in figure 5.7. Even though, images in RAW format should display the unprocessed data, there might be an internal camera algorithm that balances intensities. Reference measurements with a photomultiplier tube or a highly sensitive laboratory camera could give further information. Furthermore, the fluorophore response might not be linear at low concentrations, which would result in the observed offset. When we compare the fluorescence intensities of the ferbam and ziram measurements, ferbam produces an almost 3-fold higher fluorescence signal, at equivalent concentrations, than ziram. The chemical structure of ferbam differs from ziram in that it consist of three dithiocarbamate groups and an iron(III) central ion. While the sulfur groups interact with the gold surface, iron(III) might be released into solution or might already be present as a decomposition product from the unstable ferbam. The presence of iron(III) in combination with AuNPs might interfere with the measurements, which could cause the high offset [152, 153] that was not observed for ziram measurements.

5.4. Conclusions and outlook

It was demonstrated that the "turn-on" approach for AuNP mediated mercury detection could successfully be transferred to the detection of dithiocarbamate pesticides. A sensitive microfluidic sensor with a limit of detection as low as 16 $\mu g \cdot L^{-1}$ for ziram was developed. Even though ferbam detection showed a fluorescence off-set during measurements it was demonstrated that the gold nanoparticle mediated sensor would not only respond to ziram but also to another dithiocarbamate pesticide. The strong sulfur-gold interaction caused the release of R6G into solution and might be common not only to ziram and ferbam but also other dithiocarbamate pesticides. The low detection limit and the wide linear range makes this detection scheme

a potential alternative for rapid on-field monitoring of DTCs. The conventional CS_2-based detection method is circumvented and R6G-AuNP probes can easily be mixed on-chip without the need of more complex enzyme-modified AuNPs. For foodstuff analysis, the sensor needs to be transferred to a non-aqueous system, to analyze more dithiocarbamate pesticides that will precipitate in aqueous solutions. In combination with an on-chip separation of different pesticides this could provide a sensitive sensor for food quality monitoring. The simple microfluidic device could be used in conjunction with smaller consumer electronics such as a smartphone, to provide a simple and portable device for on-field detection. Beside the fluorescent sensing properties, a colorimetric detection could additionally be applied to distinguish dithiocarbamate (aggregation) from mercury (no aggregation) in environmental monitoring application, but this needs further investigation. Gold nanoparticle mediated detection is a very promising sensing scheme, not only for (dithiocarbamate) pesticides and other environmental contaminants such as mercury, it also offers an alternative to conventional electrochemical or absorbance methods, employed in lab-on-a-chip systems.

6. Thiol-ene microchips for capillary electrophoresis

Integration of capillary electrophoresis (CE) onto microchips is one of the most successful implementations of miniaturized analysis techniques onto microfluidic devices. Most common detection schemes in CE utilize UV-absorbance or laser-induced fluorescence detection where non-fluorescent analytes need to be labeled prior to separation. The integration of the previously described gold nanoparticle (AuNP) mediated detection into a CE microchip could offer an alternative to fluorescent dithiocarbamate (DTC) detection without labeling. The detection of DTC with AuNP is non-selective and thus a separation is required to analyze several DTC pesticides.

6.1. Thiol-ene

Thiol-ene polymers are polymers that can be crosslinked in a step-growth polymerization, where both sulfhydryl containing monomers (thiol) and alkenes (ene) are consumed in a stoichiometric ratio [154]. The photopolymerization is initiated at $\lambda = 365\,\mathrm{nm}$ in the presence of a photoinitiator, which photochemically generates a thiyl radical from a thiol monomer that propagates the polymerization by radical addition and chain transfer [155]. The polymer's mechanical and surface properties can simply be tuned by varying the monomer's functional groups and stoichiometry [156, 157]. Since almost any multifunctional thiol will polymerize with any multifunctional ene, Good et al. tailored material characteristics such as ductility and Young's modulus of different thiol-enes by altering the thiol functional groups [156]. Low moduli and high ductility were obtained for polymers that were polymerized with mono- or dithiol monomers, whereas a 10-fold higher modulus was reported for tetrathiol monomers. The stepwise polymerization of thiol-ene is highly efficient and variations

in the thiol:ene ratio will lead to an excess of either of them. Khire et al. used an excess of thiol monomers to polymerize a polymer with surface thiol groups. These are highly desirable anchor molecules in surface modification and allowed covalent attachment of an ultrathin polymer layer to the thiol-ene surface [157].

Already discovered more than a century ago, thiol-ene crosslinking polymers found their way into niche applications such as UV-curable resins, coatings and potential new dental restorative materials [155, 158–160]. It was only recently that thiol-ene polymers experienced a renaissance in microfluidic applications due to their attractive properties and ease in polymerization. First, Harrison et al. described the use of Norland Optical Adhesives (NOA)[1], a commercially available thiol-ene based resin, for the rapid prototyping of microfluidic channels [161]. They exposed a layer of resin between two glass plates through a photomask with collimated UV light and washed away the uncured resin. By employing this simple method, they could fabricate 1 mm deep channels that showed good chemical resistance against common organic solvents such as methanol, toluene and hexane. While Harrison et al. further demonstrated the potential patterning of NOA by polydimethylsiloxane (PDMS) molds, Kim et al. utilized PDMS as peelable molds and demonstrated a high aspect ratio fabrication of hydrophilic NOA micro- and nanostructures [162]. Carlborg et al. demonstrated microfluidic devices that were photopolymerized with excess monomer ratios and demonstrated the successful bonding of excess ene to excess thiol parts [163]. They further investigated the wettability and functionalization properties of different excess monomer ratios, showing once more that the tunable surface functionalities of thiol-ene polymers offer new perspectives, not only for microfluidic applications. Even though some examples for thiol-ene based devices demonstrate the fabrication of thiol-ene based microfluidic chips, not many publications exploit the performance in microfluidic applications. Bartholo et al. showed the generation of hexadecane droplets in 1% sodium dodecyl sulfate in water using NOA based microstickers [164] and James et al. demonstrated the coupling of cavity ring down spectroscopy (CRDS) and the track-

[1] Norland Products Inc., Cranbury, NJ, USA

ing of the oscillating period of the Belousov-Zhabotinsky reaction[2] in a simple microfluidic channel made of NOA [165].

The potential of thiol-ene based microfluidc chips for electrokinetically driven applications has not been investigated and is briefly discussed in parts of this chapter.

Microfluidic chips in this chapter are fabricated by photopolymerizing pentaerythritol tetrakis-(3-mercapto-propionate) (four functional thiol groups) and 1,3,5-triallyl-1,3,5-triazine-2,4,6(1*H*,3*H*,5*H*)-trione (three functional allyl groups). Monomer structures are illustrated in Figure 6.2. Thiol-enes that are polymerized with these monomers are reported to polymerize through a true stoichiometric step-growth reaction, opposed to polymerization with acrylate-monomers that undergo a combined step-growth and homopolymerization, i.e. polymerization of the same functional group. These monomers can successfully be polymerized without the addition of a photoinitiator that might cause autofluorescence and "yellowing" of the chips. Even though, a faster polymerization occurs at $\lambda = 254\,\mathrm{nm}$ the polymerization can still be initiated and propagate at $\lambda = 365\,\mathrm{nm}$ [166].

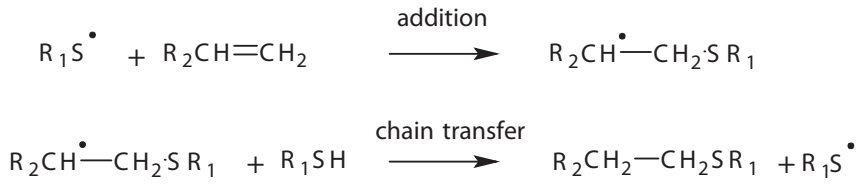

Figure 6.1.: Thiol-ene polymerization: A single thiol reacts with a single ene in a step-growth polymerization mechanism. The addition of a photoinduced thiyl radical forms a carbon radical through the ene functional group. In a second step, the polymerization propagates and forms another thiyl radical.

[2] A nonlinear chemical clock reaction.

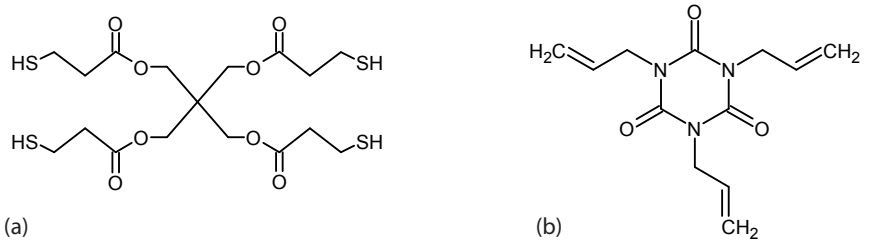

Figure 6.2.: (a) Pentaerythritol tetrakis-(3-mercapto-propionate) (b) 1,3,5-triallyl-1,3,5-triazine-2,4,6(1*H*,3*H*,5*H*)-trione

6.2. Chip design and fabrication

CE was performed with two different chip layouts: In the first layout, a standard cross-injector design (see Figure 6.3 (b)) was used to test the performance and suitability of thiol-ene for microchip CE. The separation channel is 34 mm long, 50 µm wide and 20 µm deep with a rounded channel profile, due to an isotropic etch profile of the Si-master mold[3]. A second design (see Figure 6.3 and Figure 6.8) consists of a 36 mm separation channel and two sidearms to laminate the separation with rhodamine 6G (R6G) functionalized AuNP at the end of the separation column. After lamination, the R6G-AuNPs and potentially separated DTC bands can mix by diffusion in the 19 mm long detection channel. An estimation for the minimum channel length $l \approx 460\,\mu m$ for diffusive mixing was made with the diffusion coefficients for ziram, $D_{Ziram} = 5.12 \times 10^{-10}\,m^2{\cdot}s^{-1}$, and ferbam, $D_{Ferbam} = 4.32 \times 10^{-10}\,m^2{\cdot}s^{-1}$, at an estimated flow velocity of $v_{EOF} = 1\,mm{\cdot}s^{-1}$. The overall detection channel length was 19 mm. The width of the separation and detection channel was 50 µm with a depth of 20 µm and a rectangular cross-sectional profile. Fiber couples were integrated at three different positions for additional UV-absorbance measurements or fluorescence excitation, but were not used during this work.

[3]Si-master was provided by Guisheng Zhuang and Thomas G. Jensen, Technical University of Denmark, Kgs. Lyngby, Denmark

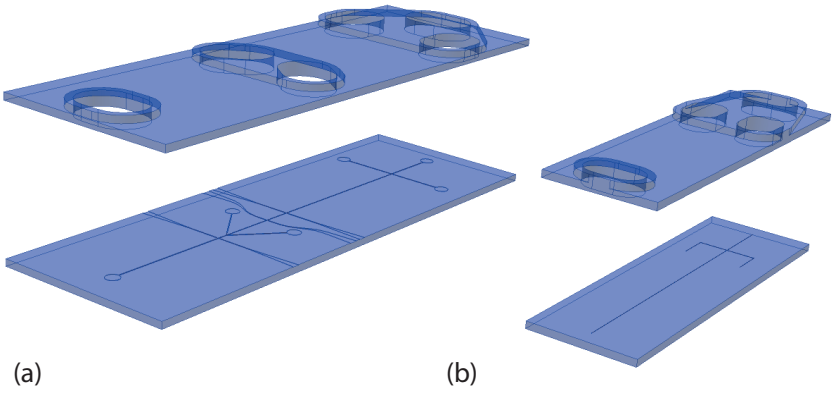

Figure 6.3.: Thiol-ene chip design: Perspective view of top and bottom thiol-ene part of (a) the cross injector design with post-column AuNP lamination for fluorescence detection, and (b) a simple cross-injector design.

Thiol-ene chip fabrication

Thiol-ene chips were fabricated in a photopolymerization-assisted molding process. PDMS molds where used for two reasons: First, thiol-ene does not stick to PDMS and second, PDMS as a flexible material makes demolding of the stiff thiol-ene polymers more feasible. Sylgard 184 elastomere kit (Dow Corning) was used to prepare the PDMS pre-polymer (10:1 ratio), which was then degassed for 30 min under vacuum before it was poured over the molds and cured at 80 °C for 2 h.

Fabrication of PDMS mold

The molds for the channel part were cast from a Si-master that was fabricated by standard clean room processes described in Section 3.3.1 on page 36). Briefly, the silicon wafer was patterned with photoresist. A trench, defining the microfluidic channel, was etched into the silicon wafer (50 µm wide × 20 µm deep) by an anisotropic deep reactive ion etch. The wafer was oxidized and subsequently wet-etched to smoothen the scalloped sidewalls. A no-stick teflon-like coating was applied to prevent PDMS from sticking to the Si-master. From

this master, PDMS slabs were molded that contained a negative (upstanding) copy of the channel structure.

The molds for the top part of the chip were fabricated from a poly(methyl)methacrylate (PMMA) mold, which was stacked and clamped together from several PMMA parts. By stacking the mold instead of milling it from a block of PMMA, a mold with smooth surfaces was obtained, that could replicate smooth surfaced PDMS molds.

Polymerization of thiol-ene chip

Thiol-ene monomers were mixed in different ratios by weighing the appropriate amount of each monomer into a plastic beaker. While stirring, air bubbles are introduced into the mix and the pre-polymer is degassed for approximately 30 min in the dark. Degassing under vacuum, as commonly employed for PDMS prepolymers mixtures, would cause the formation of smaller air bubbles and was thus avoided. The prepolymer was then poured into the PDMS molds, until a convex meniscus formed. The channel structure containing lid (for the bottom part of the chip) was carefully put on top of the mold to avoid the trapping of air at the interface. The closed mold was exposed to UV light (Dymax 5000-EC, Dymax Europe GmbH, Wiesbaden, Germany, intensity $\approx 40\,\mathrm{mW{\cdot}cm^{-2}}$ at 365 nm) for 70 s. Afterwards, the mold was flipped and exposed through the bottom for the same amount of time. Directly after the polymerization, the thiol-ene chip was released from the mold and bonded within 1 h after polymerization. Prior to bonding, the top and bottom part of the chip were heated up in a convective oven for 10 min. Depending on the monomer ratio, the temperature was set to 70 °C (40 % excess thiol) and 90 °C (10 % excess ene), respectively. While heating up the polymer parts softened and the soft parts were brought into conformal contact and bonded by rolling a rubber roll across them. A short 1 min UV exposure right after mating can improve the bonding and was applied for all the chips. Bonded chips were further annealed in a convective oven for 20 min at the above mentioned temperatures.

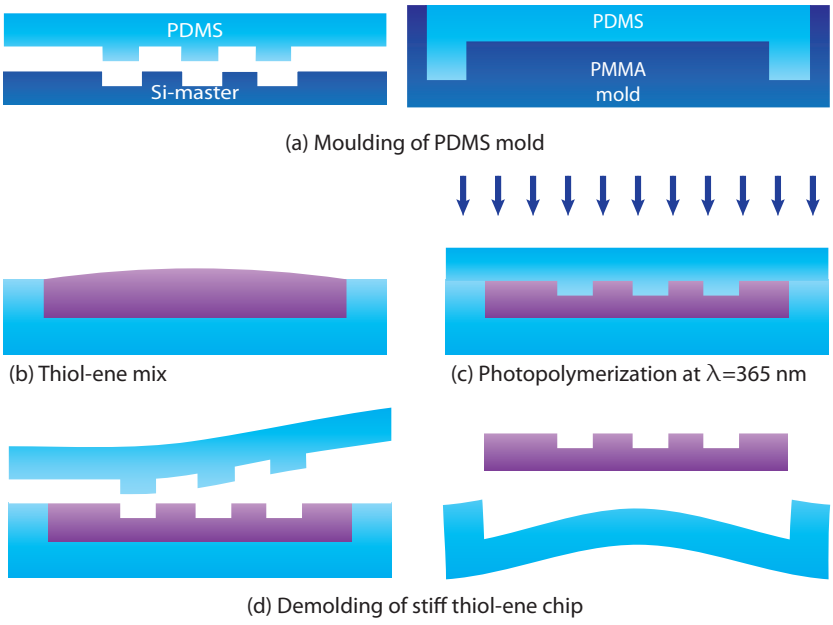

Figure 6.4.: The PDMS mold is cast on a Si-master and onto a PMMA mold. The monomer mix is poured into the mold (b), the open mold is closed with the PDMS slab that contains the channel structures and exposed to UV light (c). The soft and flexible PDMS mold can be peeled off from the stiff chip (d).

6.3. Experimental

Reagents

N,N-Bis(2-hydroxyethyl)glycine (bicine), sodium hydroxide (Scharlau Chemie S.A., Barcelona, Spain), methanol, 2,7-dichlorofluorescein (2,7-DCF), 5-carboxyfluorescein (5-CF), fluorescein sodium salt (FL-Na) and rhodamine 6G (R6G) were of analytical grade and suitable for fluorescence measurements. Fluorescent carboxylate-modified polystyrene latex beads, average size= 0.5 µm, were used for flow observations. A 5 µM bicine buffer stock solution was prepared by diluting the appropriate amount of N,N-bis(2-hydroxyethyl)glycine in 18 MΩ water (Millipore, Billerica, MA, USA) and titrated with 1 M sodium hydroxide to the desired pH. Lower concentrations were prepared by diluting the stock solution with 18 MΩ water. Fluorophore stock solutions, 400 µM 2,7-DCF, 200 µM 5-CF, 100 µM FL-Na were prepared in 2 mM bicine buffer and further diluted as needed. Ziram pesticide standard was prepared by dissolving 2.5 mg zinc bis(dimethyldithiocarbamate) (Pestanal pesticide standard, Sigma Aldrich) in 50 mL methanol. If not otherwise stated, all reagents were of analytical or HPLC grade, obtained from Sigma Aldrich (Saint Louis, MO, USA), and used as received. All solutions were filtered through a 0.2 µm cellulose acetate filer (VVR International, Paris, France) before introducing them to the chip.

Synthesis and modification of AuNP

AuNPs were synthesized with the method already described in Section 5.3 on page 91. The concentration of the AuNP solution was 0.725 nM and the average particle size was 23 nm. AuNP solution was diluted 1:2 (1 part AuNP solution to 1 part 4 mM bicine buffer solution pH: 8.89) and functionalized with 0.26 µM R6G in a R6G:AuNP molar ration of 700.

Experimental setup

The microfluidic chip was placed on an IX71 inverted microscope (Olympus Corporation, Tokyo, Japan) equipped with a fluorescence

lamp (X-Cite 120, EXFO Photonic Solutions Inc., Mississauga, Ontario, Canada) and a filter cube ($\lambda_{ex} = 420 - 480\,\text{nm}$, $\lambda_{em} > 520\,\text{nm}$. A photomultiplier tube (PMT) (H5784-20, Hamamatsu Photonics, Japan) was mounted on the straight part of the microscope's trinocular tube, separated by an additional band pass filter, a pinhole aperture and a tiltable mirror unit, that can deflect the beam at a 90° angle and project the image onto a paper screen. This screen was used to align the microchannel and the pinhole so that only the fluorescence signal from the spot inside the microchannel reached the PMT. For R6G fluorescence measurements, the sample was excited with a laser pointer (www.dx.com, 5 mW, $\lambda = 532\,\text{nm}$) and the emitted light was filtered at $\lambda > 550\,\text{nm}$ through the additional bandpass filter. A schematic drawing of the optical paths, for excitation light and emission path, are depicted in Figure 6.5. The PMT output signal was filtered by a low pass filter at 100 Hz and collected by a Microfluidic Tool Kit (Micralyne, Edmonton, AB, Canada) that also serves as a high voltage supply and was connected to the respective fluid reservoirs via platinum wires. Data collection, potential settings and injection times were controlled with the supplied software. A gated injection scheme was used throughout this work. The current through the separation channel was measured by a picoammeter (485, Keithley Instrument Inc., Cleveland, OH, USA) that was connected to the buffer reservoir. Working potentials were determined by applying a potential between two reservoirs and measuring the current, thus creating an Ohm's-Law plot and calculating the respective potentials using Ohm's law and Kirchhoff's circuit law. Detailed information on calculations can be found in the Ph.D. thesis of Nickolaj J. Petersen [167]. The calculated potentials and the "cut-off" of the sample flow by the buffer during the separation were visually confirmed by FL-Na injections (see also Section 6.3.2). Microchips were first filled with 2 mM bicine buffer by suction and equilibrated for 10 min by applying the respective potentials to establish an electroosmotically driven flow within the channel from the buffer reservoir towards the waste reservoir. Even though, low autofluorescence is reported for thiol-ene materials [164], the fabricated microchips showed autofluorescence at $\lambda_{ex} = 420 - 480\,\text{nm}$, which could significantly be reduced by exposing the detection area through the 20× magnification objective of the

inverted microscope at the excitation wavelength for ca. 20 min. The thereby generated "burned" spot was clearly visible and permanent. Every new chip was therefore treated in this way before the actual measurement.

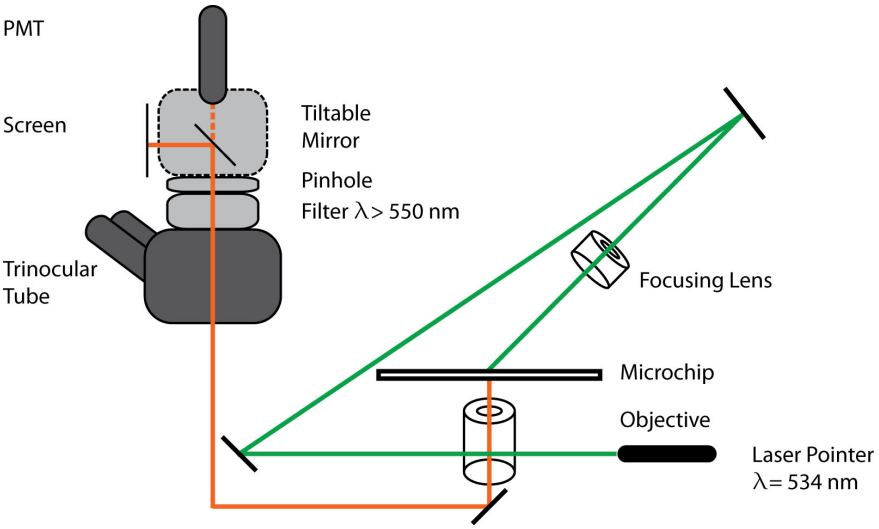

Figure 6.5.: Scheme of the measurement setup for optical detection, with the CE chip on the microscope stage. In this schematic illustration, the optical path for R6G fluorescence measurements is illustrated. The excitation light from a laser pointer (green path) is reflected by two mirrors and focused onto the microfluidic channel. The emitted light (orange path) passes through the trinocular tube of the inverted microscope, a band pass filter and a pinhole aperture to the PMT. Other fluorescence measurements used a fluorescence lamp, where the excitation light is focused through the microscope's objective onto the chip and the emitted light is filtered through the filter cube (not shown) and then follows the same (orange) path.

6.3.1. Fluorophore separation

The simple cross-injector chip design (see Figure 6.3) and three different fluorophores, 2,7-DCF, FL-Na, 5-CF were used to demonstrate the performance of thiol-ene based microfluidic chips for capillary

electrophoresis. These fluorophores are negatively charged when dissolved in basic bicine buffer solution (pH 8.46) with 2,7-DCF (net charge= -1.8) being the least negative, followed by FL-Na (net charge= -1.99) and 5-CF (net charge= -2.99)[4]. The chip had an excess of 40% thiol:ene. To estimate the electroosmotic flow velocity in the channel, the buffer reservoir was filled with 40 µM 2,7-DCF in 2 mM bicine buffer and water was injected from the sample reservoir by a 0.5 s gated injection and a field strength of 247 $\mathrm{V{\cdot}cm^{-1}}$. This indirect fluorescence detection scheme resulted in a high fluorecencent background signal from 2,7-DCF and a negative peak when the neutral water plug passed the detector (see Figure 6.6). Thus the elution time for water can be related to the achieved electroosmotic flow velocity in the system and was determined as 1.01 $\mathrm{mm{\cdot}s^{-1}}$ with an error $< 1\%$ (95% confidence interval with $n = 5$ measurements). While electroosmotic flow in glass capillaries is related to the negatively charged walls, the surface charge of polymer chips is related to adsorbed hydroxide ions onto the polymer surface. Beattie explains this phenomenon by the autolysis of water by the hydrophobic surface of the polymer [168]. The presence of a negative surface charge on thiol-ene chips could further be investigated by evaluating the electroosmotic flow and its dependency on pH changes. Figure 6.7 shows the separation of the three analytes, 2,7-DCF, FL-Na, and 5-CF. Stock solutions of the respective analytes were diluted with 2 mM bicine buffer to a final concentration of 13 µM 2,7-DCF, 10 µM FL-Na and 7 µM 5-CF. The sample was injected for 0.3 s with a field strength of 247 $\mathrm{V{\cdot}cm^{-1}}$ and the fluorescence signal was detected at a distance of 2 cm from the injection. The peaks for 2,7-DCF and 5-CF are baseline-resolved, whereas a further optimization is needed to improve the resolution for FL-Na. Repetitive measurements showed good reproducibility with an error $< 1.5\%$ (95% confidence interval with $n = 3$) for the migration times of the respective elutes.

[4]Net charges calculated with Marvin Sketch(ChemAxon Kft., Budapest, Hungary).

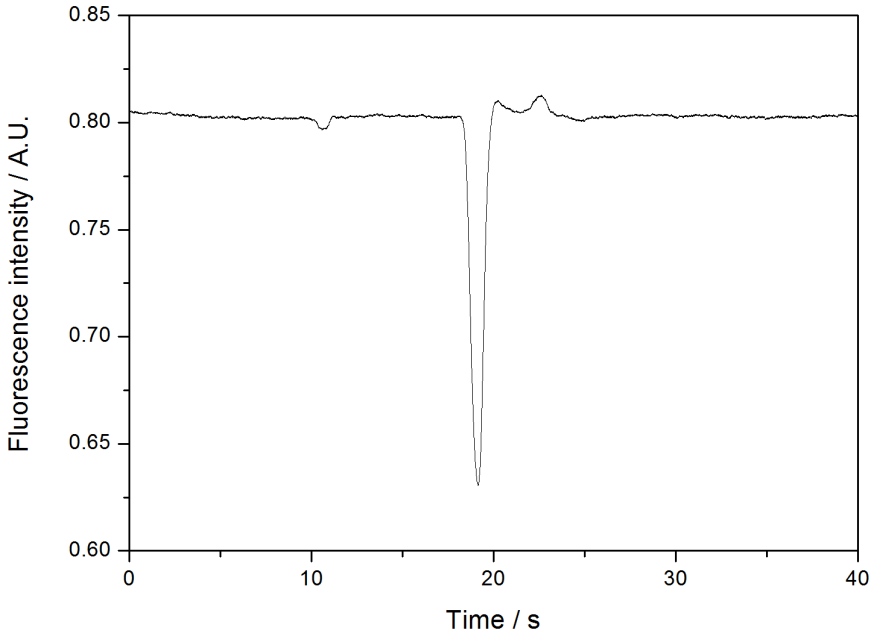

Figure 6.6.: Electroosmotic flow measurement with injection of water. The 2 mM bicine running buffer contains 40 µM 2,7-dichlorofluorescein to visualize the water plug by fluorescence measurements (pH: 8.46). Gated injection scheme with 0.5 s injection time, 247 $V \cdot cm^{-1}$ electric field strength and 1.85 cm distance from injection to detection.

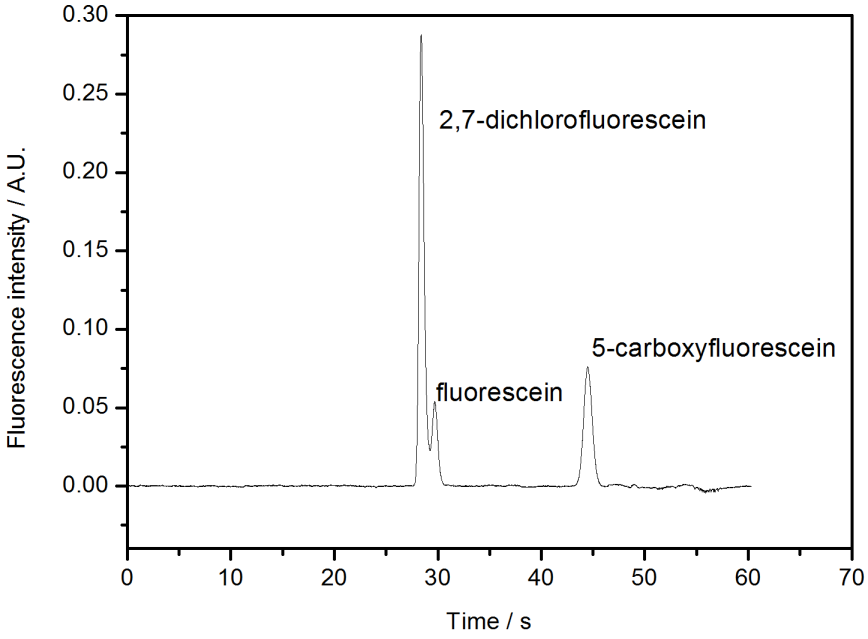

Figure 6.7.: On-chip separation of 13 µM 2,7-dichlorofluorescein, 10 µM fluorescein sodium salt, 7 µM 5-carboxyfluorescein, in 2 mM bicine buffer (pH: 8.46). The gated injection scheme was used with 0.3 s injection time, 247 $V \cdot cm^{-1}$ electric field strength and 2 cm distance from injection to detection. The graph is baseline-corrected to compensate for a drift from the light source and/or photobleaching of the material.

6.3.2. Ziram lamination

For the separation and subsequent lamination with R6G-AuNPs for AuNP mediated detection, a different chip was designed, and the channel layout is depicted in Figure 6.8. The chip was made of thiol-ene with a 10% excess ene:thiol to avoid interaction of R6G-AuNP and terminal thiol groups on the surface. Potentials for sample "cut-off" during separation were calculated using the above described method. The insets in Figure 6.8 show micrographs that were taken during a gated injection of 2,7-DCF and 5-CF. Inset (a) shows the sample plug right after injection and the separation of 20 µM 2,7-DCF (first band) and 10 µM 5-CF (second band) is already visible. Furthermore, the sample stream is "cut-off" by a fraction of the buffer stream at the cross and sample bleeding into the separation channel is avoided. The sample plug passes the AuNP lamination point and flow focusing by the adjacent AuNP flow is visible. The electroosmotic flow velocity was measured by indirect fluorescence detection and was $\upsilon_{EOF} = 0.90\,\mathrm{mm{\cdot}s^{-1}}$ (95% confidence interval for $n = 9$ measurements, field strength $143\,\mathrm{V{\cdot}cm^{-1}}$). Figure 6.9 shows the separation of 4 µM 2,7-DCF and 10 µM FL-Na at a distance 3.7 cm from the injection, i.e. 2 mm after the lamination point. This shows that the lamination is diffusion controlled and does not influence the separation.

The CE microchip was further tested for dithiocarbamate (DTC) pesticide detection. First, ziram samples were injected and the fluorescence signal from released R6G was measured using the fluorescence lamp (excitation with $\lambda_{ex} = 510 - 550\,\mathrm{nm}$) and the filter cube from the microscope setup ($\lambda_{em} > 590\,\mathrm{nm}$), but no signal could be detected for ziram concentrations varying from $125\,\mu\mathrm{g{\cdot}L^{-1}}$, $400\,\mu\mathrm{g{\cdot}L^{-1}}$, and $800\,\mu\mathrm{g{\cdot}L^{-1}}$ in 2 mM bicine buffer (pH: 8.7). No fluorescence signal was detected for 0.5 s and 1.5 s injection times at different detection points, (2, 5 and 10 mm) from the lamination point. A change of the excitation source, from the fluorescence lamp to a laser pointer with $\lambda_{ex} = 532\,\mathrm{nm}$ and another band pass filter ($\lambda_{em} > 550\,\mathrm{nm}$, filter wheel in front of the pinhole in Figure 6.5) to better fit the R6G excitation and emission peaks[5] did not lead to

[5] $\lambda_{ex} = 528\,\mathrm{nm}$, $\lambda_{em} = 551\,\mathrm{nm}$ Source: Sigma Aldrich, Saint Louis, MO, USA

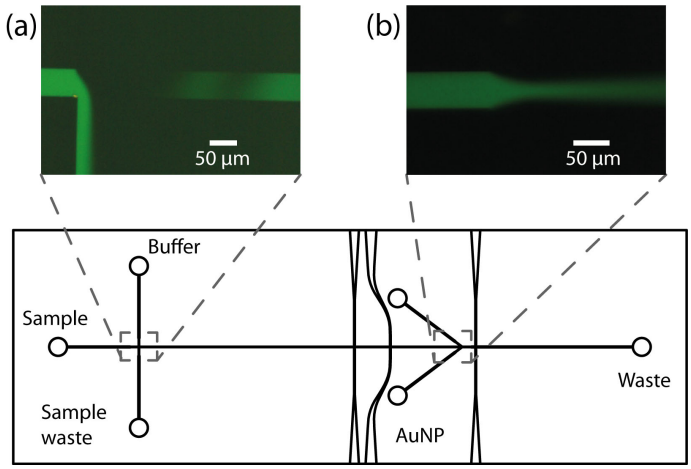

Figure 6.8.: Schematic drawing of the microfluidic chip for DTC separation and detection. (a) Sample "cut-off" during separation mode and bands or 5-CF and 2,7-DCF, (b) R6G-AuNP lamination of the 2,7-DCF plug.

a measurable signal either. To control whether the reaction takes place and can be measured in the microchip device, ziram solutions ranging from 125 to 2000 µg·L^{-1} were mixed-off chip, filled into the buffer reservoir, electrokinetically pumped through the channel and laminated with AuNP at the detection point. The R6G fluorescence intensity was measured 1.5 mm after the lamination point. To allow sufficient time for the interaction between ziram and AuNP, a stop-flow method was applied. After 10 min stabilization, the flow was stopped for 5 s, before the fluorescence signal was measured, and started again for 100 s, stopped for 5 s and so forth. The curve shown in Figure 6.10 illustrates the results. From theses measurements, a ziram-AuNP interaction takes place and a fluorescence signal can be measured, a linear trend can be seen with the limit of linearity at 1200 µg·L^{-1}. The limit of quantification for this measurement is estimated to around 300 µg·L^{-1}, but additional measurements are required in the ziram concentration range from 300 to 1200 µg·L^{-1} to make more qualitative assumptions. While no siphoning effects were

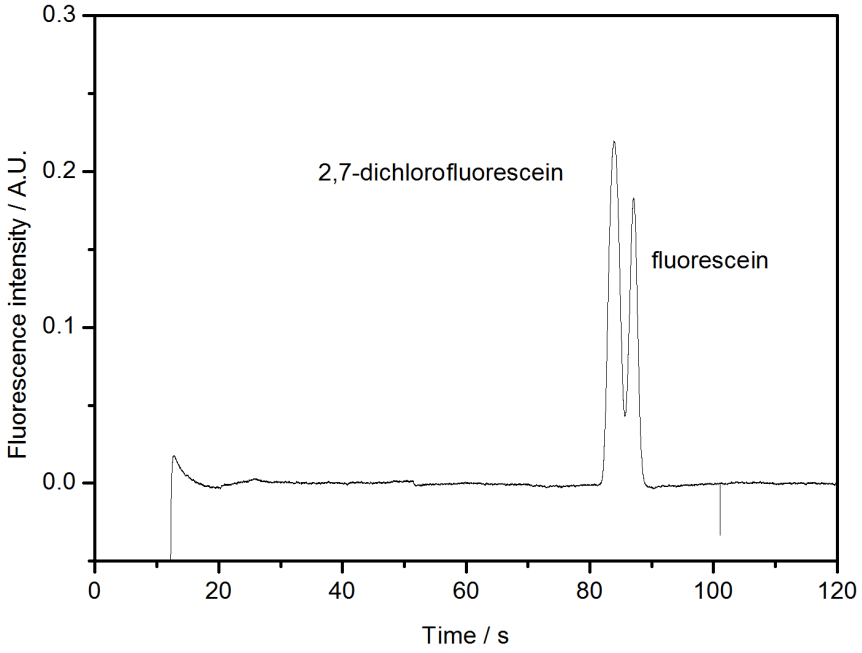

Figure 6.9.: Separation of 4 µM 2,7-dichlorofluorescein and 10 µM fluorescein sodium salt in 2 mM bicine buffer (pH: 8.46) with 0.5 s injection time, detection at 3.7 cm, field strength 143 $V \cdot cm^{-1}$. Detection takes places after the lamination with R6G-AuNP solution. The graph is baseline-corrected to compensate for a drift from the light source and/or photobleaching of the material.

observed in experiments with the simple cross-injector chip (40% excess thiol:ene), back flow from the waste and AuNP reservoirs was seen in experiments with fluorescent beads for the AuNP lamination chip. Backflow in electrokinetically driven flows can have several sources. While siphoning due to different hight levels in liquid reservoirs can be minimized by carefully maintaining the liquid levels, other pressure effects are more difficult to control, such as Laplace pressure that depends on the meniscus shape of the liquid/air interface in the reservoirs [169]. It was found that the 10% excess ene:thiol chips shrink (ca. 1%) during photopolymerization and annealing of the bonded chips. The shrinkage during annealing causes stress-induced bending, which can be counterbalanced by placing a load on top of the chip, while it cools down. Although bent chips could be flattened in this way, minimal height differences due to the internal stress might have caused the observed backflow.

6.4. Conclusions and outlook

Detection of ziram injected samples by R6G-AuNP probe lamination was not successful, but given the short time frame for these experiments (less than three weeks at the end of my Ph.D. project) it could be demonstrated that a principle detection was possible. By employing a stop-flow scheme an increase of fluorescence intensity with increasing ziram concentration was shown. The measurement setup needs further improvement, even though the use of the laser pointer can improve the detection of R6G fluorescence, the setup gets more fragile by using several mirrors and lenses to focus the beam onto the chip. By accidentally moving the microscope stage or the focusing lens, which was easy to happen either by moving the stage, when changing medium or touching the lens with the microscope light source when aligning the microchannel to the pinhole, the beam was out of focus and impossible to refocus onto the same spot. Another filter cube for the inverted microscope with the right excitation and emission filters could significantly simplify the complex system. A second-generation microfluidc chip is probably needed to optimize the mixing after separation and the thiol-ene shrinkage effect on bonded chips needs to be investigated. Tailored thiol-ene

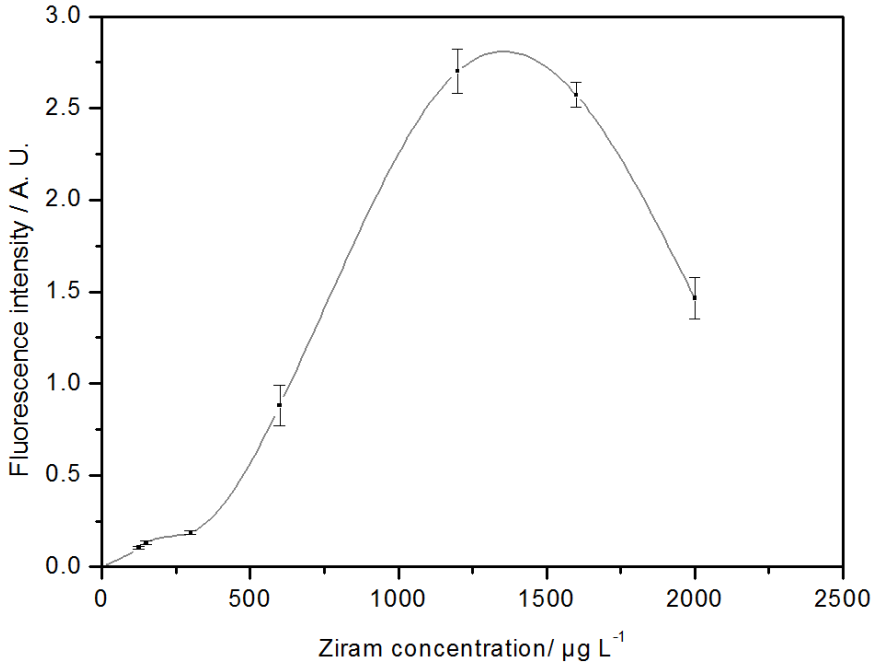

Figure 6.10.: Stop-flow detection after AuNP lamination. The flow was stopped for 5 s before every measurements. Limit of linearity 1200 µg·L^{-1}, due to R6G self-quenching.

polymers offer a unique potential for rapid prototyping of surface-functionalized microfluidic devices, e.g., rapid photochemical patterning of biomolecules inside microfluidic channels [170]. Moreover, they are an interesting alternative to PDMS in soft lithography due to their high chemical resistance and tunable stiffness. The here applied photopolymerization-assisted molding process was very reproducible and PDMS molds could be reused several times. Future chips could be easily fabricated by direct polymerization with a collimated light source through a photomask and thus avoiding the two-step molding process and the fabrication of a Si-master for the PDMS channel mold. Bonded chips did not fail due to collapsed channel walls or leaked due to insufficient bonding as previously reported for cyclic olefin polymer (COP) chips with similar dimensions.

Furthermore, the performance of thiol-ene based microchips for capillary electrophoresis was demonstrated and three fluorophores could successfully and repeatably separated on these chips. Thus, the thiol:ene CE microchips offer a cheap and easy-to-fabricate polymeric alternative, for glass based CE microchips.

7. Conclusions and outlook

The work presented in this thesis summarizes the results of my three year Ph.D. project. It started out as a project to investigate the potential of lab-on-a-chip (LOC) systems for dithiocarbamate analysis. dithiocarbamates (DTCs) are very challenging target analytes for microfluidic approaches, since they are mostly soluble in organic solvents only.

A microfluidic pesticide-screening device that fulfills all the requirements for a cheap, portable and disposable device had to be designed. For this reasons, cyclic olefin polymer (COP) was chosen as a suitable substrate material that would offer a variety of characteristics especially needed for DTC analysis: Chemical inertness made it an ideal substrate candidate for non-aqueous analysis in the first place. Its high optical transmittance and the possibility to integrate gold electrodes on-chip were essential for the implementation of optical and electrochemical detection pathways, well-established detection methods in environmental analysis and LOC based systems. While working with COP, several drawbacks turned out to be major challenges when fabricating thin foil based LOC systems. The bond strength of Zeonor-ZF-14 chips was very weak and could only slightly be improved by UV/ozone (UV/O_3) surface treatments. Long experiments with pressure driven flow often failed due to fluid leakage in weakly bonded areas. Chips made of Topas 5013, another COP substrate material, showed better bonding characteristics than the Zeonor brand.

Microfluidic channels with integrated gold electrodes were fabricated in COP for electrochemical characterizations and detection of different DTC pesticides. Cyclic voltammetry of two different DTCs, showed an electrochemical response for the respective pesticides, but also revealed a fast fouling of the integrated gold electrodes by the sulfur-containing pesticides. The passivated electrodes could not be reactivated by (electro)chemical cleaning protocols and thus were not further investigated for electrochemical DTC analysis. However, a

microfluidic chip fabricated in a similar manner was used in a collaboration project for the electropermeabilization of living bacteria for the extraction of RNA and plasmid DNA (pDNA) with promising results. Although a limiting property in electrochemical analysis with gold electrodes, the high affinity of sulfur to gold was proven extremely useful for gold nanoparticle mediated fluorescence detection of ziram. The change from COP to polydimethylsiloxane (PDMS) as the chip substrate material allowed the fabrication of reliable chips for on-chip mixing of different pesticide concentrations with the gold nanoparticle (AuNP) probe. The obtained calibration curve was linear in the measured range of 45 to 150 $\mu g \cdot L^{-1}$ with a limit of detection as low as 16 $\mu g \cdot L^{-1}$. The demonstrated AuNP based detection scheme is a novel principle that could simplify DTC detection. Conventional acidic hydrolysis of DTCs to CS_2 is circumvented and the developed method, together with a suitable on-chip separation, could provide a future detection method for specific detection of DTC species. It was demonstrated that a simple household digital camera could be used for fluorescent detection of ziram in the low $\mu g \cdot L^{-1}$ range. A smaller camera as it is already used in many consumer devices could, combined with the cheap polymer chip, be sufficient for a portable device for pesticide screening at remote locations. To develop such a device, many unsolved issues will need to be investigated. An on-chip separation of different DTC species will be the next step and to this end thiol-ene was investigated as a polymeric material for microchip capillary electrophoresis.

Thiol-ene chips were so far not used for microchip capillary electrophoresis, but the fabricated chips showed very reproducible results for the separation of 2,7-dichlorofluorescein (2,7-DCF), fluorescein sodium salt (FL-Na) and 5-carboxyfluorescein (5-CF). The AuNP-probe lamination of ziram and subsequent fluorescence detection was demonstrated in channels with a shorter optical path length compared to the design that was used for detection in Chapter 5. COP is without question a remarkable material that is predestined as an alternative substrate material to glass for a wide range of LOC applications. While working with it, I was constantly facing new challenges, either with weakly bonded chips, crazing after Topas embossing, or difficulties in gold lift-off for electrode fabrication. PDMS

and especially thiol-ene have proven, at least during my project, to be more reliable materials. Chips fabricated from thiol-ene could be fabricated in a fast photopolymerization step; electro-osmotic flow in these devices was stable and delamination or fluidic leakage were not observed.

Outlook

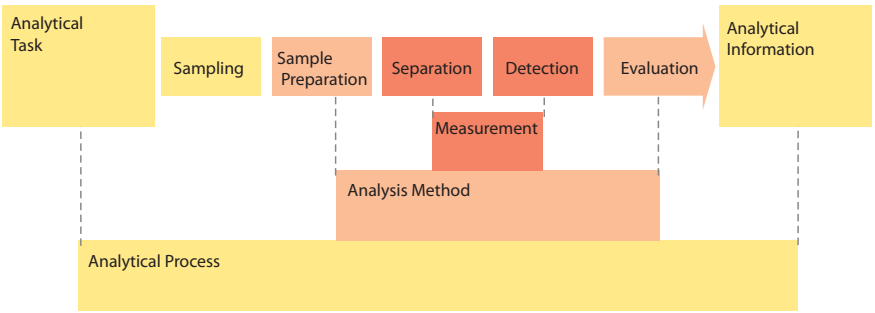

Figure 7.1.: The total analytical process can be divided into several steps: Every analytical process begins with an analytical question or task, several steps are necessary to provide an answer with sufficient analytical information. The analysis method usually comprises a sample preparation step to handle highly complex sample matrices in the following measurement method. The obtained data from sample separation and analyte detection is then evaluated. Figure adapted from Schwedt [171].

The LOC concept was introduced more than 20 years ago and until today there are just a few devices on the market, while the demand for powerful and portable devices is high, not only in environmental monitoring. Measurements with analyte separation and detection are often the first development steps in this process and are essential to obtain analytical information. To provide a portable device that is capable of performing chemical analysis, several further steps and processes need to be integrated into a chip. Figure 7.1 depicts a schematic of such a total analysis process. The analysis process starts always with a specific analytical task, then samples need to be taken and prepared according to the method's relevant protocols to ensure

representative samples before they can be separated and detected in the actual measurement step. The obtained data need to be processed and evaluated until the final analytical information about the target component is available. Such a task-in-answer-out device for DTC monitoring depends on the development of further analytical strategies. First, the present AuNP-mediated detection scheme needs to be combined with an on-chip separation technique for specific DTC analysis. Sample preparation from complex food, groundwater or soil sample matrices is not trivial and on-chip sample preparation strategies might involve several extraction and purification steps that need to be miniaturized. Until today, most research in LOC relevant topics is concentrated on basic fabrication and measurement, to make LOCs a success in environmental analysis the focus needs to expand and span the entire analytical method development, if not the entire analytical process.

References

[1] A. Manz, N. Graber, and H. Widmer. "Miniaturized total chemical analysis systems: A novel concept for chemical sensing." In: *Sensors and Actuators B: Chemical* 1.1-6 (Jan. 1990), pp. 244–248.

[2] C. S. Effenhauser and G. J. M. Bruin. "Review Integrated chip-based capillary electrophoresis." In: *Electrophoresis* 18.12-13 (1997), pp. 2203–2213.

[3] O. Geschke, H. Klank, and P. Tellemann. *Microsystem engineering of lab-on-a-chip devices*. Weinheim: Wiley-VCH, 2004.

[4] S. Mouradian. "Lab-on-a-chip: applications in proteomics." In: *Current Opinion in Chemical Biology* 6.1 (Feb. 2002), pp. 51–56.

[5] P. S. Dittrich and A. Manz. "Lab-on-a-chip: microfluidics in drug discovery." In: *Nature Reviews Drug Discovery* 5.3 (Mar. 2006), pp. 210–218.

[6] C. D. Chin, V. Linder, and S. K. Sia. "Lab-on-a-chip devices for global health: Past studies and future opportunities." In: *Lab on a Chip* 7.1 (2006), pp. 41–57.

[7] L. Chen, A. Manz, and P. J. R. Day. "Total nucleic acid analysis integrated on microfluidic devices." In: *Lab on a Chip* 7.11 (Oct. 2007), pp. 1413–1423.

[8] A. Ríos, M. Zougagh, and M. Avila. "Miniaturization through lab-on-a-chip: Utopia or reality for routine laboratories? A review." In: *Analytica Chimica Acta* 740 (Aug. 2012), pp. 1–11.

[9] H.-F. Li and J.-M. Lin. "Applications of microfluidic systems in environmental analysis." In: *Analytical and Bioanalytical Chemistry* 393.2 (Jan. 2009), pp. 555–567.

[10] A. Martín, D. Vilela, and A. Escarpa. "Food analysis on microchip electrophoresis: An updated review." In: *Electrophoresis* 33.15 (Aug. 2012), pp. 2212–2227.

[11] G. Chen, Y. Lin, and J. Wang. "Monitoring environmental pollutants by microchip capillary electrophoresis with electrochemical detection." In: *Talanta* 68.3 (Jan. 2006), pp. 497–503.

[12] L. Marle and G. M. Greenway. "Microfluidic devices for environmental monitoring." In: *TrAC Trends in Analytical Chemistry* 24.9 (Oct. 2005), pp. 795–802.

[13] S. Solé, A. Merkoçi, and S. Alegret. "Determination of toxic substances based on enzyme inhibition. Part II. Electrochemical biosensors for the determination of pesticides using flow systems." In: *Critical Reviews in Analytical Chemistry* 33.2 (2003), pp. 127–143.

[14] J. S. Van Dyk and B. Pletschke. "Review on the use of enzymes for the detection of organochlorine, organophosphate and carbamate pesticides in the environment." In: *Chemosphere* 82.3 (Jan. 2011), pp. 291–307.

[15] M. D. Luque de Castro and M. C. Herrera. "Enzyme inhibition-based biosensors and biosensing systems: questionable analytical devices." In: *Biosensors and Bioelectronics* 18.2 (2003), pp. 279–294.

[16] X. Llopis et al. "Lab-on-a-chip for ultrasensitive detection of carbofuran by enzymatic inhibition with replacement of enzyme using magnetic beads." In: *Lab on a Chip* 9.2 (2009), pp. 213–218.

[17] O. Szolar. "Environmental and pharmaceutical analysis of dithiocarbamates." In: *Analytica chimica acta* 582.2 (2007), pp. 191–200.

[18] G Vettorazzi et al. "International safety assessment of pesticides: dithiocarbamate pesticides, ETU, and PTU–a review and update." In: *Teratogenesis, carcinogenesis, and mutagenesis* 15.6 (1996), pp. 313–37.

[19] A. Malik and W. Faubel. “Methods of analysis of dithiocarbamate pesticides: a review.” In: *Pesticide Science* 55.10 (1999), pp. 965–970.

[20] A. Wang et al. “Parkinson’s disease risk from ambient exposure to pesticides.” In: *European Journal of Epidemiology* 26.7 (Apr. 2011), pp. 547–555.

[21] G. Crnogorac and W. Schwack. “Residue analysis of dithiocarbamate fungicides.” In: *TrAC Trends in Analytical Chemistry* 28.1 (2009), pp. 40–50.

[22] European Commission. *Commission Regulation (EU) No 600/2010 of 8 July 2010 amending Annex 1 to Regulation (EC) No 396/2005*. 2010.

[23] H. Bjerre Christensen. “Fungicides in food : analytical and food safety aspects.” PhD thesis. Copenhagen: The Royal Veterinary and Agricultural University, 2004.

[24] European Commission. *EU pesticide database*. http://ec.europa.eu/sanco_pesticides/public/index.cfm?event =substance.selection&am p;ch=1, Dec. 31, 2012.

[25] S. Terry, J. Jerman, and J. Angell. “A gas chromatographic air analyzer fabricated on a silicon wafer.” In: *IEEE Transactions on Electron Devices* 26.12 (Dec. 1979), pp. 1880–1886.

[26] E. Bassous, H. H. Taub, and L. Kuhn. “Ink jet printing nozzle arrays etched in silicon.” In: *Applied Physics Letters* 31.2 (1977), p. 135.

[27] H. Bruus. *Theoretical microfluidics*. English. Oxford: Oxford University Press, 2008.

[28] A. Einstein. “Über die von der molekularkinetischen Theorie der Wärme geforderte Bewegung von in ruhenden Flüssigkeiten suspendierten Teilchen.” In: *Annalen der Physik* 322.8 (1905), pp. 549–560.

[29] M. von Smoluchowski. “Zur kinetischen theorie der Brownschen Molekularbewegung und der Suspensionen.” In: *Annalen der Physik* 326.14 (1906), pp. 756–780.

[30] P. Gravesen, J. Branebjerg, and O. S. Jensen. “Microfluidics-a review.” In: *Journal of Micromechanics and Microengineering* 3.4 (1999), p. 168.

[31] T. M. Squires and S. R. Quake. “Microfluidics: Fluid physics at the nanoliter scale.” In: *Reviews of Modern Physics* 77.3 (2005), p. 977.

[32] H. Helmholtz. “Studien über electrische Grenzschichten.” In: *Annalen der Physik* 243.7 (1879), pp. 337–382.

[33] A. J. Bard and L. R. Faulkner. *Electrochemical methods and applications*. English. New York; London: Wiley-Interscience, 2000.

[34] K. Seiler et al. “Electroosmotic Pumping and Valveless Control of Fluid Flow within a Manifold of Capillaries on a Glass Chip.” In: *Analytical Chemistry* 66.20 (1994), pp. 3485–3491.

[35] S. C. Jacobson et al. “Microchip Capillary Electrophoresis with an Integrated Postcolumn Reactor.” In: *Analytical Chemistry* 66.20 (Oct. 1994), pp. 3472–3476.

[36] L. L. Shultz-Lockyear et al. “Effects of injector geometry and sample matrix on injection and sample loading in integrated capillary electrophoresis devices.” In: *Electrophoresis* 20.3 (1999), pp. 529–538.

[37] D. A. Skoog, F. J. Holler, and S. R. Crouch. *Principles of instrumental analysis*. Belmont, CA: Thomson Brooks/Cole, 2007.

[38] J. O. Bockris, M. a. V. Devanathan, and K. Muller. “On the Structure of Charged Interfaces.” In: *Proceedings of the Royal Society of London. Series A. Mathematical and Physical Sciences* 274.1356 (1963), pp. 55–79.

[39] J. Wang. *Analytical Electrochemistry*. 2nd ed. Vol. 3. New York: Vch Verlagsgesellschaft Mbh, 2006.

[40] J. Heinze. “Ultramicroelectrodes in Electrochemistry.” In: *Angewandte Chemie International Edition* 32.9 (1993), pp. 1268–1288.

[41] R. G. Compton and P. R. Unwin. “Channel and tubular electrodes.” In: *Journal of Electroanalytical Chemistry and Interfacial Electrochemistry* 205.1–2 (June 1986), pp. 1–20.

[42] W. LaCourse. *Pulsed electrochemical detection in high performance liquid chromatography*. New York: Wiley, 1997.

[43] H. Becker and L. E. Locascio. “Polymer microfluidic devices.” In: *Talanta* 56.2 (Feb. 2002), pp. 267–87.

[44] D. Snakenborg, H. Klank, and J. P. Kutter. “Microstructure fabrication with a CO_2 laser system.” In: *Journal of Micromechanics and Microengineering* 14.2 (2003), p. 182.

[45] Y. Xia and G. M. Whitesides. “Soft Lithography.” In: *Annual Review of Materials Science* 28.1 (Aug. 1998), pp. 153–184.

[46] J. N. Lee, C. Park, and G. M. Whitesides. “Solvent compatibility of poly(dimethylsiloxane)-based microfluidic devices.” In: *Analytical Chemistry* 75.23 (Dec. 2003), pp. 6544–54.

[47] E. Berthier, E. W. K. Young, and D. Beebe. “Engineers are from PDMS-land, Biologists are from Polystyrenia.” In: *Lab on a Chip* 12.7 (Feb. 2012), pp. 1224–1237.

[48] J. Y. Shin et al. “Chemical structure and physical properties of cyclic olefin copolymers (IUPAC Technical Report).” In: *Pure and Applied Chemistry* 77.5 (2005), pp. 801–814.

[49] M Yamazaki. “Industrialization and application development of cyclo-olefin polymer.” In: *Journal of Molecular Catalysis A: Chemical* 213.1 (Apr. 2004), pp. 81–87.

[50] P. S. Nunes et al. “Cyclic olefin polymers : emerging materials for lab-on-a-chip applications.” In: *Microfluidics and Nanofluidics* 9.2-3 (Apr. 2010), pp. 145–161.

[51] R. R. Lamonte and D. McNally. “Cyclic olefin copolymers.” In: *Advanced Materials & Processes* 159.3 (2001), pp. 33–36.

[52] M. Focke et al. “Lab-on-a-Foil: microfluidics on thin and flexible films.” In: *Lab on a Chip* 10.11 (Mar. 2010), pp. 1365–1386.

[53] H. Becker and U. Heim. “Hot embossing as a method for the fabrication of polymer high aspect ratio structures.” In: *Sensors and Actuators A: Physical* 83.1-3 (May 2000), pp. 130–135.

[54] H. Wang et al. “Low temperature bonding for microfabrication of chemical analysis devices.” In: *Sensors and Actuators B: Chemical* 45.3 (Dec. 1997), pp. 199–207.

[55] S. Bhattacharya et al. “Studies on surface wettability of poly (dimethyl) siloxane (PDMS) and glass under oxygen-plasma treatment and correlation with bond strength.” In: *Journal of Microelectromechanical Systems* 14.3 (2005), pp. 590–597.

[56] H. Klank, J. P. Kutter, and O. Geschke. “CO_2-laser micromachining and back-end processing for rapid production of PMMA-based microfluidic systems.” In: *Lab on a Chip* 2.4 (Nov. 2002), pp. 242–246.

[57] R. Truckenmüller et al. “Bonding of polymer microstructures by UV irradiation and subsequent welding at low temperatures.” In: *Microsystem Technologies* 10.5 (Aug. 2004), pp. 372–374.

[58] J. Kameoka et al. “A polymeric microfluidic chip for CE/MS determination of small molecules.” In: *Analytical Chemistry* 73.9 (2001), pp. 1935–1941.

[59] C. Li et al. “Isoelectric focusing in cyclic olefin copolymer microfluidic channels coated by polyacrylamide using a UV photografting method.” In: *Electrophoresis* 26.9 (May 2005), pp. 1800–1806.

[60] P. Mela et al. “The zeta potential of cyclo-olefin polymer microchannels and its effects on insulative (electrodeless) dielectrophoresis particle trapping devices.” In: *Electrophoresis* 26.9 (May 2005), pp. 1792–1799.

[61] D. A. Mair et al. “Injection molded microfluidic chips featuring integrated interconnects.” In: *Lab on a Chip* 6.10 (Oct. 2006), pp. 1346–54.

[62] B. Pemg and C. Wu. “Microfluidic chip fabrication using hot embossing and thermal bonding of COP.” In: *Polymers for Advanced Technologies* 21.7 (2009), pp. 457–466.

[63] M. Hansen et al. “A nanoimprinted polymer lab-on-a-chip with integrated optics.” In: *Advancements in Polymer Optics Design, Fabrication, and Materials*. San Diego, Aug. 2005, 58720A1–58720A7.

[64] B. Bilenberg et al. “Topas-based lab-on-a-chip microsystems fabricated by thermal nanoimprint lithography.” In: *Journal of Vacuum Science Technology B: Microelectronics and Nanometer Structures* 23.6 (2005), pp. 2944–2949.

[65] O. Gustafsson, K. B. Mogensen, and J. P. Kutter. “Underivatized cyclic olefin copolymer as substrate material and stationary phase for capillary and microchip electrochromatography.” In: *Electrophoresis* 29.15 (Aug. 2008), pp. 3145–52.

[66] C. Fredrickson et al. “Effects of Fabrication Process Parameters on the Properties of Cyclic Olefin Copolymer Microfluidic Devices.” In: *Journal of Microelectromechanical Systems* 15.5 (Oct. 2006), pp. 1060–1068.

[67] A. Bhattacharyya and C. M. Klapperich. “Mechanical and chemical analysis of plasma and ultraviolet-ozone surface treatments for thermal bonding of polymeric microfluidic devices.” In: *Lab on a Chip* 7.7 (2007), pp. 876–882.

[68] C. W. Tsao et al. “Low temperature bonding of PMMA and COC microfluidic substrates using UV/ozone surface treatment.” In: *Lab on a Chip* 7.4 (2007), p. 499.

[69] H. Shinohara, J. Mizuno, and S. Shoji. “Studies on low-temperature direct bonding of VUV , VUV / O_3 and O_2 plasma pretreated cyclo-olefin polymer.” In: *Sensors and Actuators A: Physical* 165.1 (Jan. 2011), pp. 124–131.

[70] S. Roy, C. Yue, and Y. Lam. “Influence of plasma surface treatment on thermal bonding and flow behavior in Cyclic Olefin Copolymer (COC) based microfluidic devices.” In: *Vacuum* 85.12 (June 2011), pp. 1102–1104.

[71] T. I. Wallow et al. “Low-distortion, high-strength bonding of thermoplastic microfluidic devices employing case-II diffusion-mediated permeant activation.” In: *Lab on a Chip* 7.12 (Dec. 2007), pp. 1825–1831.

[72] D. A. Mair et al. “Room-temperature bonding for plastic high-pressure microfluidic chips.” In: *Analytical Chemistry* 79.13 (July 2007), pp. 5097–102.

[73] I. Ogilvie and V. Sieben. “Reduction of surface roughness for optical quality microfluidic devices in PMMA and COC.” In: *Journal of Micromechanics and Microengineering* 20.6 (June 2010), p. 065016.

[74] J. Han et al. “UV adhesive bonding techniques at room temperature for plastic lab-on-a-chip.” In: *7th international Conference on Miniaturized Chemical And Biochemical Analysis Systems*. 2003, pp. 1113 –1116.

[75] J. Raj et al. “Surface immobilisation of antibody on cyclic olefin copolymer for sandwich immunoassay.” In: *Biosensors and Bioelectronics* 24.8 (Apr. 2009), pp. 2654–8.

[76] J. Mizuno et al. “Cyclo-Olefin polymer direct bonding using low temperature plasma activation bonding.” In: *The 13th International Conference on Solid-State Sensors, Actuators and Microsystems, 2005. Digest of Technical Papers. Transducers ’05*. Ieee, 2005, pp. 1346–1349.

[77] S.-J. Hwang et al. “Surface modification of cyclic olefin copolymer substrate by oxygen plasma treatment.” In: *Surface and Coatings Technology* 202.15 (2008), pp. 3669–3674.

[78] C. Tsao and D. DeVoe. “Bonding of thermoplastic polymer microfluidics.” In: *Microfluidics and Nanofluidics* 6.1 (Nov. 2009), pp. 1–16.

[79] S. Miserere et al. “Fabrication of thermoplastics chips through lamination based techniques.” In: *Lab on a Chip* 12.10 (Mar. 2012), pp. 1849–1856.

[80] K. W. Ro, J. Liu, and D. R. Knapp. "Plastic microchip liquid chromatography-matrix-assisted laser desorption/ionization mass spectrometry using monolithic columns." In: *Journal of Chromatography A* 1111.1 (Apr. 2006), pp. 40–47.

[81] J Liu et al. "Monolithic column plastic microfluidic device for peptide analysis using electrospray from a channel opening on the edge of the device." In: *International Journal of Mass Spectrometry* 259.1-3 (Jan. 2007), pp. 65–72.

[82] X. Illa et al. "A cyclo olefin polymer microfluidic chip with integrated gold microelectrodes for aqueous and non-aqueous electrochemistry." In: *Lab on a Chip* 10.10 (May 2010), pp. 1254–1261.

[83] A. F. M. Barton. *CRC Handbook of Solubility Parameters and Other Cohesion Parameters, Second Edition*. 2nd ed. CRC Press, Oct. 1991, p. 768.

[84] D. Paul et al. "Lamination-based rapid prototyping of microfluidic devices using flexible thermoplastic substrates." In: *Electrophoresis* 28.7 (Apr. 2007), pp. 1115–1122.

[85] P. P. Gillis and J. J. Gilman. "Double Cantilever Cleavage Mode of Crack Propagation." In: *Journal of Applied Physics* 35.3 (Mar. 1964), pp. 647–658.

[86] W. P. Maszara et al. "Bonding of silicon wafers for silicon-insulator." In: *Journal of Applied Physics* 64.10 (Nov. 1988), pp. 4943–4950.

[87] W. Goerlitz and A.-M. Schauwienold. "Polymer blend for producing films with a reduced number of deffects." U.S. pat. WO2006042681. 2006.

[88] B.-L. Johansson et al. "Characterization of air plasma-treated polymer surfaces by ESCA and contact angle measurements for optimization of surface stability and cell growth." In: *Journal of Applied Polymer Science* 86.10 (2002), pp. 2618–2625.

[89] D. A. Mair et al. "Room-temperature bonding for plastic high-pressure microfluidic chips." In: *Analytical chemistry* 79.13 (July 2007), pp. 5097–102.

[90] O. H. J. Szolar. “Environmental and pharmaceutical analysis of dithiocarbamates.” In: *Analytica Chimica Acta* 582 (2007), pp. 191–200.

[91] L. Mathew et al. “Differential pulse anodic stripping voltammetric determination of ziram (a dithiocarbamate fungicide).” In: *Talanta* 43.1 (1996), pp. 73–76.

[92] M. Shan Lin et al. “Trace measurement of dithiocarbamate based pesticide by adsorptive stripping voltammetry.” In: *Analytica Chimica Acta* 388.1-2 (May 1999), pp. 111–117.

[93] P. Qiu and Y. N. Ni. “Determination of ziram in vegetable samples by square wave voltammetry.” In: *Chinese Chemical Letters* 19.11 (Nov. 2008), pp. 1337–1340.

[94] D. Sharma et al. “A pulse polarographic method for the analysis of zinc dithiocarbamates.” In: *Indian Journal of Chemistry* 46.7 (July 2007), pp. 1121–1124.

[95] M. d. P. da Silva, J. R. Procopio, and L. Hernández. “Electrochemical detection in the determination of several dithiocarbamates by reverse-phase liquid chromatography.” In: *Journal of Liquid Chromatography & Related Technologies* 22.3 (1999), pp. 463–475.

[96] M Hernández-Olmos, L Agu, and P Ya. “Analytical voltammetry in low-permitivity organic solvents using disk and cylindrical microelectrodes. Determination of thiram in ethyl acetate.” In: *Electrochimica Acta* 46.2-3 (Nov. 2000), pp. 289–296.

[97] M. T. Sevilla et al. “Voltammetric Determination of Thiram following Adsorptive Accumulation on a Rotating Gold Disk Electrode.” In: *Electroanalysis* 2 (1990), pp. 475–479.

[98] A Ngoviwatchai and D. Johnson. “Pulsed amperometric detection of sulfur-containing pesticides in reversed-phase liquid chromatography.” In: *Analytica Chimica Acta* 215 (1988), pp. 1–12.

[99] R. S. Martin et al. “Dual-Electrode Electrochemical Detection for Poly(dimethylsiloxane)-Fabricated Capillary Electrophoresis Microchips.” In: *Analytical Chemistry* 72.14 (July 2000), pp. 3196–3202.

[100] C. D. García and C. S. S. Henry. "Comparison of Pulsed Electrochemical Detection Modes Coupled with Microchip Capillary Electrophoresis." In: *Electroanalysis* 17.3 (Feb. 2005), pp. 223–230.

[101] C. D. García and C. Henry. "Coupling Capillary Electrophoresis and Pulsed Electrochemical Detection." In: *Electroanalysis* 17.13 (2005), pp. 1125–1131.

[102] D.-S. Lee et al. "Wafer-Scale Fabrication of Polymer-Based Microdevices via Injection Molding and Photolithographic Micropatterning Protocols." In: *Analytical Chemistry* 77.16 (Aug. 2005), pp. 5414–5420.

[103] Z. Zou et al. "Functionalized nano interdigitated electrodes arrays on polymer with integrated microfluidics for direct bioaffinity sensing using impedimetric measurement." In: *Sensors and Actuators A: Physical* 136.2 (May 2007), pp. 518–526.

[104] J. Shim, M. Rust, and C. Ahn. "Interdigitated Array Electrodes with Nano Gaps Using Optical Lithography and Controlled Undercut Method." In: *Nanotechnology 2008. NANO '08. 8th IEEE Conference on Nanotechnology.* Aug. 2008, pp. 851–854.

[105] H. Shinohara et al. "Polymer microchip integrated with nanoelectrospray tip for electrophoresis-mass spectrometry." In: *Sensors and Actuators B: Chemical* 132.2 (June 2008), pp. 368–373.

[106] L. M. Fischer et al. "Gold cleaning methods for electrochemical detection applications." In: *Microelectronic Engineering* 86.4–6 (June 2009), pp. 1282–1285.

[107] A. Ngoviwatchai and D. C. Johnson. "A study of the anodic oxidation of thiophosphate at a gold electrode in 0.10 M sodium hydroxide by double-potential-step chronocoulometry in a thin-layer cell." In: *Electroanalysis* 1.2 (Mar. 1989), pp. 125–131.

[108] P. J. Vandeberg, J. L. Kowagoe, and D. C. Johnson. “Pulsed amperometric detection of sulfur compounds: thiourea at gold electrodes.” In: *Analytica Chimica Acta* 260.1 (May 1992), pp. 1–11.

[109] W. LaCourse and G. Owens. “Pulsed electrochemical detection of thiocompounds following microchromatographic separations.” In: *Analytica Chimica Acta* 307.2-3 (May 1995), pp. 301–319.

[110] G. Owens and W. LaCourse. “Pulsed electrochemical detection of thiols and disulfides following capillary electrophoresis.” In: *Journal of Chromatography B: Biomedical Sciences and Applications* 695.1 (1997), pp. 15–25.

[111] S. J. Modi, W. R. LaCourse, and R. E. Shansky. “Determination of thio-based additives for biopharmaceuticals by pulsed electrochemical detection following HPLC.” In: *Journal of Pharmaceutical and Biomedical Analysis* 37.1 (Feb. 2005), pp. 19–25.

[112] W. R. LaCourse and S. Modi. “Microelectrode Applications of Pulsed Electrochemical Detection.” In: *Electroanalysis* 17.13 (2005), pp. 1141–1152.

[113] K. Montzka Wassarman, A. Zhang, and G. Storz. “Small RNAs in Escherichia coli.” In: *Trends in Microbiology* 7.1 (Jan. 1999), pp. 37–45.

[114] R. Martins, J. A. Queiroz, and F. Sousa. “A new affinity approach to isolate Escherichia coli 6S RNA with histidine-chromatography.” In: *Journal of Molecular Recognition* 23.6 (2010), pp. 519–524.

[115] F. Sousa, D. M. Prazeres, and J. a. A. Queiroz. “Affinity chromatography approaches to overcome the challenges of purifying plasmid DNA.” In: *Trends in Biotechnology* 26.9 (Sept. 2008), pp. 518–525.

[116] D. E. Taylor and E. C. Brose. “Modified Birnboim-Doly method for rapid detection of plasmid copy number.” In: *Nucleic Acids Research* 16.18 (Sept. 1988), pp. 9056–9056.

[117] P. Chomczynski and N. Sacchi. "The single-step method of RNA isolation by acid guanidinium thiocyanate-phenol-chloroform extraction: twenty-something years on." In: *Nature Protocols* 1.2 (2006), pp. 581–585.

[118] H. J. Lee et al. "Electrochemical cell lysis device for DNA extraction." In: *Lab on a Chip* 10.5 (Mar. 2010), pp. 626–633.

[119] P. Vulto et al. "A microfluidic approach for high efficiency extraction of low molecular weight RNA." In: *Lab on a Chip* 10.5 (Mar. 2010), pp. 610–616.

[120] E. Neumann, S. Kakorin, and K. Toensing. "Principles of Membrane Electroporation and Transport of Macromolecules." In: *Methods in Molecular Medcine*. Ed. by M. J. Jaroszeski, R. Heller, and R. Gilbert. Methods in Molecular Medicine. Humana Press, Jan. 2000, pp. 1–35.

[121] M. B. Fox et al. "Electroporation of cells in microfluidic devices: a review." In: *Analytical and Bioanalytical Chemistry* 385.3 (Mar. 2006), pp. 474–485.

[122] R. G. Nuzzo and D. L. Allara. "Adsorption of bifunctional organic disulfides on gold surfaces." In: *Journal of the American Chemical Society* 105.13 (June 1983), pp. 4481–4483.

[123] L. Strong and G. M. Whitesides. "Structures of self-assembled monolayer films of organosulfur compounds adsorbed on gold single crystals: electron diffraction studies." In: *Langmuir* 4.3 (May 1988), pp. 546–558.

[124] A. Ulman. "Formation and structure of self-assembled monolayers." In: *Chemical Reviews* 96.4 (1996), p. 1533.

[125] J. C. Love et al. "Self-assembled monolayers of thiolates on metals as a form of nanotechnology." In: *Chemical Reviews* 105.4 (2005), pp. 1103–1170.

[126] Y. Zhao et al. "Dithiocarbamate assembly on gold." In: *Journal of the American Chemical Society* 127.20 (2005), pp. 7328–7329.

[127] P. Morf et al. “Dithiocarbamates:A Functional and Versatile Linkers for the Formation of Self-Assembled Monolayers.” In: *Langmuir* 22.2 (Jan. 2006), pp. 658–663.

[128] M. S. Vickers et al. “Dithiocarbamate ligand stabilised gold nanoparticles.” In: *Journal of Materials Chemistry* 16.2 (2006), p. 209.

[129] M. Park et al. “Chemically Directed Immobilization of Nanoparticles onto Gold Substrates for Orthogonal Assembly Using Dithiocarbamate Bond Formation.” In: *ACS Applied Materials & Interfaces* 2.3 (Mar. 2010), pp. 795–799.

[130] Y. Kim, R. C. Johnson, and J. T. Hupp. “Gold nanoparticle-based sensing of “spectroscopically silent” heavy metal ions.” In: *Nano Letters* 1.4 (2001), pp. 165–167.

[131] S. Kühn et al. “Enhancement of single-molecule fluorescence using a gold nanoparticle as an optical nanoantenna.” In: *Physical Review Letters* 97.1 (2006), pp. 17402–1–4.

[132] G.-Y. Kim et al. “Preparation of a highly sensitive enzyme electrode using gold nanoparticles for measurement of pesticides at the ppt level.” In: *Journal of Environmental Monitoring* 10.5 (2008), pp. 632–637.

[133] C. C. Huang and H. T. Chang. “Selective gold-nanoparticle-based “turn-on” fluorescent sensors for detection of mercury (II) in aqueous solution.” In: *Analytical Chemistry* 78.24 (2006), pp. 8332–8338.

[134] G. K. Darbha, A. Ray, and P. C. Ray. “Gold Nanoparticle-Based Miniaturized Nanomaterial Surface Energy Transfer Probe for Rapid and Ultrasensitive Detection of Mercury in Soil, Water, and Fish.” In: *ACS Nano* 1.3 (Oct. 2007), pp. 208–214.

[135] H. Wang et al. “Gold Nanoparticle-Based Colorimetric and “Turn-O” Fluorescent Probe for Mercury(II) Ions in Aqueous Solution.” In: *Analytical Chemistry* 80.23 (Dec. 2008), pp. 9021–9028.

[136] J. Xie, Y. Zheng, and J. Y. Ying. "Highly selective and ultrasensitive detection of Hg^{2+} based on fluorescence quenching of Au nanoclusters by Hg^{2+}-Au^{+}interactions." In: *Chemical Communications* 46.6 (2010), pp. 961–963.

[137] T. Huang and R. W. Murray. "Quenching of $[Ru(bpy)_3]^{2+}$ Fluorescence by Binding to Au Nanoparticles." In: *Langmuir* 18.18 (Sept. 2002), pp. 7077–7081.

[138] E Dulkeith et al. "Fluorescence quenching of dye molecules near gold nanoparticles: radiative and nonradiative effects." In: *Physical review letters* 89.20 (Nov. 2002), p. 203002.

[139] C. Fan, S. Wang, and J. Hong. "Beyond superquenching: hyperefficient energy transfer from conjugated polymers to gold nanoparticles." In: *Proceedings of the National Academy of Sciences of the United States of America* 100.11 (May 2003), pp. 6297–6301.

[140] T. J. Lin, K. T. Huang, and C. Y. Liu. "Determination of organophosphorous pesticides by a novel biosensor based on localized surface plasmon resonance." In: *Biosensors and Bioelectronics* 22.4 (2006), pp. 513–518.

[141] A. Virel, L. Saa, and V. Pavlov. "Modulated Growth of Nanoparticles. Application for Sensing Nerve Gases." In: *Analytical Chemistry* 81.1 (Jan. 2009), pp. 268–272.

[142] H. Li et al. "Visual detection of organophosphorus pesticides represented by mathamidophos using Au nanoparticles as colorimetric probe." In: *Talanta* 87 (Dec. 2011), pp. 93–99.

[143] J. Sun et al. "A simple, label-free AuNPs-based colorimetric ultrasensitive detection of nerve agents and highly toxic organophosphate pesticide." In: *Biosensors and Bioelectronics* 28.1 (Oct. 2011), pp. 152–157.

[144] D. Liu et al. "A Highly Sensitive, Dual-Readout Assay Based on Gold Nanoparticles for Organophosphorus and Carbamate Pesticides." In: *Analytical Chemistry* 84.9 (2012), pp. 4185–4191.

[145] T. R. Fukuto. "Mechanism of action of organophosphorus and carbamate insecticides." In: *Environmental Health Perspectives* 87 (July 1990), p. 245.

[146] J. Chen et al. "A functionalized gold nanoparticles and Rhodamine 6G based fluorescent sensor for high sensitive and selective detection of mercury(II) in environmental water samples." In: *Analytica Chimica Acta* 599.1 (Sept. 2007), pp. 134–142.

[147] G. Frens. "Controlled Nucleation for the Regulation of the Particle Size in Monodisperse Gold Suspensions." In: *Nature* 241.105 (Jan. 1973), pp. 20–22.

[148] J. Turkevich, P. C. Stevenson, and J. Hillier. "A study of the nucleation and growth processes in the synthesis of colloidal gold." In: *Discussions of the Faraday Society* 11 (1951), p. 55.

[149] K. C. Grabar et al. "Preparation and Characterization of Au Colloid Monolayers." In: *Analytical Chemistry* 67.4 (1995), pp. 735–743.

[150] W. Haiss et al. "Determination of Size and Concentration of Gold Nanoparticles from UV-Vis Spectra." In: *Analytical Chemistry* 79.11 (June 2007), pp. 4215–4221.

[151] J Lafleur et al. "Gold nanoparticle-based optical microfluidic sensors for analysis of environmental pollutants." In: *Lab on a Chip* 12.22 (June 2012), pp. 4651–4656.

[152] Y. Xiang and A. Tong. "A New Rhodamine-Based Chemosensor Exhibiting Selective FeIII-Amplified Fluorescence." In: *Organic Letters* 8.8 (Apr. 2006), pp. 1549–1552.

[153] J. Mao, Q. He, and W. Liu. "An rhodamine-based fluorescence probe for iron(III) ion determination in aqueous solution." In: *Talanta* 80.5 (Mar. 2010), pp. 2093–2098.

[154] C. R. Morgan, F. Magnotta, and A. D. Ketley. "Thiol/ene photocurable polymers." In: *Journal of Polymer Science: Polymer Chemistry Edition* 15.3 (1977), pp. 627–645.

[155] N. B. Cramer and C. N. Bowman. "Kinetics of thiol-ene and thiol-acrylate photopolymerizations with real-time fourier transform infrared." In: *Journal of Polymer Science Part A: Polymer Chemistry* 39.19 (2001), pp. 3311–3319.

[156] B. T. Good et al. "Tailorable low modulus, reversibly deformable elastomeric thiol-ene materials for microfluidic applications." In: *Sensors and Actuators B: Chemical* 120.2 (Jan. 2007), pp. 473–480.

[157] V. S. Khire et al. "Formation and Surface Modification of Nanopatterned Thiol-ene Substrates using Step and Flash Imprint Lithography." In: *Advanced Materials* 20.17 (2008), pp. 3308–3313.

[158] C. E. Hoyle, T. Y. Lee, and T. Roper. "Thiol-enes: Chemistry of the past with promise for the future." In: *Journal of Polymer Science Part A: Polymer Chemistry* 42.21 (2004), pp. 5301–5338.

[159] H. Lu et al. "Investigations of step-growth thiol-ene polymerizations for novel dental restoratives." In: *Dental Materials* 21.12 (2005), pp. 1129–1136.

[160] C. E. Hoyle and C. N. Bowman. "Thiol-Ene Click Chemistry." In: *Angewandte Chemie International Edition* 49.9 (2010), pp. 1540–1573.

[161] C. Harrison et al. "A rapid prototyping technique for the fabrication of solvent-resistant structures." In: *Journal of Micromechanics and Microengineering* 14.1 (Jan. 2004), pp. 153–158.

[162] Y. S. Kim et al. "Nanofeature-Patterned Polymer Mold Fabrication toward Precisely Defined Nanostructure Replication." In: *Chemistry of Materials* 17.23 (Nov. 2005), pp. 5867–5870.

[163] C. F. Carlborg et al. "Beyond PDMS: off-stoichiometry thiol-ene (OSTE) based soft lithography for rapid prototyping of microfluidic devices." In: *Lab on a Chip* 11.18 (2011), pp. 3136–3147.

[164] D. Bartolo et al. "Microfluidic stickers." In: *Lab on a Chip* 8.2 (2007), pp. 274–279.

[165] D. James et al. “High-sensitivity online detection for microfluidics via cavity ringdown spectroscopy.” In: *RSC Advances* 2.12 (May 2012), pp. 5376–5384.

[166] N. B. Cramer, J. P. Scott, and C. N. Bowman. “Photopolymerizations of Thiol-Ene Polymers without Photoinitiators.” In: *Macromolecules* 35.14 (July 2002), pp. 5361–5365.

[167] N. J. Petersen. “Electrophoretic seperations on microchips: performance and possibilities.” PhD thesis. Kgs. Lyngby: Mikroelektronik Centret, Technical University of Denmark, 2004.

[168] J. K. Beattie. “The intrinsic charge on hydrophobic microfluidic substrates.” In: *Lab on a Chip* 6.11 (Oct. 2006), pp. 1409–1411.

[169] H. J. Crabtree et al. “Microchip Injection and Separation Anomalies Due to Pressure Effects.” In: *Analytical Chemistry* 73.17 (Sept. 2001), pp. 4079–4086.

[170] J. Lafleur et al. “Rapid photochemical surface patterning of proteins in thiol-ene based microfluidic devices.” In: *Analyst* (Nov. 2012).

[171] G. Schwedt. *Taschenatlas der Analytik*. Stuttgart [u.a.]: Thieme, 1992.

A. List of publications

Peer-reviewed paper

- J.P. Lafleur, S. Senkbeil, T.G. Jensen and J.P. Kutter, "Gold nanoparticle-based optical microfluidic sensors for analysis of environmental pollutants". Lab on a Chip, Volume 12, Issue 22, pp. 4651–4656, 2012.

Talks at conferences

- S. Senkbeil, J. Smedsgaard, A. Romano-Rodríguez and J.P. Kutter, "Tackling challenges in food safety with lab-on-chip technologies", 21. Doktorandenseminar des AK Separation Science, Hohenroda, Germany, January 10$^{\text{th}}$, 2011.

- S. Senkbeil, J. Smedsgaard, A. Romano-Rodríguez and J.P. Kutter, "Tackling challenges in food safety with lab-on-chip technologies", LabAutomation 2011, Palm Springs, California, USA, January 31$^{\text{st}}$, 2011.

Posters at conferences

Presenting author is indicated with an asterisk.

- S. Senkbeil*, J. Smedsgaard and J.P. Kutter, "Optical and electrochemical detection of pesticides using novel COP micro chips", 27$^{\text{th}}$ International Symposium on MicroScale Bioseparations and Analyses (MSB 2012), Geneva, Switzerland, February 12-15, 2012.

- S. Senkbeil, J.P. Lafleur, T.G. Jensen and J.P. Kutter*, "Gold nanoparticle-based fluorescent sensor for the analysis of dithio-

carbamate pesticides in water", International Conference of Miniaturized Systems for Chemistry and Life Sciences (MicroTAS 2012), Okinawa, Japan, October 28 – November 1, 2012.

B. Technical Drawings

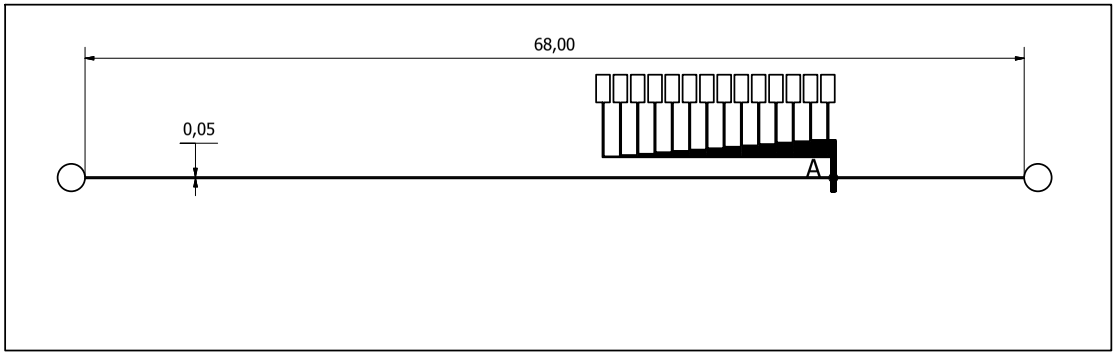

A (150:1)

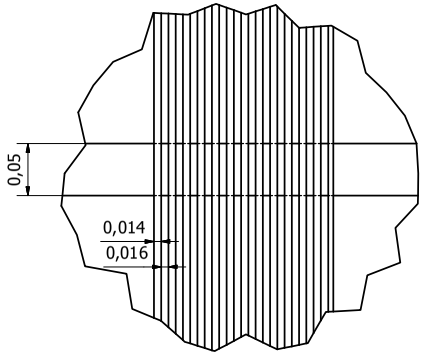

Designed by	Checked by	Approved by	Date	Date	
sise				03-01-2013	
		Zeonor Chip with integrated gold electrodes			
		ChipCOP		Edition	Sheet 1 / 1

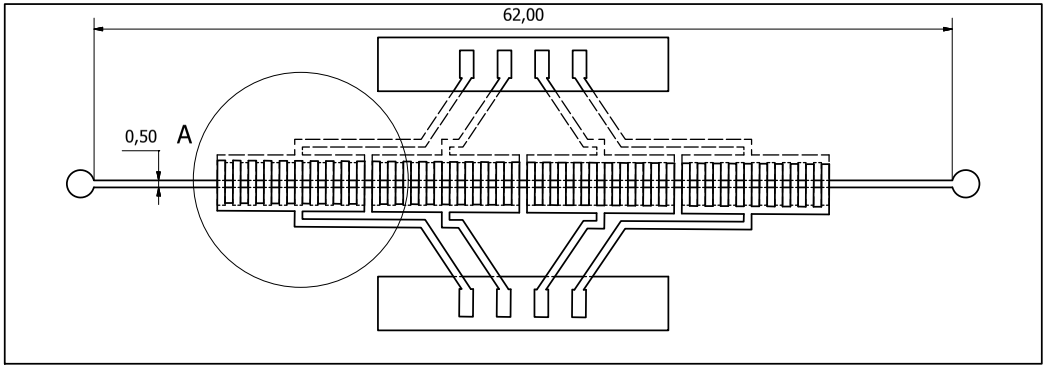

A (8 : 1)

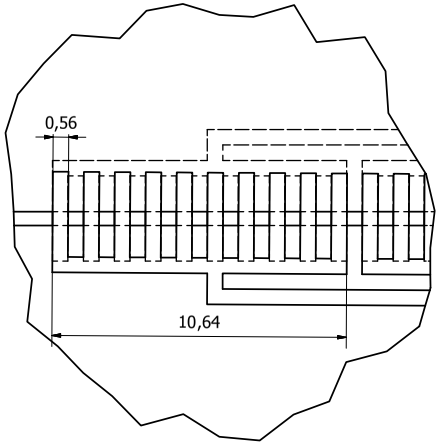

Designed by	Checked by	Approved by	Date	Date	
sise					
		Topas Chip with facing gold electrodes			
		Topas Chip		Edition	Sheet 1 / 1

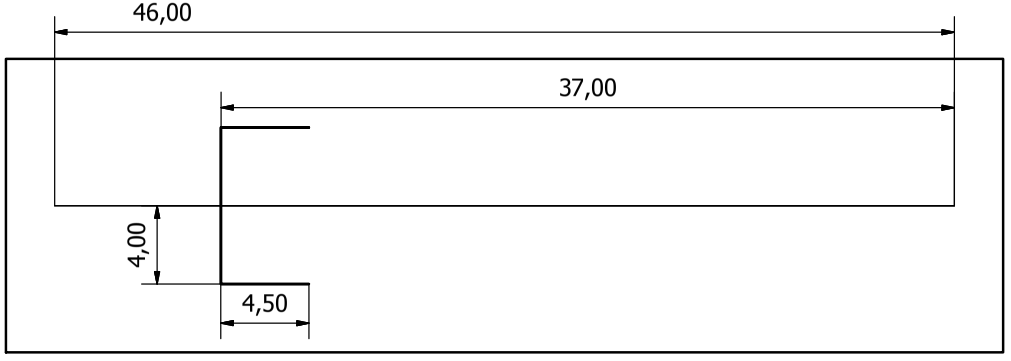

Designed by	Checked by	Approved by	Date		Date	
sise						
				Thiol-ene CE Microchip	Edition	Sheet 1 / 1

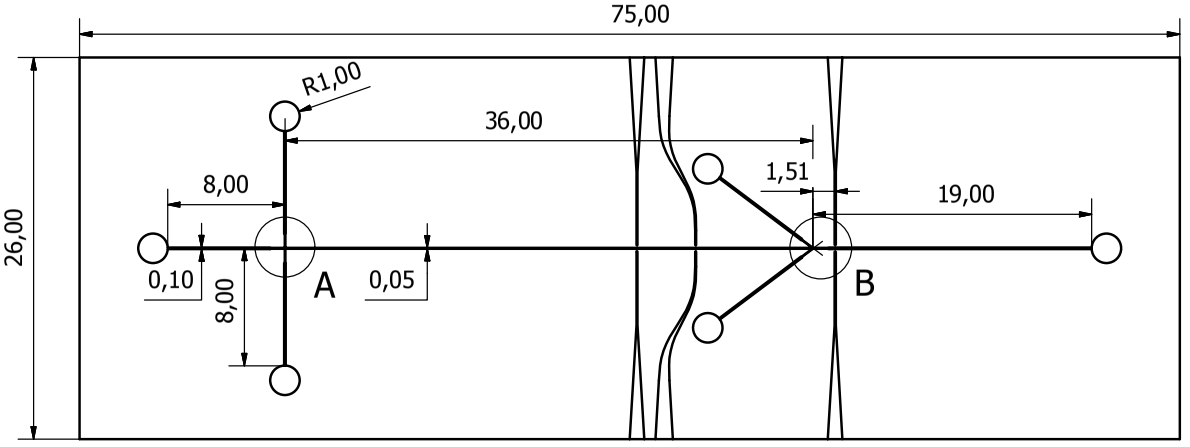

B (20:1)

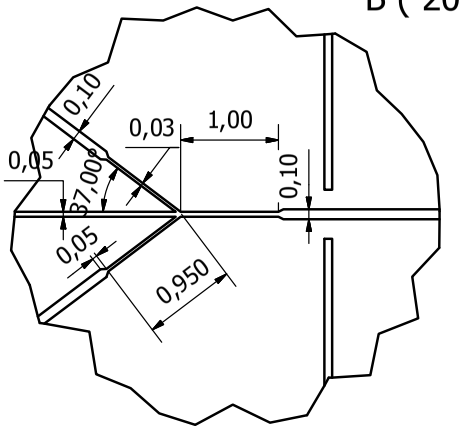

A (10 : 1)

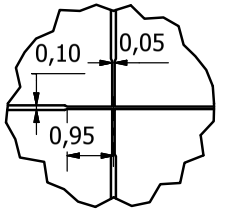

Designed by	Checked by	Approved by	Date	Date	
sise					
		Thiol-ene CE AuNP Chip		Edition	Sheet 1 / 1